1993

Experimental investigation of the laminar necklace vortex system for a rectangular block-flat plate junction

Charles V. Seal
Lehigh University

AUTHOR:

Seal, Charles V., III

TITLE:

Experimental Investigation of the Laminar Necklace Vortex System for a Rectangular Block-Flat Plate Junction

DATE: October 10, 1993

Experimental Investigation of the Laminar Necklace Vortex System for a Rectangular Block-Flat Plate Junction

by

Charles V. Seal III

A Thesis

Presented to the Graduate and Research Committee

of Lehigh University

in Candidacy for the Degree of

Master of Science

in

Mechanical Engineering

Lehigh University

October 1993

CERTIFICATE OF APPROVAL

This thesis is accepted and approved in partial fulfillment of the requirements for the degree of Master of Science.

Sept. 27, 1993
Date

Thesis Advisor
Dr. Charles R. Smith

Department Chairperson
Dr. Robert P. Wei

DEDICATION

To My Parents
For Their Love and Guidance

ACKNOWLEDGMENTS

I wish to thank all those who helped make this work possible. The assistance and suggestions of my lab-mates, Mr. John Fitzgerald, Mr. Jin Kim, and Mr. Levent Takmaz are greatly appreciated. The assistance provided by Mr. Richard Towne, Mr. Robert Minnich, and Mr. James Bunderla, of the Mechanical Engineering Machine Shop is also greatly appreciated.

I thank my advisor Professor Charles R. Smith for his patience, guidance, and recommendations. I look forward to continuing my studies under his supervision.

I would also like to thank Professor D. Rockwell and Mr. Özgür Akin for the loan of their equipment and help in performing the PIV experiments of this study. In addition Professor J. D. A. Walker and Dr. Amar Degani provided insightful comments on the present work and their help is greatly appreciated. Also, valuable comments were given by Dr. M. Visbal at Wright-Patterson AFB.

I need to thank all those who helped keep me sane these past few years. First and foremost, I thank Evelitsa for her patience and support. I thank all my friends here at Lehigh who helped pass the years and many beers, Jin, Eric, Ellyse, May-Win, Ned, Dave, Bill, Steve, Joe, John, Kim, Martin, Ed, Aki, Kenny, Chen, Reneé, Julie, James, and the entire Boilermakers team (I'm staying here until we win one!). I also thank my "old" friends John, Tim, and Al, and the Clarkson boys, Oy!, Beaker, Jay, and Jimbob.

I also wish to thank the Air Force Office of Scientific Research for its support of this research under contract No. AFOSR-91-0218. The continuing support of the AFOSR is gratefully acknowledged.

TABLE of CONTENTS

	Page
TITLE	i
CERTIFICATE OF APPROVAL	ii
DEDICATION	iii
ACKNOWLEDGMENTS	iv
TABLE OF CONTENTS	v
LIST OF FIGURES	viii
NOMENCLATURE	xii
ABSTRACT	1
1.0 INTRODUCTION	3
1.1 GENERAL	3
1.2 RELATED WORKS	4
1.2.1 General Necklace Vortex System Behavior	4
1.2.2 Vortex-Induced Flow	7
1.2.3 Coherent Structures in Turbulent Boundary Layers	8
1.3 OBJECTIVES	9
2.0 EXPERIMENTAL APPARATUS and METHOD	15
2.1 WATER CHANNEL	15
2.2 TEST APPARATUS	15
2.3 TRAVERSING PLATFORM	16
2.4 HYDROGEN BUBBLE VISUALIZATION	17
2.5 INHERENT PARTICLE VISUALIZATION	18

TABLE of CONTENTS (cont.)

	Page
2.6 VIDEO SYSTEM	18
2.7 VISUALIZATION and EXPERIMENTAL TECHNIQUES	19
2.8 PARTICLE IMAGE VELOCIMETRY	20
3.0 EXPERIMENTAL RESULTS and DISCUSSION (FLOW REGIME BEHAVIOR)	31
3.1 INTRODUCTION	31
3.2 OBSERVED FLOW REGIMES	31
3.2.1 General	31
3.2.2 Regime 1 - Steady, Single Necklace Vortex	32
3.2.3 Regime 2 - Steady, Two Vortex System	33
3.2.4 Regime 3 - Oscillating	34
3.2.5 Regime 4 - Amalgamating	35
3.2.6 Regime 5 - Breakaway	35
3.2.7 Transitional Regime	36
3.3 PHYSICAL INTERPRETATION and FLOW REGIME MODELS	40
3.3.1 General	40
3.3.2 Steady Behavior	42
3.3.3 Unsteady Behavior	43
3.4 PARAMETRIC FLOW REGIME CHARACTERIZATION	45
3.5 PRESSURE GRADIENT CHARACTERISTICS	46
3.6 FREQUENCY BEHAVIOR of UNSTEADY REGIMES	48
4.0 VELOCITY/VORTICITY FIELD BEHAVIOR of BREAKAWAY REGIME)	72
4.1 INTRODUCTION	72

TABLE of CONTENTS (cont.)

	Page
4.2 GENERAL CHARACTERISTICS	72
4.3 VELOCITY and VORTICITY FIELD	74
4.4 VORTICITY FLUX	77
4.5 CIRCULATION and TRAJECTORY	77
4.6 VELOCITY PROFILES	81
5.0 CONCLUSIONS	90
REFERENCES	92
APPENDIX A - UNCERTAINTY ANALYSIS	96
APPENDIX B - NO-SLIP WALL CONDITION IMPLEMENTED WITH PIV RESULTS	98
APPENDIX C - FREQUENCY DATA	100
VITA	103

LIST of FIGURES

		Page
Figure 1.1	Schematic of the necklace vortex system formed at the junction of a rectangular block and flat plate.	11
Figure 1.2	Hydrogen bubble visualization of the necklace vortex system formed at the junction of a rectangular bluff body and flat plate.	12
Figure 1.3	Schematic of a vortex-surface interaction.	13
Figure 1.4	Schematic of a streak generating hairpin vortex model.	14
Figure 2.1	Schematic of water channel. Plan view.	23
Figure 2.2	Side-view schematic of water channel.	24
Figure 2.3	Schematic of light-sheet illumination and end-view mirror.	25
Figure 2.4	Plan-view schematic of video system and camera locations.	26
Figure 2.5	Schematic of hydrogen bubble equipment.	27
Figure 2.6	Schematic of rectangular block mounting and field of view. U_∞=50.4 mm/s, Re_{δ^*}=298, $Re_L=3x10^4$.	28
Figure 2.7	Side-view schematic of PIV experimental apparatus, including laser system.	29
Figure 2.8.	Plan-view schematic of PIV experimental apparatus, showing orientation of the bias mirror.	30
Figure 3.1	Symmetry plane streamline schematic of regime 1 (steady, single-vortex).	51
Figure 3.2	Hydrogen bubble visualization and streamline schematic of regime 2 (steady, two-vortex).	52
Figure 3.3	Hydrogen bubble visualization and corresponding schematic time sequence of the oscillating regime (regime 3), where $t^*=t/T$ (t=time and T is the period of one cycle). The height of the induced counter-rotating structures is a relative measure of their strength.	53

LIST of FIGURES (cont.)

		Page
Figure 3.4	Hydrogen bubble visualization and corresponding schematic time sequence of the amalgamating regime (regime 4), where $t^*=t/T$ (t-time and T is the period of one cycle). The height of the induced counter-rotating structures is a relative measure of their strength.	54
Figure 3.5	Hydrogen bubble visualization and corresponding schematic time sequence of the breakaway regime (regime 5), where $t^*=t/T$ (t=time and T is the period of one cycle. The height of the induced counter-rotating structures is a measure of their relative strength.	55
Figure 3.6	Oblique view hydrogen bubble visualization of the transitional regime showing the formation of hairpin vortices.	56
Figure 3.7	End-view hydrogen bubble visualization of a hairpin vortex in the transitional regime.	57
Figure 3.8	End-view hydrogen bubble visualization of the interaction of a hairpin vortex in the transitional regime with the surface. The hydrogen bubble wire is located in the plate surface, just upstream of the transverse light sheet.	58
Figure 3.9	Schematic of transitional regime.	59
Figure 3.10	Control surface used to aid physical interpretation of the results.	60
Figure 3.11	Mutual induction effects by image vorticity for a single necklace vortex.	61
Figure 3.12	Flow regime plotted as a function of δ^*/W and Re_{δ^*} for both the 5.1 cm and 15.24 cm wide block.	62
Figure 3.13	Flow regime plotted as a function of δ^*/W and Re_{δ^*} for both the 5.1 cm and 15.24 cm wide block.	63
Figure 3.14	Lines of flow regime transition, based on Figures 3.12 & 3.13.	64
Figure 3.15	Comparison of rectangular block flow regime map to the flow regime map of a cylinder.	65

LIST of FIGURES (cont.)

		Page
Figure 3.16	Dimensionless pressure $(p-p_0)^*=2(p-p_0)/\rho U^2$ and pressure gradient $dp^*/dx^*=2W(dp/dx)/\rho U^2$ vs. x/W for an inviscid approach flow to a rectangular body, were p_0 is the stagnation pressure.	66
Figure 3.17	Normalized frequency data for the 5.1 cm x 5.1 cm block.	67
Figure 3.18	Normalized frequency data obtained for the 15.24 cm x 5.1 cm block.	68
Figure 3.19	Normalized frequency for the 5.1 cm and 15.24 cm wide blocks.	69
Figure 3.20	Normalized frequency data obtained for the 15.24 cm and 5.1 cm wide blocks.	70
Figure 3.21	Normalized frequency data obtained for the 15.24 cm and 5.1 cm wide blocks and linear curve fit.	71
Figure 4.1	Schematic of unsteady necklace vortex system behavior viewed on the symmetry plane.	83
Figure 4.2	Sample velocity field (corresponding to figure 4.3a v) obtained after interrogation and post processing. Vector spacing is approximately 1.02 vectors/mm.	84
Figure 4.3	(a) Vorticity contours. Dashed lines indicate negative vorticity, solid lines indicate positive vorticity. Time between frames is 1.0s. (b) Vorticity flux.	85
Figure 4.4	Vortex trajectory (open symbols) and non dimensional strength (Γ_v/Γ_e, closed symbols), where Γ_e is the time integral of vorticity flux passing across the left edge of the field of view over one cycle. Plotted data corresponds to Figure 4.3 iv to 4.3 xi. Circles represent the impinging primary vortex, triangles represent the corner vortex, and squares are the new corner vortex after amalgamation.	86
Figure 4.5 (a)	Selected u-velocity profiles for Figure 4.3a v.	87
Figure 4.5 (b)	Selected u-velocity profiles for Figure 4.3a ix.	88

LIST of FIGURES (cont.)

		Page
Figure 4.6	Centerline velocity profiles of a necklace vortex advecting downstream. Profiles correspond to the centerline of the primary vortex shown in Figures 4.3a iv to 4.3a vii. Each profile is taken at one second intervals.	89
Figure B.1	Comparison of vorticity contours with and without the no-slip condition imposed on the plate surface.	99
Figure C.1	Frequency (1/s) data obtained for the 5.1 cm x 5.1 cm block.	101
Figure C.2	Frequency (1/s) data obtained for the 15.24 cm x 5.1 cm block.	102

NOMENCLATURE

A	Area
d_I	Width of the interrogation window
FFT	Fast fourier transform
H	Angular momentum
I	Mass moment of inertia
L	Distance from the leading edge to the block
M	Magnification factor
R	Radius
Re_{δ^*}	Reynolds number based on the displacement thickness
Re_L	Reynolds number based on the distance from the leading edge to the block
s	Unit vector defining the integration path
T	Period
t	Time
t_e	Equivalent time
t^*	Non-dimensional time
$U_{\infty,local}$	Local free stream velocity
u	x-direction velocity
u_{adv}	Advection velocity
v	y-direction velocity
x,y,z	Cartesian coordinates in streamwise, normal, and spanwise directions
Δl	Grid width
δ	Boundary layer thickness
δ^*	Displacement thickness
Φ_ω	Vorticity flux
Γ_e	Equivalent circulation
Γ_v	Circulation of necklace vortex
ρ	Density
Ω	Angular velocity
ω	Vorticity

ABSTRACT

The unsteady laminar necklace vortex system formed at the junction of a rectangular bluff body and a flat plate was studied experimentally using hydrogen bubble flow visualization and particle image velocimetry (PIV). The vortex system was found to exhibit flow regime behavior similar to that described by other investigators for cylinder-flat plate junctions, characterized by the five distinct regimes of flow behavior.

Of the five flow regimes established, two were steady at lower Reynolds numbers and three were unsteady and periodic at higher Reynolds numbers. The flow regime present, as well as the frequency of events in the unsteady regimes, depends on free-stream velocity, fluid viscosity, block width, and distance of the block from the leading edge of the plate. Using the principles of vortex interaction, interpretations are made of the physics of the processes within the respective regimes.

The frequency of events in the three unsteady regimes is determined to be a direct function of flow velocity, and an inverse function of block width and distance from the leading edge of the test plate.

Above a critical Reynolds number the necklace vortex system was found to break down into a transitional flow regime, wherein hairpin-like distortions in the necklace vortices develop, which amplify and feed back upstream, causing the three-dimensional breakdown of the entire system. This transitional regime is characterized by the formation of hairpin vortices and the development of an unsteady two-vortex system near the corner of the block-plate junction.

Detailed spatial-temporal measurements of the velocity/vorticity field for a case within a periodic, unsteady flow regime are made on the symmetry plane using a

scanning laser Particle Image Velocimetry (PIV) technique. Detailed analysis of the PIV measurements indicates that the dominant mechanism for vorticity balance in the necklace vortex system is the cross-cancellation of the vorticity of the necklace vortices with vorticity of opposite sign generated by interaction of the vortices with the approach surface to the body.

1.0 INTRODUCTION

1.1 GENERAL

When a boundary layer flow (either laminar or turbulent) encounters a bluff body extending from a surface, a complex, three-dimensional flow field develops in the junction region. These flows occur in many practical applications such as wing-body junctions, turbine blade-hub junctions, and cooling flow past computer chips on a circuit board. Flows of this type can often have profound effects on the flow-dependent properties in the junction region, such as the local heat transfer rates and local skin friction.

Due to the adverse pressure gradient generated by the presence of the bluff body, the approaching boundary layer fluid will undergo local flow reversal, creating a region of separation upstream of the body. The impinging boundary layer destabilizes, forming spanwise vortex structures fed by advected vorticity generated upstream at the leading edge of the plate. The body also imposes a cross-stream pressure gradient, causing the boundary layer to divert symmetrically around the body, thus introducing a high degree of three dimensionality. The end result is the organization of the impinging vorticity into a necklace vortex system (Figure 1.1, and 1.2) in the junction region of the bluff body, which appears as one or more horseshoe-shaped vortices oriented such that the legs of the vortices extend downstream on either side of the body, with the apex of the deformed vortex located on the symmetry plane of the bluff-body.

These types of necklace vortex flows develop in many real systems and can have significant consequences. For example, at the junction of a conning tower and submarine

hull, the formation of a necklace vortex system will cause an increase in both local skin friction, drag, and noise. In addition, the legs of the necklace vortices can extend downstream and interfere with propeller or control surface operation (Lugt, 1983). In the case of a turbine blade-hub junction, the recirculation zones can greatly affect local heat transfer rates, increasing thermal gradients in the blade. In addition, increased skin friction due to necklace vortex development adjacent to a bridge or pier support can cause severe erosion at the base of the support.

1.2 RELATED WORKS

1.2.1 GENERAL NECKLACE VORTEX SYSTEM BEHAVIOR

Necklace vortex systems exhibit a range of steady and unsteady behavior depending on the Reynolds number, boundary layer thickness, and a characteristic dimension of the body (width, diameter, etc.). Previous studies of unsteady necklace vortex systems include investigations of: the vortex system formed by the interaction of a laminar boundary layer in the junction of a 60° included-angle wedge in air (Schwind, 1962); the behavior within a cylinder-flat plate junction in air with a laminar approach flow (Baker, 1979); and the flow behavior at a cylinder-flat plate junction with both air and water flows (Thomas, 1987). Both Schwind and Baker examined the steady (lower Re) as well as periodic unsteady (higher Re) necklace vortex regimes, while Thomas concentrated on the unsteady regimes. Baker (1979) determined that the unsteadiness exhibited by the vortex system is not related to the vortex shedding of the cylinder by altering the shedding patterns of the cylinder with a splitter plate and detecting no changes in the necklace vortex behavior.

For a cylinder-flat plate junction with laminar approach flow in water, Greco (1990) provides the most comprehensive classification and description of the range of necklace vortex behavior. Based on the studies of Greco, the behavior of a junction necklace vortex system can be generally classified into five regimes;

1. Steady	One, two, or three steady necklace vortices form with the number of vortices increasing as Re is increased;
2. Oscillating	Vortices oscillate periodically with increasing frequency as Re increases;
3. Amalgamating	The primary vortex (the vortex closest to the body) breaks away from the formation region and advects towards the body, but is then drawn back to and amalgamates with the secondary vortex (the vortex following the primary vortex), forming a new primary vortex. Amalgamation is a periodic event for which frequency increases as Re increases;
4. Breakaway	The primary vortex periodically breaks away from the formation region and advects downstream towards the body. The frequency of break away increases with increasing Re;
5. Transitional	The entire system destabilizes into three-dimensional, turbulent-like behavior.

Additional studies of the necklace vortex system include Gregory and Walker (1951) who studied a cylinder entirely immersed in the boundary layer, noting that variations in cylinder height affects the strength and character of the vortex system when the ratio of cylinder height to boundary layer thickness is approximately 1.0 or less. Also noted was that at very low velocities no vortices were found to form. A similar, but independent study by Sedney and Kitchens (1975) established similar behavior.

Little is known of the junction region of a rectangular bluff body on a flat plate. Norman (1972) investigated the laminar and turbulent vortex system formed in the

junction region of fence-like obstructions using air, and observed basically similar behavior to that described by Greco. However, Norman did not measure local velocity behavior or examine the vorticity behavior involved in these types of flows, nor did he examine wide bodies.

The present study examines the regimes and frequency behavior for the necklace vortex system formed at the junction of a rectangular bluff body with a flat plate, for which the necklace vortex system was shown to progress through essentially the same types of regimes as those described above for cylinder-flat plate junctions. The present study expands on previous work, which consists mainly of qualitative visualization and limited hot film measurements, by making instantaneous measurements of the velocity field of the necklace vortex system and employing these measurements to examine the behavior of the vorticity in the system.

As mentioned above, the necklace vortex system is stimulated by the adverse pressure gradient produced by the presence of the body, which causes flow separation and reversal in the boundary layer near the body, and reorganization of advected boundary layer vorticity into discrete vortices. Since vorticity is continuously generated at the leading edge of the plate, this raises the question of what happens to this vorticity as it approaches the junction region near the block. If the vorticity were to continuously accumulate in front of the body, the vortex system would continuously grow, which is not the case, since vortex systems of apparently discrete amounts of vorticity exist in one of several modes of either steady or periodic behavior. Therefore, a balance of vorticity must somehow be maintained by the system.

1.2.2 VORTEX-INDUCED FLOW

An important consideration in the study of the necklace vortex system is the interaction of the vortices with the plate surface, because the necklace vortices induce strong vortex-surface interactions which are "instrumental in modifying the local dynamics" of the system (Greco, 1990). Several previous experimental and numerical studies of vortex-surface and vortex-boundary layer interactions are helpful in understanding the observations of the present study.

The previous studies of Harvey and Perry (1971) and Walker (1978), which examined the flow induced near a surface by a vortex, showed that recirculating eddies form in the boundary layer near a planar surface due to the local pressure gradient induced by the vortex in close proximity to the surface. Harvey and Perry experimentally examined a trailing tip vortex while Walker numerically studied a two-dimensional vortex. The general findings of these studies is illustrated in Figure 1.3. Both studies observed that as the strength of the secondary vortices increases, an upflow of the surface fluid develops between the two vortices, which causes the local boundary layer to thicken. Eventually the upflow of surface fluid develops into a strong eruption, lifting fluid away from the surface, which interacts with the outer flow. Also, the secondary vortices are ejected away from the surface, into the outer flow during the final stages of the process. Walker *et al.* (1987), using numerical simulation and experimental observations, observed similar behavior for the flow induced by a vortex ring impacting a plane wall.

Peridier and Walker (1991), using asymptotic theories and Lagrangian numerical techniques (a refinement on the techniques used in the Walker, 1987 study), simulated the vortex-induced boundary layer separation by a two-dimensional vortex above a plane wall. The results showed the development of the secondary vortex described above,

however the refined numerical techniques, enabled the solution to be extended past the previous study of Walker (1978) to the point of illustrating boundary layer separation.

1.2.3 COHERENT STRUCTURES IN TURBULENT BOUNDARY LAYERS

This study also examines the behavior of the transitional regime of the necklace vortex system, which demonstrates comparative similarity to a number of the coherent flow structures observed in turbulence. Therefore, a *brief* review of the research in this area is presented.

Rundstadler *et al.* (1963) first documented the presence of low-speed streaks in the near-wall region of turbulent boundary layers. They observed that these low-speed streaks eventually lift away from the wall, destabilize, and burst due to an interaction with the outer flow. Kim *et al.* (1971) found that the bursting of the streaks is critical to the generation of new turbulence. The behavior of the low-speed streaks has been shown to be related to streamwise counter-rotating vortices present in the near-wall region. Blackwelder and Ecklemann (1979) found velocity patterns indicative of counter-rotating streamwise vortices in the near-wall region during the aforementioned bursting process. The existence the streamwise vortices and their relationship to the formation of the low-speed streaks was confirmed visually by Smith and Schwartz (1982).

The hairpin vortex has been suggested to be a primary flow structure responsible for coherent behavior of turbulent boundary layers by a number of researchers including; Theodorsen (1952), Willmarth and Tu (1967), Offen and Kline (1975), Perry and Chong (1982), Smith (1984), Smith *et al.* (1991), and many others. The model for hairpin vortices in a turbulent boundary layer consists of modeling the streamwise counter-rotating vortices mentioned above as the trailing legs of hairpin vortices. The low-speed streaks are theorized to be generated by the accumulation of low-momentum fluid

adjacent to the counter-rotating legs. Figure 1.4 illustrates a model for streak generation by a hairpin vortex. The validation of this hypothesis consists of studies by Smith and Acalar (1987) and Haidari and Smith (1993) which showed that the generation of hairpin vortices in a laminar environment creates visualization patterns and velocity statistics consistent with those for fully turbulent boundary layers.

1.3 OBJECTIVES

The overall objective of the present study was to expand on the work of Greco (1990) by characterizing the necklace vortex regimes for a rectangular block-flat plate junction and establishing velocity/vorticity fields of the breakaway regime. This later study examines the breakaway regime, since this regime exhibits a rich environment of periodic vorticity reorganization, and clear vortex-surface interactions.

The specific objectives of the present study are to:

1. Characterize and categorize the different regimes of flow behavior for rectangular block end-wall junction flows;
2. Determine the parametric relationship between the observed regime and the relevant flow parameters (W, U_∞, δ^*, etc.);
3. Establish the frequency characteristics of the unsteady regimes and obtain a functional relationship between the frequency and the relevant flow parameters;
4. Examine the transitional regime of behavior of the necklace vortex system and compare the processes with flat plate transition and turbulence;
5. Establish temporal flow field velocity/vorticity measurements of the periodic breakaway regime using Particle Image Velocimetry (PIV) techniques; and

6. Examine how vorticity is distributed within the necklace vortex system formed in front of a rectangular bluff body and how this vorticity temporally redistributes itself within the vortex system to maintain the balance of vorticity.

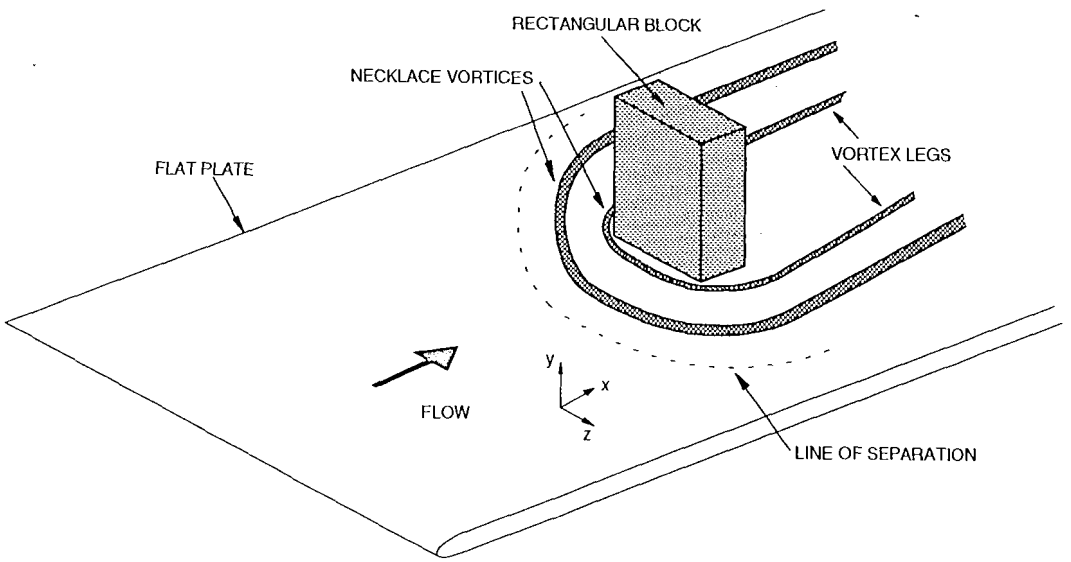

Figure 1.1 Schematic of the necklace vortex system formed at the junction of a rectangular block and flat plate.

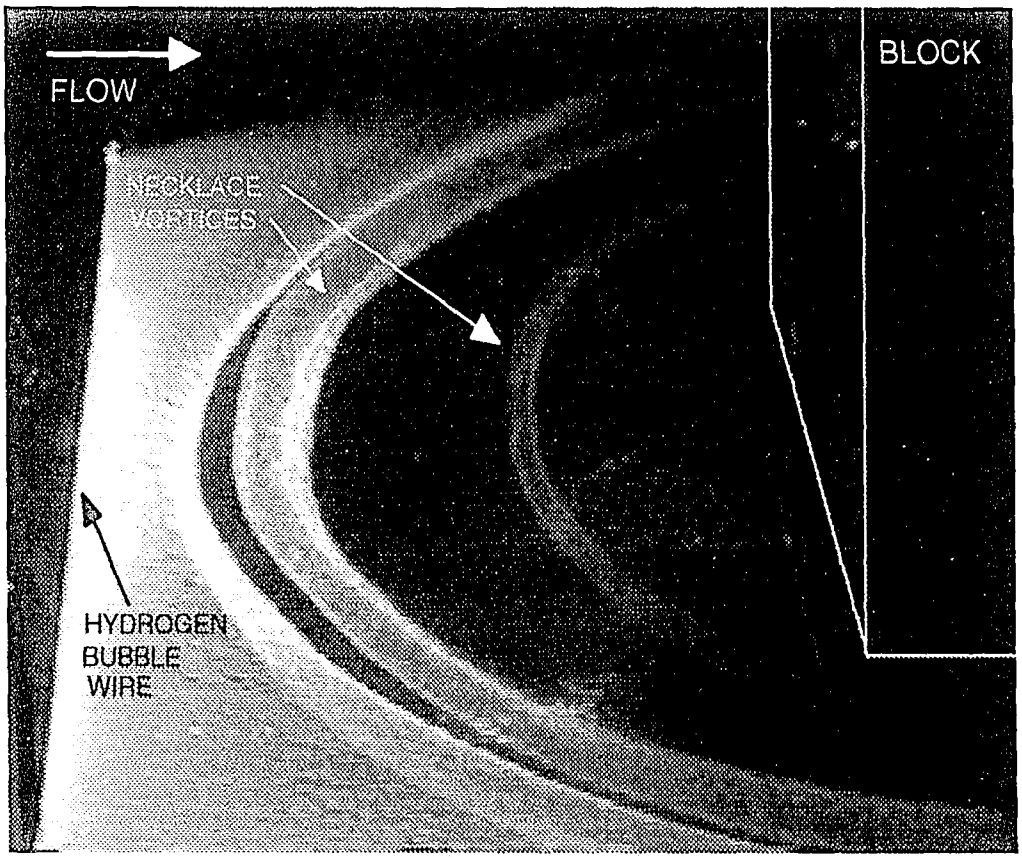

Figure 1.2 Hydrogen bubble visualization of the necklace vortex system formed at the junction of a rectangular bluff body and flat plate.

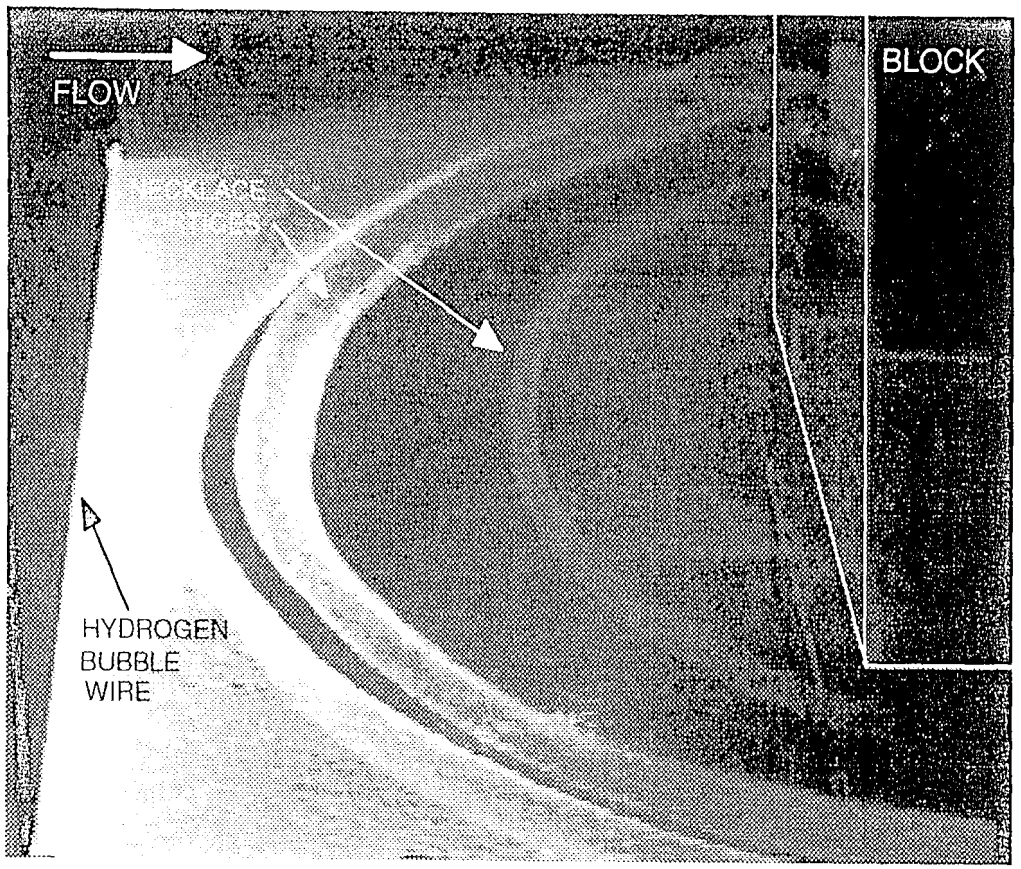

Figure 1.2 Hydrogen bubble visualization of the necklace vortex system formed at the junction of a rectangular bluff body and flat plate

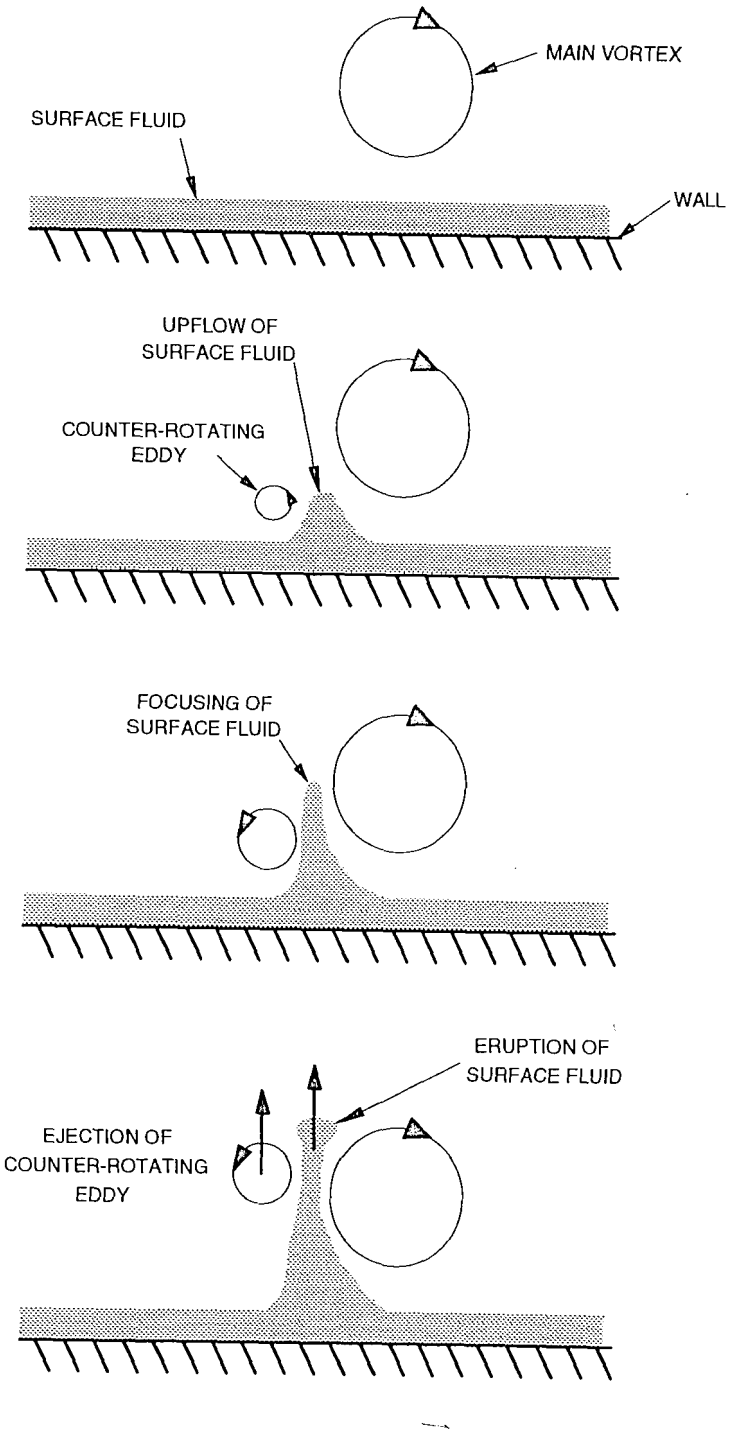

Figure 1.3 Schematic of a vortex-surface interaction.

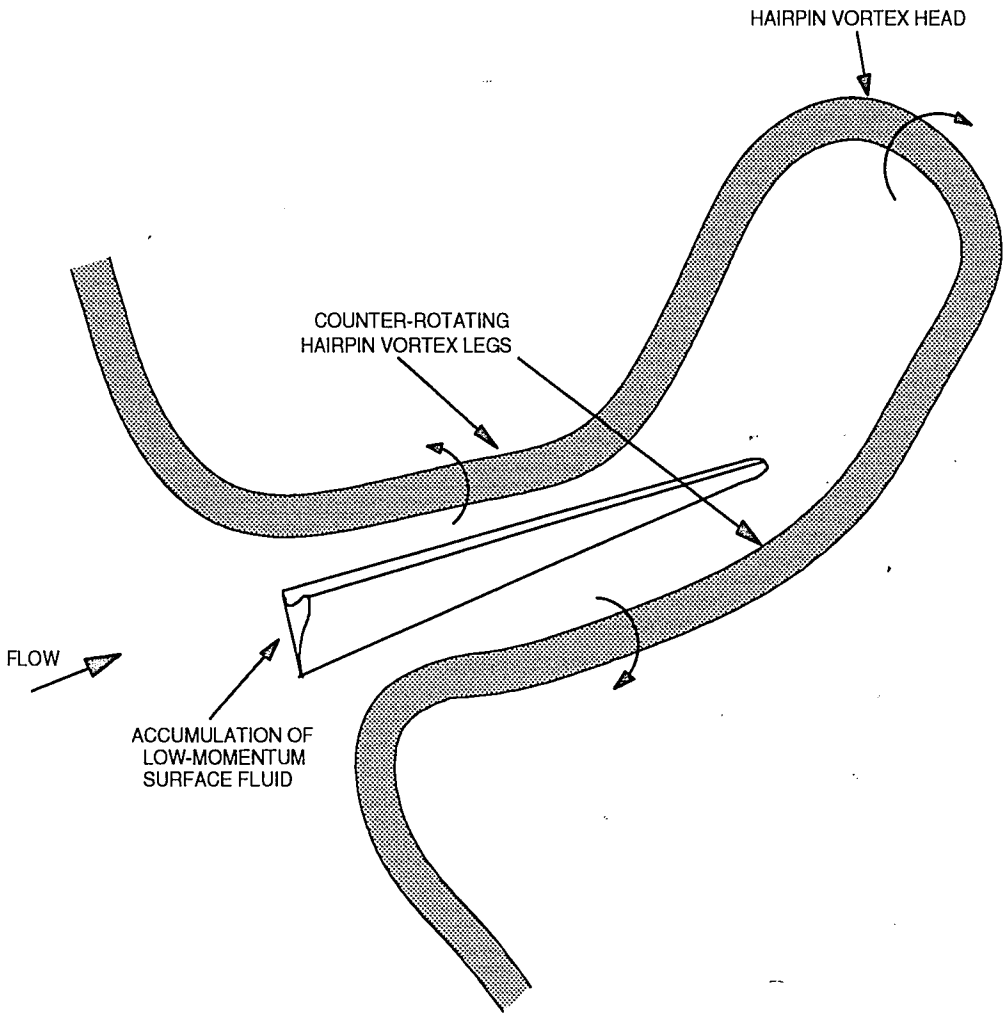

Figure 1.4 Schematic of a streak generating hairpin vortex model.

2.0 EXPERIMENTAL APPARATUS and METHOD

2.1 WATER CHANNEL

Experiments were performed in a Plexiglas free-surface water channel with a test section 0.3 m deep by 0.9 m wide by 5.0 m long (Figures 2.1 and 2.2) located in the Lehigh University Fluid Dynamics Research Laboratory. The water depth was maintained at 28.9 cm for all experiments. The flow was driven by a Westinghouse variable-speed, feedback-controlled, 7.5 horsepower, DC motor connected to a split casing centrifugal pump. The pump feeds water into the inlet tank via a distribution manifold, which then passes through a fiberglass honeycomb flow straightener (7.5 cm wide, 0.8 cm cell) to establish uniform flow, followed by two 20-mesh, stainless steel, turbulence control screens. A 2:1 inlet contraction is used to reduce any remaining flow irregularities prior to the working section. The flow then passes through the working section to an outlet tank, and is recirculated.

At a water depth of 28.9 cm the channel provides a stable flow from 0.01 m/s to 0.4 m/s, with free-stream turbulence intensities near the beginning of the test section less than 0.2 percent at a flow velocity of 0.12 m/s (Greco 1990).

2.2 TEST APPARATUS

A 2.6 m long (1.2 cm thick) Plexiglas flat plate with a 5:1 elliptical leading edge was used to establish a laminar boundary layer for the present studies. The plate is elevated 10.2 cm above the channel floor by four sets of spanwise supports, thus

providing a water depth of 18.7 cm above the plate. The leading edge of the plate was located 0.85 m from the beginning of the working section for all experiments. Previous measurements have shown this plate to yield Blasius behavior to ±3%; therefore the boundary layer thickness (δ) and the displacement thickness (δ^*) can be computed using the standard Blasius equations. This plate can be used to generate boundary layer thicknesses from 0.1 cm to more than 7.0 cm, yielding corresponding Re $_{\delta^*}$ of 20.0 to 1,427. The coordinate system for this study was defined as shown in Figure 2.3.

The two rectangular blocks examined were: 5.1 cm wide x 20.3 cm high x 5.1 cm deep, and 15.2 cm wide x 20.3 cm high x 5.1 cm deep. Using these two blocks Reynolds numbers based on block width ranging from 625 to 42,000 could be examined. The blocks were located on the centerline of the plate to maintain symmetry. The blocks were constructed of Plexiglas with carefully machined end surfaces to eliminate leakage between the block and the plate. The Plexiglas construction also allowed end views of the flow to be done through the block using a downstream viewing mirror (Figure 2.3 and 2.4).

2.3 TRAVERSING PLATFORM

A traversing platform mounted above the working section of the water channel (Figures 2.1 and 2.2) was used in the present study for probe support and location. The platform rides on two 4.1 m long cylindrical steel rails mounted on top of each side of the channel frame. The platform is driven by a 1.0-horsepower Reliance Electric motor capable of generating platform speeds of 0.01 m/s to 0.24 m/s in either direction. In the present study, the platform was only used for probe support. Hydrogen bubble probes were mounted on a mechanism capable of positioning the probe in three directions,

which in turn was mounted on the platform (Figures 2.1 and 2.2), allowing the probe to be located anywhere in the flow field.

2.4 HYDROGEN BUBBLE VISUALIZATION

Limited flow visualization was performed using a moveable hydrogen bubble visualization probe consisting of a 25 μm diameter platinum wire soldered taut between two insulated brass rods forming a Y-shaped support. The wire is used as the cathode in a process of electrolysis, with a variable voltage/frequency power supply providing a pulsed current density to the wire; the anode was a 6.0 mm diameter carbon rod located away from the region of interest (Figure 2.5). The result is the generation of fine hydrogen bubbles which enable the visualization of the flow structure. Sodium sulfate (Na_2SO_4) is added in a concentration of 0.15 g/L to increase the conductivity of the water, thus improving bubble quality and reducing the voltage required to achieve the electrolytic process. The probe was placed in a cross-stream orientation upstream of the body in all instances (Figure 2.3). The distance from the block and the plate surface varied according to how the flow was to be marked.

Lighting consisted of either general illumination through the bottom of the channel using a 1050W photographic lamp, or light sheet illumination created by masking portions of the channel floor or using a 10-watt scanned argon-ion laser (Rockwell *et al.*, 1993). The light sheets were located either on the symmetry plane or upstream of the body in a cross-stream orientation (Figure 2.3).

2.5 INHERENT PARTICLE VISUALIZATION (IPV)

A novel visualization approach was used extensively in the present study in addition to hydrogen bubble visualization. Ordinary tap water (used in these experiments) contains large numbers of small inherent particulates. While these are not of the quality of those used for PIV (see below), they are visible when illuminated by a scanned laser sheet, which provides sufficient visualization of the flow behavior for characterization of the flow structure without the intrusion of a probe.

This IPV technique was used exclusively for flow characterization, because in certain instances a hydrogen bubble probe was found to affect the flow behavior. Also, hydrogen bubble visualization has limited effectiveness at lower flow speeds, where the buoyancy of the bubbles restricts their usefulness as a visualization tool; with IPV effective visualization at lower flow speeds can be easily attained.

2.6 VIDEO SYSTEM

The flow visualization experiments were recorded in real time using a SONY SSC-S20 CCD color video camera connected to a PANASONIC AG-7300 SVHS video cassette recorder capable of recording at 60 interlaced frames per second (Figure 2.4). The camera was fitted with an 18-108 mm zoom lens enabling detailed observation of small scale structures on the order of millimeters in the flow. At the highest zoom setting a field of view 2.9 cm x 2.2 cm could be obtained. A SONY PVM-1943MD color video monitor was used to view the experiments as they were performed and recorded, and later for analysis of the recorded sequences.

The recorder is capable of playing the video either forwards or backwards, in slow motion or freezing a selected frame. A single-frame advance mode was also used to

allow detailed analysis of the experiments. Single images from a video sequence could be either photographed from the monitor screen using a 35 mm camera or digitized into a TIFF file format via a DATA TRANSLATION video frame grabber board.

2.7 VISUALIZATION and EXPERIMENTAL TECHNIQUES

Visualization was used to both characterize the flow behavior and determine the frequency behavior of the unsteady regimes over a wide range of flow parameters. Systematic visualization was done for both blocks at four different locations from the leading edge of the plate (0.1 m, 0.3 m, 0.6 m, and 1.0 m). For each block location the free-stream flow velocity (U_∞) was varied systematically from a minimum of 1.23 cm/s to a maximum of 26.6 cm/s. This allowed the examination of parameter ranges of $60 \le Re_{\delta^*} \le 825$ and $1200 \le Re_L \le 5.3 \times 10^5$ (where L is the distance from the leading edge to the block), and $620 \le Re_W \le 4 \times 10^4$ (where W is the width of the block).

At each fixed velocity, a video sequence of the flow was recorded for later characterization of the flow behavior. The video was analyzed to establish the flow behavior and the frequency of events in the unsteady regimes. The frequency of periodic events was calculated from the recorded sequences by measuring, with a stopwatch the time for passage of a given number of repetitive flow structures using a fixed reference point on the monitor. An uncertainty analysis (Klein and McClintock, 1953) of this technique shows a worst case uncertainty of approximately $\pm 1.0\%$.

2.8 PARTICLE IMAGE VELOCIMETRY (PIV)

High image-density particle image velocimetry (Adrian, 1991; Rockwell *et al.*, 1993), was used to establish the details of the velocity field for one particular case in the unsteady breakaway regime. The 15.2 cm wide block was mounted 0.6 m from the leading edge of the plate (Figure 2.6) and oriented such that the width was perpendicular to the flow direction.. The free stream velocity U_∞ was set at 50.4 mm/s, which gave corresponding $Re_L=3x10^4$ and $Re_{\delta^*}=298$, based on (1) the distance L from the leading edge to the block, and (2) the displacement thickness δ^* calculated for an *equivalent* unobstructed Blasius boundary layer at 0.6 m.

The scanned laser was used to illuminate spherical, metallic-coated particles (nominal diameter of 12 μm and density of 2.6 g/cm^3) on the symmetry plane. Approximately 20 cm^3 of particles were mixed in the 2400 gallon water channel, which assured approximately 15 particle images within each interrogation window (1.7 mm x 1.7 mm in the plane of the laser sheet; see below). The scanned laser sheet was generated using a 72 facet rotating mirror in conjunction with a 10 watt Argon-ion laser. An optical assembly employing a convex lens, concave lens, and a singlet lens (Corcoran, 1992) was used to focus the beam to a diameter of approximately 1.0 mm at the region of interest (Figures 2.6 and 2.7). A combination of a 150 Hz laser scanning rate and a 1/30 second camera exposure time was employed, which produced image photographs with 5 exposures of each particle within the viewing field. Photographs were taken at a rate of 1 image/sec for 10.0 seconds, capturing a little more than one breakaway cycle. A NIKON F3 35 mm camera (using Kodak TMAX 400 film) was used to record the particle images (Figure 2.8).

A rotating bias mirror was located immediately in front of the camera lens, at an angle of 45° to the centerline of the lens (Figure 2.8). Its purpose was to impart a

uniform bias velocity to all particles while they were being photographed in order to overcome the directional ambiguity associated with regions of reverse (negative) flow, and decrease the dynamic range of the image patterns, thereby enhancing the success rate of the evaluation process leading to the velocity field. The magnitude of the imposed bias was sufficiently large to overcome negative velocities associated with regions of reverse flow, but small enough such that the principal features of the actual velocity field were not obscured. The principal guidelines for determining the minimum bias velocity (Towfighi, 1992) is that a line passing through successive, multiply-exposed particle images should not turn an angle greater than 90 °. In order to recover the actual velocity field, the uniform bias velocity was subtracted from the field of vectors obtained after evaluation of the entire image.

To evaluate the entire pattern of particle images recorded on 35-mm film, a given pattern is digitized into a TIFF file format, using a Nikon LS-3510AF 35-mm film scanner in conjunction with a 486 PC housing two Eighteen-Eight array processors. The resolution of the digitized pattern of images was 125 pixels/mm of film. The velocity at a given location was determined from the digitized image (4125 pixels x 2625 pixels) using a single-frame autocorrelation technique involving application of two successive FFTs over an interrogation window of 80 x 80 pixels. This window was sequentially moved across the image in order to determine the velocity at successive locations. In order to approximate the Nyquist sampling criterion, adjacent windows were overlapped by 40%. This evaluation process yielded approximately 4,950 velocity vectors. Since the magnification M of the camera lens was 1:2.6, the effective width d_I of the interrogation window in the plane of the laser sheet was $d_I/M=1.7$ mm; correspondingly, the effective grid width was $\Delta l/M=1.02$ mm in the laser sheet. The interrogation process was not successful at all locations. Due to a variety of factors, including locally-

inadequate quality of the particle images or insufficient particle concentration, the evaluation process can lead to an incorrect vector or no vector at all. In cases where the vector differed drastically from its neighbors, it was manually deleted. Each blank interrogation area was then replaced by a vector determined by bilinear interpolation. Typically, not more than two to three percent of the vectors in the entire velocity field had to be determined using this interpolation process.

Prior to further processing, the entire field of velocity vectors was smoothed by convolving the field of vectors with a Gaussian kernel having a coefficient p=1.3, which minimizes distortion of the original field of vectors (Landreth and Adrian, 1989). No further filtering or smoothing was done in constructing the contours of constant vorticity; these contours were determined by a cubic spline fit through the discrete values of vorticity using a tension factor of 0.1. For certain plots, the levels between vorticity contours were interpolated to emphasize the structural features of the flow. The typical minimum distance between contours was approximately one third of the grid width Δl/M; in a few high gradient regions it decreased to as low as one sixth Δl/M. The top and left boundaries of the flow field were free; the bottom and right boundaries were solid surfaces. Special care was taken to ensure that the no slip condition was maintained at the bottom surface during post processing.

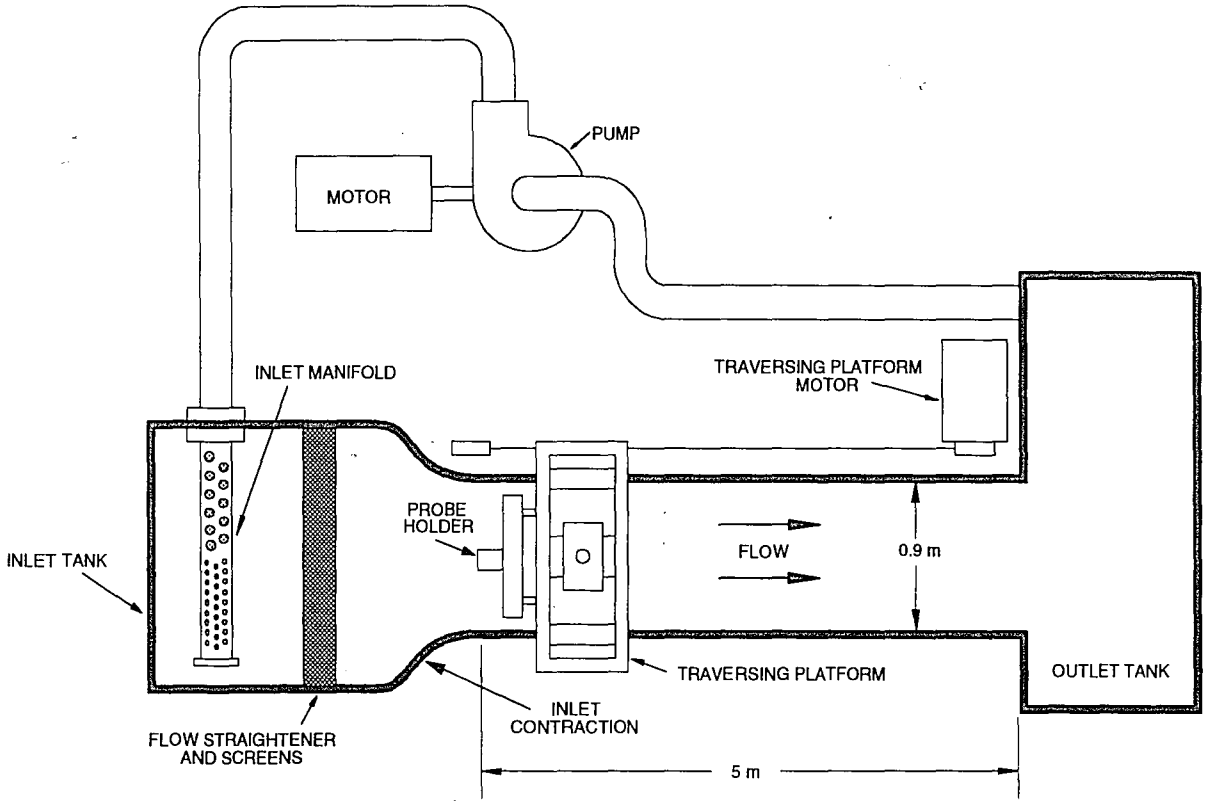

Figure 2.1 Schematic of water channel. Plan view.

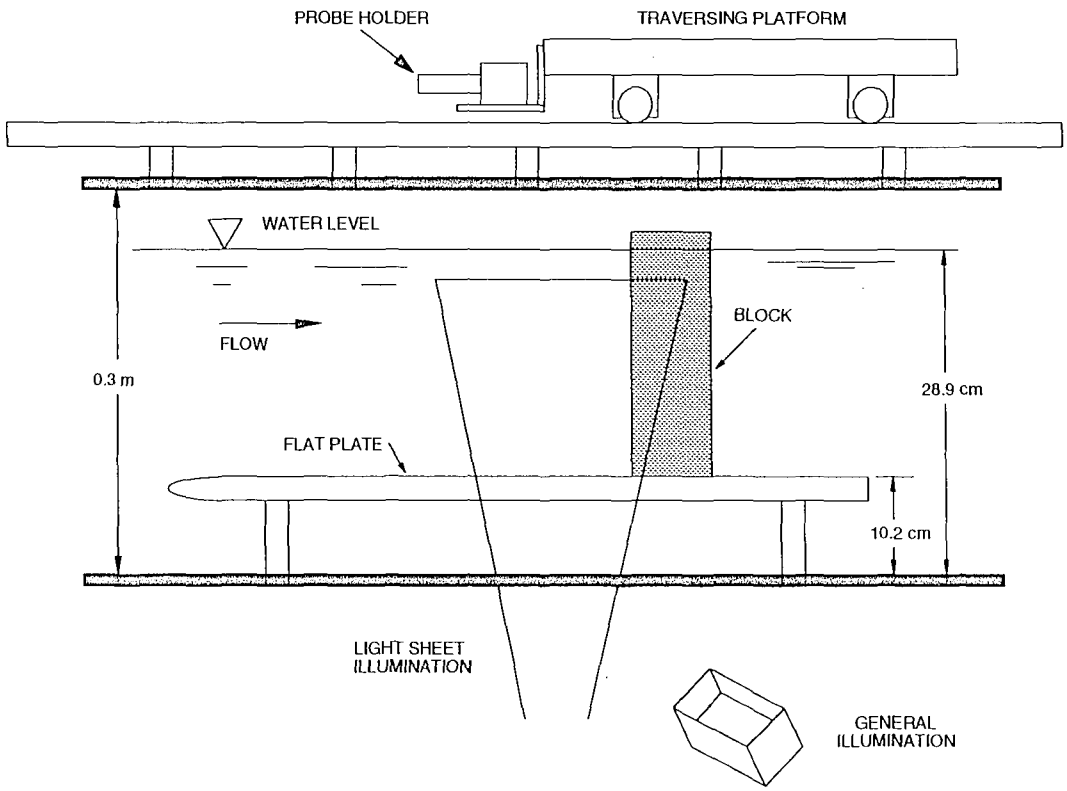

Figure 2.2 Side-view schematic of water channel.

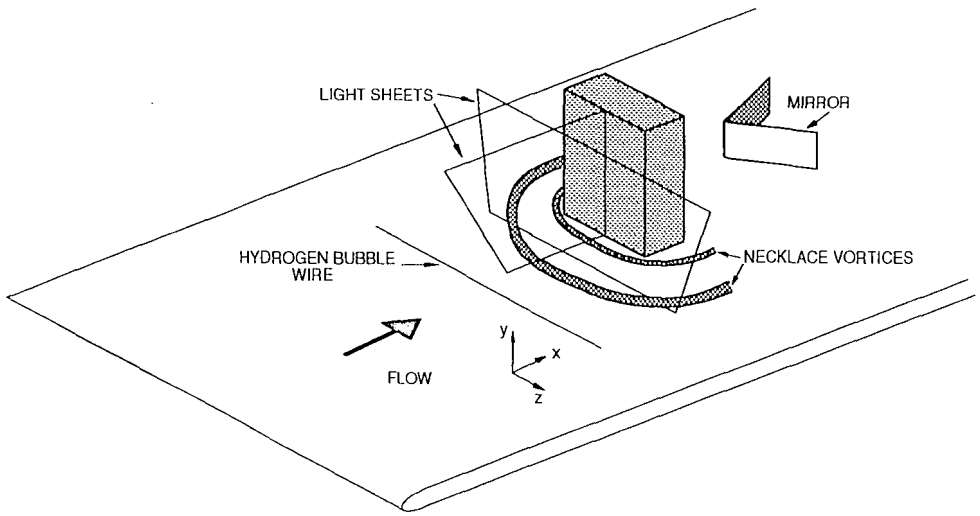

Figure 2.3 Schematic of light-sheet illumination and end-view mirror.

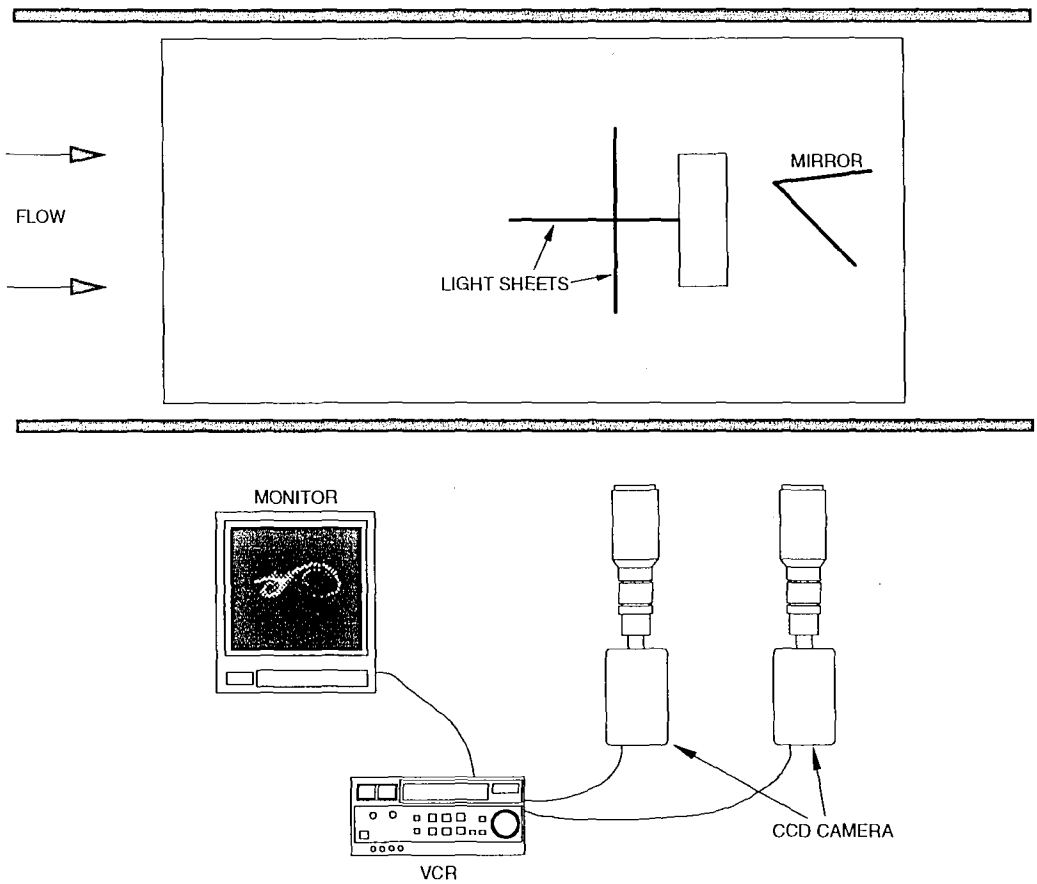

Figure 2.4 Plan-view schematic of video system and camera locations.

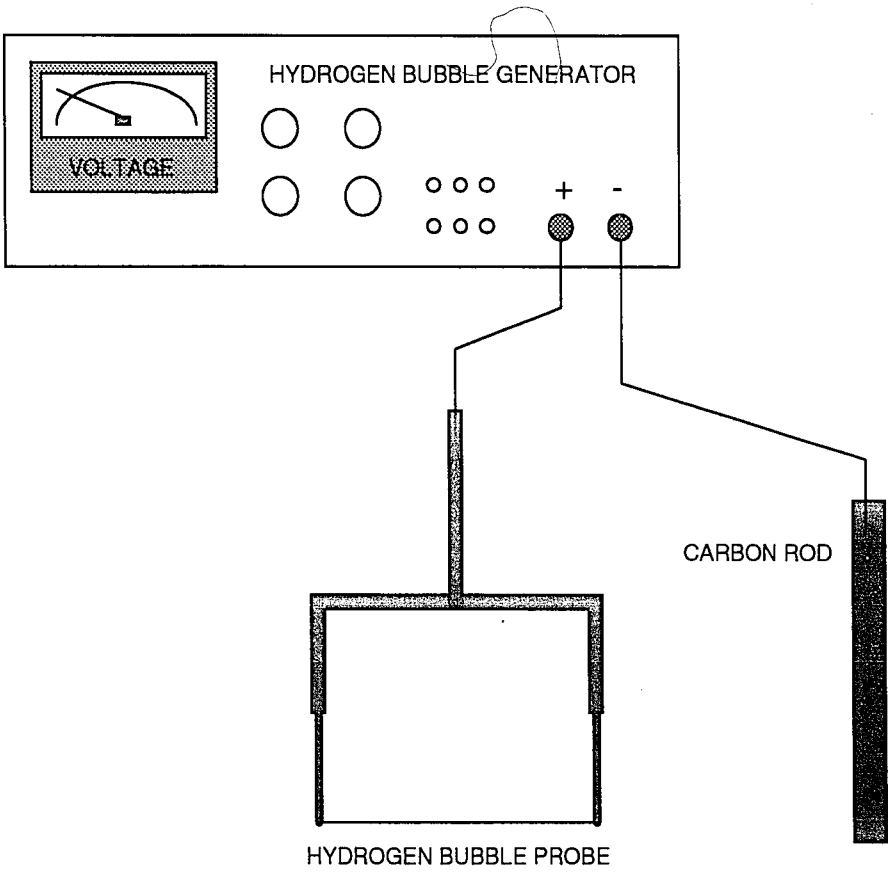

Figure 2.5 Schematic of hydrogen bubble equipment.

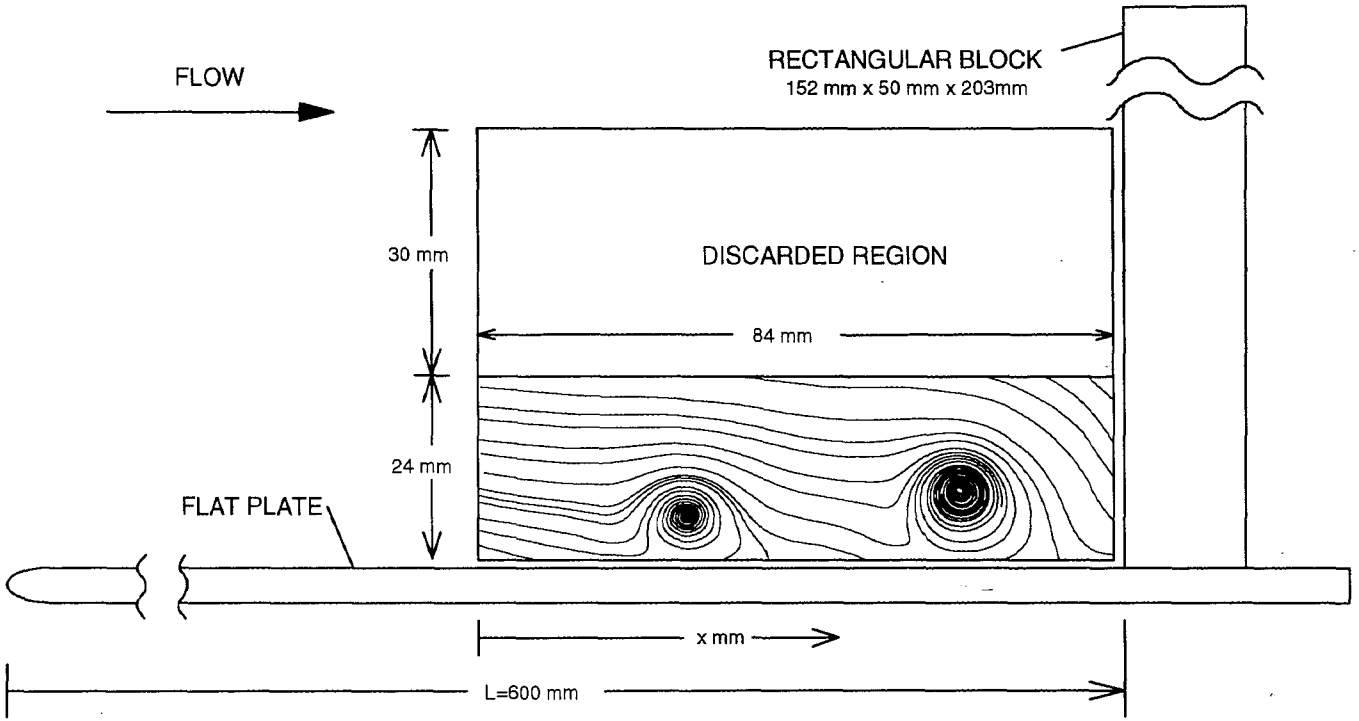

Figure 2.6 Schematic of rectangular block mounting and field of view. U_∞=50.4 mm/s, Re_{δ^*}=298, $Re_L=3x10^4$.

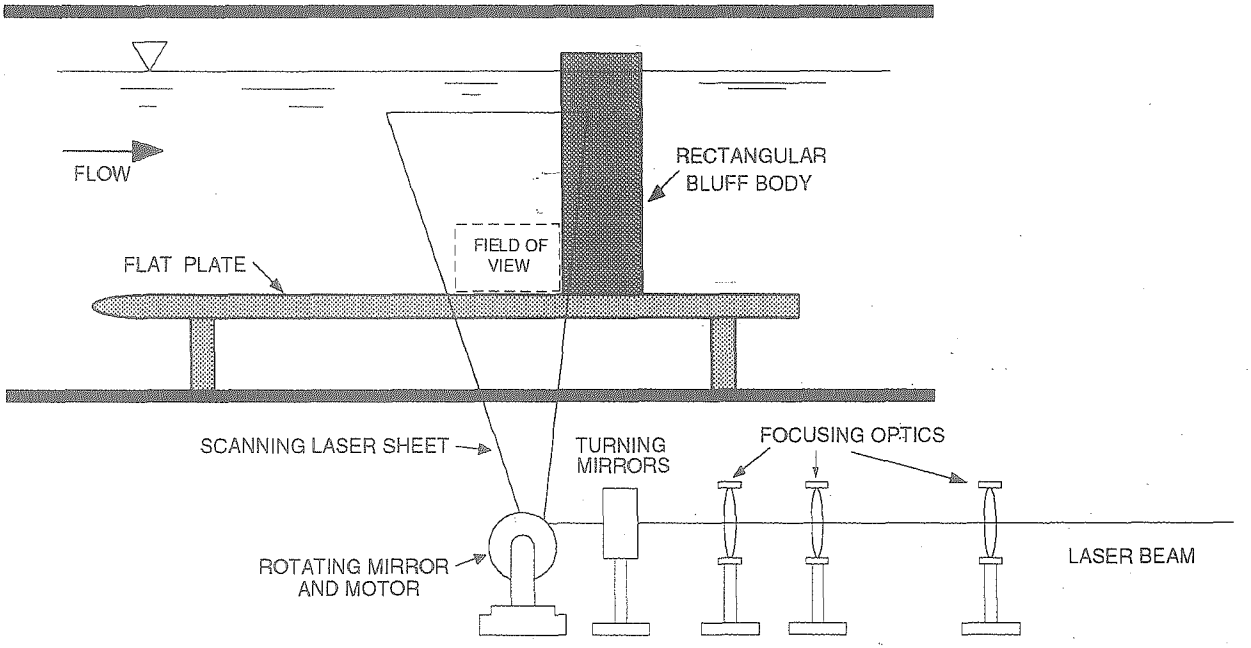

Figure 2.7 Side-view schematic of PIV experimental apparatus, including laser system.

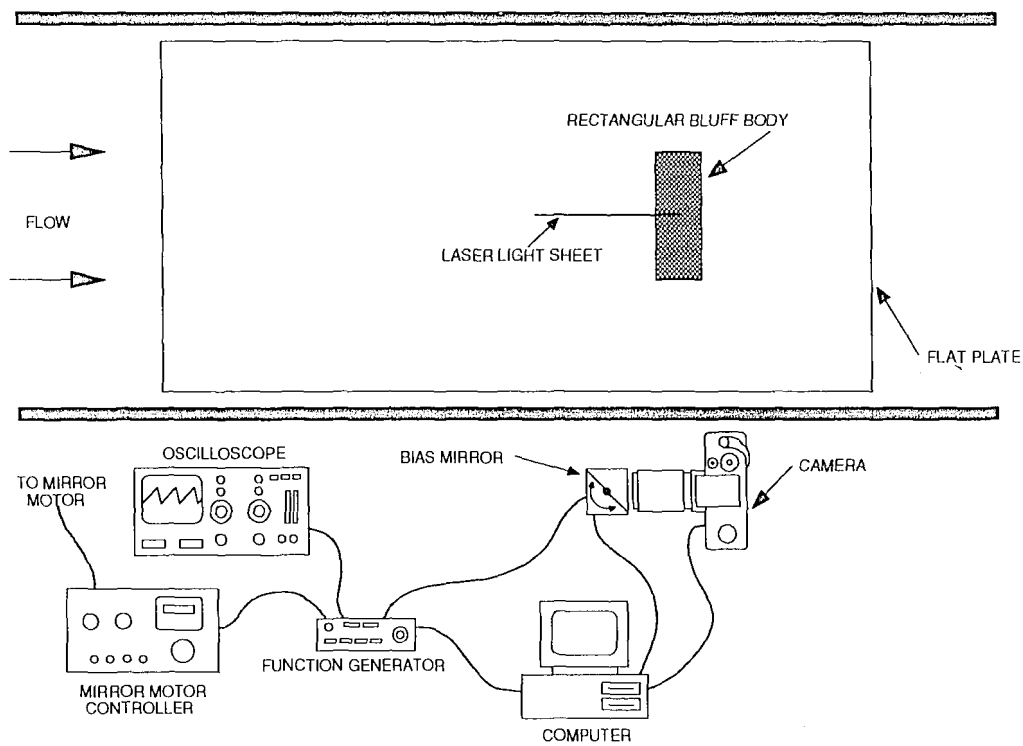

Figure 2.8. Plan-view schematic of PIV experimental apparatus, showing orientation of the bias mirror.

3.0 EXPERIMENTAL RESULTS and DISCUSSION (FLOW REGIME BEHAVIOR)

3.1 INTRODUCTION

This section describes the results of the flow visualization experiments performed to qualitatively determine and characterize the behavior of the laminar necklace vortex system formed at the junction of a flat plate-rectangular body over a range of flow parameters. This section also discusses the implications of the results. It must be noted that the qualitative results of this study are extremely similar to the sequence of flow regimes noted by Greco (1990) for cylinder junction flows. The regimes observed in the present study and their behavior are quite similar, except for slight differences in the transitional regime and the absence of a three-vortex system. For this reason much of the analysis of the results presented for this study re-present the conclusions of Greco; in particular the discussion of the visualization results and the models of flow behavior in the different regimes are quite similar.

3.2 OBSERVED FLOW REGIMES

3.2.1 GENERAL

As mentioned in section 1, a number of distinct regimes of flow behavior for a necklace vortex system are known to exist, with the regime of behavior depending on the flow velocity, block geometry, and boundary layer characteristics. For a fixed block geometry at a specific location, the flow passes through several ordered regimes of behavior as the flow velocity is increased, with switch over zones (zones where two

adjacent types of behavior are exhibited simultaneously) sometimes developing. The regimes observed, in order of appearance are:

Regime 1 - One-vortex - A steady, single necklace vortex is formed
Regime 2 - Two-vortex - A steady, two-vortex system develops
Regime 3 - Oscillating - The two vortices of regime 2 oscillate slightly out of phase with each other
Regime 4 - Amalgamating - The primary vortex (the vortex closest to the body) breaks away from the formation region and advects towards the block, but is then drawn back to and amalgamates with the secondary vortex (the vortex following the primary vortex), forming a new primary vortex. Amalgamation is a periodic event for which frequency increases as Re increases;
Regime 5 - Breakaway - The primary vortex periodically breaks away from the formation region and advects downstream towards the body. The frequency of break away increases with increasing Re;
Regime 6 - Transitional - The entire system destabilizes into a non-symmetric, three-dimensional, transitional behavior.

This ordered progression is the same for all block geometries and locations, although the velocity range over which a particular behavior is observed varies with block dimensions and boundary layer thickness. In the following sections, the results obtained for the 5.1 cm wide block located 0.6 m from the leading edge of the test plate will be used to describe and illustrate a typical progression.

3.2.2 REGIME 1 - STEADY, SINGLE NECKLACE VORTEX

The first regime observed, beginning at Re $_{\delta}$*=148 (where Re$_{\delta}$* is the Reynolds number based on the equivalent displacement thickness for an unobstructed boundary layer at the block location) and U_{∞}=1.23 cm/s, was that of a single, steady necklace vortex formed upstream of the block approximately 3.3 cm from the block, with a diameter of about 1.1 cm (Figure 3.1 illustrates this schematically). This initial necklace

vortex, and all subsequent vortices, have a clockwise rotation (negative vorticity) for flow from left to right. The necklace vortex deforms symmetrically around the block; the legs extend downstream as shown in Figures 1.1 and 1.2, where they eventually break down or are entrained in the Strouhal vortices present behind the block.

Previous studies of the necklace vortex system formed in the end wall of a cylinder (Greco, 1990) indicate that no necklace vortices are observed to form at initially low Reynolds numbers (Re_D=750, Re_{δ}*=200).. This was not the case for the rectangular blocks employed in the present study. At the lowest Reynolds numbers examined (Re_W=621, and Re_{δ}*=60), a single necklace vortex was still present. The reason for this difference is unclear, but it is probably due to either 1) the differences in the lateral pressure gradients of the respective buff bodies or 2) the failure at low Reynolds numbers of the hydrogen bubble visualization technique used in the Greco (1990) study (as opposed to the IPV technique used in the present study). It is of course probable that the single necklace vortex would have disappeared if the present study could have been extended to lower Reynolds numbers.

3.2.3 REGIME 2 - STEADY, TWO-VORTEX SYSTEM

As the flow speed is increased to 1.5 cm/s (Re_{δ}*=166), a second, smaller and weaker, secondary vortex develops upstream of the primary, or first vortex. For the 5.1 cm block, the primary vortex develops approximately 3.7 cm away from the block (with a diameter of approximately 0.9 cm); the secondary vortex forms about 5.4 cm from the block (diameter approximately 0.6 cm). The secondary vortex is initially very weak, but gains strength as the flow speed is increased. In addition, a small counter-rotating vortex develops between the two vortices near the plate surface. This steady, two-vortex system

is shown in Figure 3.2, which is a hydrogen bubble visualization of this regime, augmented by a streamline schematic.

3.2.4 REGIME 3 - OSCILLATING

As the flow speed increases to 2.5 cm/s (Re_{δ^*}=210), the beginning of unsteady, periodic motion of the necklace vortices is noted, as the two vortices of the previous system begin to periodically oscillate relative to each other. The primary and secondary vortices are observed to move towards each other, reaching a minimum separation distance, and then move away from one another, reaching a maximum separation distance, whereupon the process repeats periodically. Figure 3.3 illustrates this behavior. The process begins as the primary vortex begins to move downstream away from the formation region (beginning about 4.2 cm from the block, with a diameter of approximately 0.9 cm), losing strength as it advects; the secondary vortex begins to gain strength (beginning about 5.5 cm from the block, with a diameter of about 0.5 cm), as it also moves downstream (Figure 3.3 i-iv). The primary vortex reaches a maximum distance from the secondary vortex and then reverses direction (at about 3.3 cm from the block and a diameter of approximately 0.7 cm) moving back towards the secondary vortex, which continues downstream to about 4.9 cm from the block with a diameter of about 0.7 cm (Figure 3.3 iv-v). The primary vortex continues moving upstream, reaching a minimum separation distance from the secondary vortex, which returns it to its original location and size; the secondary vortex weakens and moves upstream, also returning to its original location and size (Figure 3.3 v-vii). Note that the amplitudes of the oscillation are relatively small compared to subsequent regime behavior, with the oscillation of the primary vortex generally greater than that of the secondary vortex. The

frequency of this oscillatory behavior increases as the flow speed increases, and is not a function of the Strouhal shedding frequency.

Previous studies of the necklace vortex system formed in front of a cylinder (Greco, 1990) indicate that for a cylinder, the natural progression was for a third, tertiary vortex to generally develop immediately upstream of the secondary vortex, for both the steady and unsteady modes. However, for the block geometries examined in this study, no tertiary vortex was observed to develop; however further study, particularly with a smaller block, might prove otherwise.

3.2.5 REGIME 4 - AMALGAMATING

A further increase in flow speed to 2.8 cm/s (Re_{δ^*}=223) results in the periodic, amalgamating behavior illustrated in Figure 3.4. Within this regime, the primary vortex forms (approximately 4.3 cm from the block with a diameter of about 0.8 cm) and begins to move downstream and weaken, while the secondary vortex develops about 5.4 cm from the block, continually increasing in strength (Figure 3.4 i-iii). The primary vortex then reverses direction, moving back towards the secondary vortex, where it passes beneath and amalgamates with the advancing secondary vortex (Figure 3.4 v-vi) to form a new primary vortex (at about 3.8 cm from the block) (Figure 3.4 vii); the process then repeats periodically. The formation of a new secondary vortex initiates as the first primary and secondary vortices are amalgamating.

3.2.6 REGIME 5 - BREAKAWAY

At U_∞=5.0 cm/s (Re_{δ^*}=299) the flow changes to the breakaway flow behavior illustrated in Figure 3.5. Here the necklace vortices periodically develop, break away from the formation region, and move downstream to the corner region of the block-plate

junction. In fact, the behavior is similar to regime 4, except that the point of amalgamation of the two vortices moves downstream to the corner region of the block-plate junction. The cycle begins when a completely formed primary vortex breaks away from the formation region (breaking away at about 5.0 cm from the block with a diameter of about 0.6 cm) and advects towards the block (Figure 3.5 i). When it reaches the corner region (with a diameter approximately the same as when it left the formation region), the primary vortex amalgamates with an existing corner vortex, forming a new corner vortex of about 0.6 cm diameter (Figure 3.5 vi-vii). This corner vortex remains in the corner region (decreasing over time to a diameter to about 0.4 cm) until it amalgamates with another arriving primary vortex After the primary vortex breaks away, the secondary vortex becomes the new primary vortex and a new secondary vortex begins to develop (Figure 3.5 ii-vi). Note that for the case considered here (i.e. with the 5.1 cm square block 0.6 m from the leading edge of the plate) the primary vortex does not appear to decrease in size as it is advected downstream, as was the case for the previously described regimes. The initial formation of the vortices takes place about 6.5 cm from the block when regime 5 behavior first initiates, moving out to 6.7 cm from the block just before transitional behavior develops. Note that the frequency of the breakaway process generally increases linearly with increasing Re.

3.2.7 REGIME 6 - TRANSITIONAL REGIME

At U_∞=18 cm/s (Re_δ*=570) and beyond, the necklace vortex system loses both symmetry and periodicity. The vortices first become kinked along their length, forming hairpin-like distortions, and then break down into the complicated three-dimensional flow pattern of the fully-transitional regime. The process begins when small disturbances in the flow are amplified by the pressure gradient imposed by the block,

initially creating small kinks in the necklace vortices. At lower flow speeds these disturbances will damp out; however, above a critical flow speed the disturbances will affect the formation of new vortices due to a global feedback process, and the whole system will destabilize. At Reynolds numbers slightly below the critical Re, the flow may alternate between periods of breakdown and periodic coherence.

In the fully transitional regime, the flow is characterized by the formation of hairpin vortices (Figure 1.4) and generation of turbulent-like bursts of surface fluid emanating from the wall region into the outer flow, as well as the development of a highly-focused turbulent-like two-vortex system, like that described for regime 2, close to the block. The turbulent-like vortices appear sporadically, at varying distances from the block, and are deformed along their length (Figure 3.9 is a schematic of the fully transitional regime). Figure 3.6 is an oblique view of a typical visualization of the fully transitional regime, showing the hairpin generation. Figure 3.7 is an end view of the transitional regime (taken looking upstream through the clear block) showing one such visualized hairpin vortex, similar to the one pointed out in the oblique view in Figure 3.6. These hairpin vortices are advected downstream after formation, interacting strongly with the surface fluid adjacent to the flat plate, and subsequently move into the outer flow away from the wall or sometimes become entrained in the turbulent-like vortices. The surface interaction is a result of the legs of the necklace vortex focusing the surface fluid between them into sharp eruptions like the one illustrated schematically in Figure 1.4 and illustrated in an end view visualization sequence in Figure 3.8. Figure 3.8 used a transverse light sheet to visualize the interaction of a hairpin vortex, with the surface; a hydrogen bubble wire located on the surface of the plate just upstream of the light sheet facilitates visualization of the surface fluid. Figure 3.8 i shows the surface prior to interaction with a hairpin vortex. Figure 3.8 ii to 3.8 iv illustrate the initiation of an

eruption and the ejection of the surface fluid into the outer flow. Figure 3.8 v to 3.8 vi show the interaction of the ejected fluid with the outer flow.

The transitional regime of the laminar necklace vortex system contains a number of interesting phenomenon. Greco (1990) states that the temporal breakdown process of the laminar necklace vortex system "closely parallels the spatial transition of laminar flow on a flat plate", and the appearance of both the hairpin-like distortions of the necklace vortex before full transition and the hairpin vortices in the fully transitional regime reinforce the suggestion that hairpin vortices are important structures in turbulence initiation. Also it is at this point where the destabilizing effects of the combined effect of the adverse pressure gradient caused by the presence of the block and upstream disturbances advecting into the vortex system override the stabilizing effects of vortex stretching.

Greco (1990) provides an analogy of necklace vortex transition to flat plate transition which is re-presented here. He stated that the temporal breakdown of the coherent necklace vortices is much like the spatial transitional behavior of a boundary layer on a flat plate as described by White (1974). During flat plate transition, the development of Tollmien-Schlichting waves due to instabilities in the shear layers results in the development of spanwise vortices. The development of the necklace vortices closely resembles this behavior. Greco (1990) also states that the "three-dimensional distortions in the spanwise Λ-vortices which develop spatially during flat plate transition can be related to the hairpin-like distortions which develop temporally in the necklace vortices during their breakdown. The three-dimensionalities amplify non-linearly in both cases, leading to a rapid transition to disorganized flow behavior, a turbulent boundary layer in the case of a flat plate, and a turbulent junction vortex in the case of the cylinder-plate arrangement."

The appearance of hairpin vortices in the transitional regime deserves special consideration. The hairpin-like distortions appearing in the necklace vortices just prior to full transition suggest that the hairpins are integral to the transition process either as manifestations of the mechanism leading to transition or as a mechanism for amplification and propagation of three-dimensional disturbances in an unstable flow. Greco's (1990) description of the formation process of hairpin vortices in the fully transitional regime is capable of being applied here. That is, hairpin vortices form just downstream of the separation line (where the laminar boundary layer separates from the flat plate, marking the beginning of the three-dimensional separated region of the transitional regime). It appears the hairpin vortices form from the distortion of spanwise vortex tubes like those that develop into the necklace vortices of regime 5. The frequency of spanwise vortical structure formation also is much higher than the frequencies associated with regime 5 behavior, while the relative scale and strength of these spanwise vortical structures are less than those of the previous regimes. Greco (1990) postulates that this is due to a shorter formation time compared to previous regimes. Relatively strong three-dimensional disturbances from the distorted flow downstream are fed back into the formation region (just downstream of the separation line), quickly distorting the spanwise structures into the observed hairpin vortices. The hairpin vortices then lift away from the plate and advect downstream where they either move away from the plate and interact with the outer flow or amalgamate into the turbulent-like vortices mentioned above. The mutual induction of the hairpin vortex legs is most likely the reason the hairpin vortices lift away from the plate. Haidari (1990) states that hairpin vortices may act as turbulence generating mechanisms, developing subsidiary vortices and introducing three-dimensionalities into the flow. The hairpin vortices of the transitional regime play just such a role in the progression from laminar

flow upstream of the separation line to the turbulent-like behavior near the block. Figure 3.9 is a general schematic of the transitional regime showing the various flow structures discussed above, and their interrelationship..

3.3 PHYSICAL INTERPRETATION and REGIME FLOW MODELS

3.3.1 GENERAL

The appearance of the necklace vortices and the behavior of the different flow regimes can be explained by considering the vorticity of the system and the laws governing vorticity and vortices. Initially vorticity is generated at the leading edge of the plate and advected downstream in the boundary layer as spanwise vortex lines. As these vortex lines enter the region of adverse pressure gradient upstream of the block, the block and pressure gradient prevent the vortex lines from continuing, and the vortex lines must remain continuous, the vorticity reorganizes into discrete vortices which deform around the body and extend downstream. What clearly needs to be addressed is how the organized vorticity interacts, and maintains a vorticity balance in the junction region.

Schwind (1962) used a conservation of vorticity approach to explain the existence of distinct flow regimes in the junction region of a 60° wedge-flat plate. He stated that as the free-stream velocity is increased, the flow regimes change behavior in order to diffuse the increased amount of vorticity being advected into the region, thus maintaining a balance of vorticity. These considerations can be applied to the flow regimes observed in the present study.

The vorticity transport equation:

$$\frac{D\omega}{Dt} = \omega \cdot \nabla V + \upsilon \nabla^2 \omega \qquad (1)$$

is used to evaluate the behavior of vorticity in the boundary layer near the block. This equation states that the rate of change of vorticity of a fluid particle in a time-dependent vorticity field is equal to the rate of deformation of vortex lines (vortex stretching and tilting) plus the net rate of viscous diffusion. A closed rectangular area ABCD (Figure 3.10) on the plane of symmetry is used to aid in the analysis, where sides AB and AD lie on the flat plate and rectangular block respectively, CD lies along a streamline in the irrotational free-stream, and BC is normal to the mean flow and well upstream of the adverse pressure gradient created by the block. The balance of vorticity for a steady flow requires that the rate of vorticity advected in side BC must equal the rate of vortex stretching plus the rate of viscous diffusion at surfaces AB and AD (or in this case, the rate of opposite sign vorticity generated at these surfaces due to the adverse pressure gradient). Note that both steady and unsteady regimes were mentioned previously, however the unsteady regimes behave in a consistently periodic way and thus may be viewed as quasi-steady with respect to vorticity since the total time mean vorticity within the circuit over one cycle does not appear to change (Greco, 1990).

Another useful relation can be arrived at by taking the limit of the Navier-Stokes equation in the streamwise direction as $y \rightarrow 0$, which gives:

$$\frac{\partial p}{\partial x} = -\mu \frac{\partial \omega_z}{\partial y}. \qquad (2)$$

This equation states that the rate of diffusion of vorticity from the plate is opposite and proportional to the strength of the local adverse pressure gradient.

Greco (1990) also used the theory of inviscid vortex dynamics to develop flow models for the various unsteady regimes. This method will be applied to the present study as well. Inviscid vortex dynamics state that a point vortex near a solid surface will be influenced by its image vortex in the surface. The velocity fields of both the real and the image vortex mutually influence each other, resulting in a mutual induction

phenomenon. In the present case, there are two solid surfaces in the vicinity of the vortex (the plate and the cylinder), and thus the influence of both images must be considered. Figure 3.11 illustrates how a single necklace vortex will be affected by the presence of the plate and block.

Also aiding in understanding the dynamics of the unsteady regimes are the results of several previous computational and experimental studies of the interaction of a vortex with a solid surface. In a computational study of the flow induced by a single vortex above an infinite plate, Peridier and Walker (1991) determined that a counter-rotating eddy will form below the vortex and near the plate. As time progresses, the induced counter-rotating eddy will gain strength and size, inducing a strong upflow between the eddy and vortex. This upflow will develop into a strong, narrowly focused eruption of vorticity bearing surface fluid away from the surface as the counter-rotating eddy itself becomes narrowly focused.

3.3.2 STEADY BEHAVIOR

Both the single vortex and two-vortex configuration (regimes 1 and 2) generate a local adverse pressure gradient beneath the main vortices which is superimposed on the adverse pressure gradient generated by the block. This local pressure gradient region promotes relatively high rates of opposite sign vorticity generation, which cross-cancels with the vorticity in the boundary layer providing a balance of vorticity (Greco, 1990). Greco (1990) states that the formation of the secondary vortex seen in regime 2 suggests that the influx of boundary layer vorticity, due to increased free-stream velocity, has become too great to balance with the opposite sign vorticity generated by a single vortex. Therefore, a second vortex forms to provide another region of intense opposite-sign vorticity generation. The increased amount of opposite sign vorticity generation is

partially reflected by the formation of the small counter-rotating vortex close to the plate, between the primary and secondary vortices.

3.3.3 UNSTEADY BEHAVIOR

The behavior of the unsteady regimes can be explained using the principles of vorticity conservation and vortex-surface interactions, in accordance with a model described by Greco (1990). The model for the oscillating regime (regime 3) will be discussed first, and then subsequent regimes will be explained as modifications of the same model.

As the oscillatory cycle begins, the primary vortex is advected downstream by the mean flow and weakens due to viscous diffusion and cross-cancellation with opposite-sign vorticity generated by its own interaction with fluid adjacent to the test plate surface (Figure 3.3 i-iii). As it weakens and approaches the block, the primary vortex is influenced by its image in the block, which forces it towards the plate, where it is advected upstream by both the reverse flow along the plate (created by the adverse pressure gradient due to the presence of the block) and the influence of its image in the plate (Figure 3.3 iv-vi). At the same time, the secondary vortex gains strength from vorticity transported from upstream. The counter-rotating structure associated with the interaction of the secondary vortex with the plate surface also gains strength, inducing the secondary vortex away from the plate and away from the influence of the pressure gradient-induced backflow (Figure 3.3 iii-v). As the two vortices come together (Figure 3.3 v-vii), the primary vortex strengthens by drawing vorticity from the incoming boundary layer, and the counter rotating structure associated with the primary vortex increases strength and undergoes an eruptive event analogous to, but not as drastic as, that observed by Harvey and Perry (1971) and computed by Peridier and Walker (1991)

(because the strength of the eruptive behavior is related to the Re of the vortex, which is relatively low for the present experiments). This interaction induces the primary vortex away from the plate, to its initial position; the interaction of the secondary vortex with the same counter-rotating structure both weakens the secondary vortex, and induces the secondary vortex toward the plate. The counter-rotating structure also seems to cut off the supply of vorticity to the primary vortex from the boundary layer. At this point, the vortices have returned to their original positions and the cyclic process repeats. Greco (1990) states that the primary reason for the development of unsteady behavior at this point is that the main vortices are now generating subsidiary structures of sufficient strength to destabilize the flow and interact with and affect the surrounding flow. In fact, as the induced counter-rotating structures gain strength (due to the increase in the strength of the main vortices, as the free-stream velocity increases) they exert progressively greater influence on the flow, resulting in the different behavioral regimes.

The amalgamating regime (regime 4) flow mechanics are essentially the same as regime 3, with a few modifications at the point the primary and secondary vortices come together. The primary and secondary vortices encounter one another and, being of like sign, coalesce, with the primary vortex passing under and into the secondary vortex, forming a new primary vortex. During this coalescence, the counter-rotating structures associated with the main vortices merge and a relatively strong eruptive event marking the beginning of the cycle occurs (Figure 3.4 v-vii). This strong eruptive event at the beginning of the cycle serves to separate the primary vortex from the formation region and stop the feeding of boundary layer vorticity generated at the leading edge of the plate into the vortex. The breakaway regime flow mechanics are the same as for regime 4, except that a strong eruptive event severs the forming primary vortex from the formation region and the point of amalgamation has moved to the corner region of the block-flat

plate junction. The flow mechanics of the breakaway regime are discussed in more detail in section 4.2.

3.4 PARAMETRIC FLOW REGIME CHARACTERIZATION

The previous study of Greco (1990) mapped flow regime behavior for a cylinder as a function of the flow parameters Re_{δ^*} and δ^*/D. A similar parametric flow regime characterization is used in the present study, and the results are compared to Greco's cylinder-plate junction results. For the present study, a dual functionality of flow regime on Re_{δ^*} and δ^*/W is suggested. Figures 3.12 and 3.13 are plots of the flow regime zones as a function of Re_{δ^*} and δ^*/W (Figure 3.13 is an expanded view of the region near the origin). One can see that the regimes fall into fairly consistent areas of the map. From this data Figure 3.14 was constructed, which shows the lines of flow regime transition. Note in Figure 3.14 that the solid lines indicate lines of transition obtained using the data obtained in the present study, whereas the dashed lines are extrapolated lines of transition covering flow parameter ranges for which no experimental data was obtained. The dashed lines were based on extrapolation of the experimental data and Greco's (1990) inferences about flow regime behavior discussed below.

Boundary layer flow on a flat plate will, at a critical Reynolds number, become transitional regardless of the presence of a block. Therefore, the curve representing transition is expected to asymptote to the critical Reynolds number of the plate as illustrated in Figure 3.14 (Greco, 1990). Since the strength of the local adverse pressure gradient becomes minimal as the width of a block becomes very small, and the formation of necklace vortices appears to be pressure gradient induced, the curve representing the transition from no vortices to regime 1 should approach the asymptote for transition to a

turbulent boundary layer flow as δ^*/W increases (Greco, 1990). Also, as $\delta^*/W \rightarrow \infty$ (i.e. $W \rightarrow 0$) one expects the local adverse pressure gradient due to the presence of the block to become negligible and the flow on the plate to act like an unobstructed boundary layer flow.

Figures 3.12 through 3.14 suggest that no single parametric relationship correlates the flow regime. However the maps can be used to observe several trends and draw conclusions as to the nature of the necklace vortex system. Figure 3.14 shows that the degree of instability of the flow, as shown by the progression from steady to unsteady to transitional behavior, increases with increasing Reynolds number. Also, it is observed that decreasing W appears to stabilize the flow (i.e. as δ^*/W increases, the transition to more unstable regimes occurs at higher Reynolds numbers). It was mentioned previously that the formation of necklace vortices and their subsequent destabilization are pressure gradient driven phenomenon. This suggestion is supported by noting that as block width is decreased (increasing δ^*/W), the strength and extent of the adverse pressure gradient and its effect on the boundary layer decreases, which suggests that the formation and destabilization of necklace vortices should be delayed to higher Reynolds numbers, as is suggested by Figure 3.14. For comparison, the previous results of Greco are overlaid on the results of the present study in Figure 3.15. The comparison suggests markedly similar behavior.

3.5 PRESSURE GRADIENT CHARACTERISTICS

The upstream, non-dimensional pressure and pressure gradient for an inviscid approach flow to a rectangular obstacle along the plane of symmetry was calculated to examine the potential role that the adverse pressure gradient generated by the block plays

in the development of the necklace vortex system. Figure 3.16 plots the non-dimensional pressure $(p-p_0)^*$ and non-dimensional pressure gradient dp^*/dx^*. The solution method used assumed that the blocks examined in the present study could be represented as semi-infinite blocks (i.e. the block extends to infinity in one direction as seen in Figure 3.16). The pressure curve increases smoothly from a free-stream value to the stagnation pressure at the block wall, providing nothing of real value for the analysis of the necklace vortex flow; however, the pressure gradient curve does provide some insight into the flow behavior. Note, that the inviscid solution will be modified due to the presence of the local pressure gradients induced by the necklace vortices, but the general behavior of the inviscid solution is helpful in evaluating the observed flow behavior.

Beginning at about x/W=-1.5 the pressure gradient increases rapidly to its maximum at about x/W=-0.37 and then decreases rapidly to 0.0 at the block wall. The results of the flow visualization indicate that most of the necklace vortices form from about x/W=-1.1 to x/W=-.7. According to Greco (1990) this suggests that the formation of the necklace vortices is tied to the rapid increase in pressure gradient. Previously (section 3.2.3) it was mentioned that the downstream vortices in multiple, steady systems (i.e. regime 2) were stronger than the upstream vortices, which suggests that the proximity of a vortex to the point of maximum pressure gradient influences the strength of a vortex. For example, referring to Figure 3.16, the primary (stronger) vortex in regime 2 forms at approximately x/W=-0.73, where the non-dimensional pressure gradient is a little less than twice that at x/W=-1.06, (the formation location of the secondary vortex); this supporting the suggestion that proximity of a vortex to the point of maximum pressure gradient influences its strength. It should also be noted that the maximum rate of opposite-sign vorticity generation due to the pressure gradient occurs at the point of maximum pressure gradient. Also note that the limiting form of the Navier-

Stokes equation at y=0 (section 3.3.1) indicates a direct link between vorticity generation and the surface pressure gradient. Thus, to a good approximation Figure 3.16 indicates that the generation of opposite-sign vorticity will occur in approximately the same distribution over the surface as the pressure gradient. Variations in this process will occur due to the generation of local differences due to the development of discrete vortices.

3.6 FREQUENCY BEHAVIOR OF UNSTEADY REGIMES

As mentioned above, the frequency of events in the unsteady, periodic regimes (oscillating, amalgamating, and breakaway regimes) increases with increasing free-stream velocity when block geometry and location are held constant. The term 'events' is used to denote any periodic behavior of the system (i.e. the frequency of oscillations, amalgamations, or breakaways). The frequencies were obtained by measuring the time elapsed for a certain number of events using video playback of extended recorded sequences. The frequency behavior was established to not be related to the Strouhal shedding frequency.

In general, the frequency is a function of flow velocity, block geometry, boundary layer thickness, and fluid viscosity. Dimensional analysis suggests several possible dimensionless groups which could govern this periodic behavior, including (fW/U, Re_W, & Re_{δ^*}), ($f\delta^*/U$, Re_{δ^*}, & δ^*/W), or ($f(\delta^*)^2/\upsilon$, Re_{δ^*}, & δ^*/W). The functionality of these groups is examined below and in plots of reduced frequency data.

Figure 3.17 shows the relationship between dimensionless frequency (fW/U) and Re_W for the 5.1 cm square block. Note that there appears to be a strong linear relationship above Re_W=2,000, with a roughly parabolic behavior for lower Re_W. Note

also the decrease in slope of the frequency curve, as well as a decrease in frequency at a given Re_W as the block x-location (distance from the leading edge) is increased, clearly a result of the increasing boundary layer thickness, δ. Similar frequency trends were also observed by Greco, although he only included the frequency of events for regime 5, effectively excluding the range below Re_W=2,000. Figure 3.18 similarly plots fW/U vs. Re_W for the 15.24 cm wide block, which suggests that as block width increases a strong deviation from linear behavior occurs. Greco (1990) also observed a similar deviation from linear frequency behavior for larger diameter cylinders. Also, note that the data in Figure 3.18 obtained with the block located 0.1 m from the leading edge falls well below its expected position (i.e. above the other curves, which would follow the frequency and slope trend described above). This is most likely due to an interaction of the leading edge of the plate with the pressure gradient generated by the block. Figure 3.16 suggests that the inviscid pressure gradient at the leading edge for the 15.24 cm block at 0.1 m (x/W=-0.67) would be very high ($dp^*/dx^* \approx 0.5$), whereas for the 5.1 cm block at 0.1 m the pressure gradient at the leading edge (x/W=-2.0) is much less ($dp^*/dx^* \approx 0.1$). When the block is moved downstream and the leading edge is no longer in the high pressure gradient region, the anticipated frequency behavior returns, reinforcing the suggestion that for the 15.24 cm block at 0.1 m an interaction of the pressure gradient with the leading edge is influencing vorticity generation at the leading edge, which will impact the stability of the system, and thus the frequency of the flow behavior. Also, the curve for 0.1m exhibits a strange discontinuity at the lower end ($Re_W \approx 15{,}000$). This again is likely due to the interaction of the pressure gradient with the leading edge. Because of the suspected interaction of the leading edge with the pressure gradient for the 15.24 cm wide block at 0.1 m, the frequency data corresponding to this case was not included in the subsequent plots.

In an attempt to establish a single functional relationship for the necklace vortex frequency, several alternative plots were examined using the various dimensionless groups suggested by dimensional analysis (see above). Figure 3.19 is a plot of fW/U_∞ vs. Re_δ^*. This does not collapse the data, but does illustrate the dependence of the slope of individual curves on block width and x location. Figure 3.20, a plot of $f\ \delta^*/U_\infty$ vs. Re_δ^*, is another attempt at collapsing the data, however it is evident that it is inadequate. The most effective of plots was $f(\delta^*)^2/\nu$ vs. Re_δ^*, which compressed the data into a relatively narrow band as shown in Figure 3.21. A linear curve fit suggested a fit of $f(\delta^*)^2/\nu=0.03974(Re_\delta^*)-4.33384$, with a correlation coefficient of 0.956. The lack of data between the 5.1 cm square block at 1 and 2 m, seen on Figure 3.21, would likely be filled if data were taken at some locations in between, therefore the equation generated is most likely biased a bit downward. One must note, however, that the effect of the block width is not reflected in the plot parameters, $f(\delta^*)^2/\nu$ and Re_δ^* of Figure 3.21; however, Figure 3.21 indicates that block width does cause a variation in the range over which a periodic frequency is noted. No group of parameters was found that could collapse the data into one functional relationship.

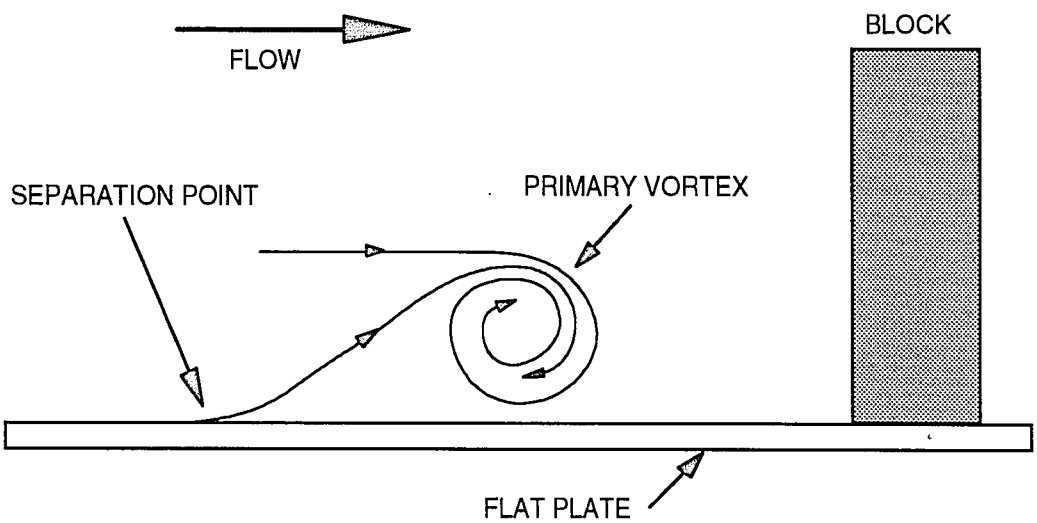

Figure 3.1 Symmetry plane streamline schematic of regime 1 (steady, single-vortex).

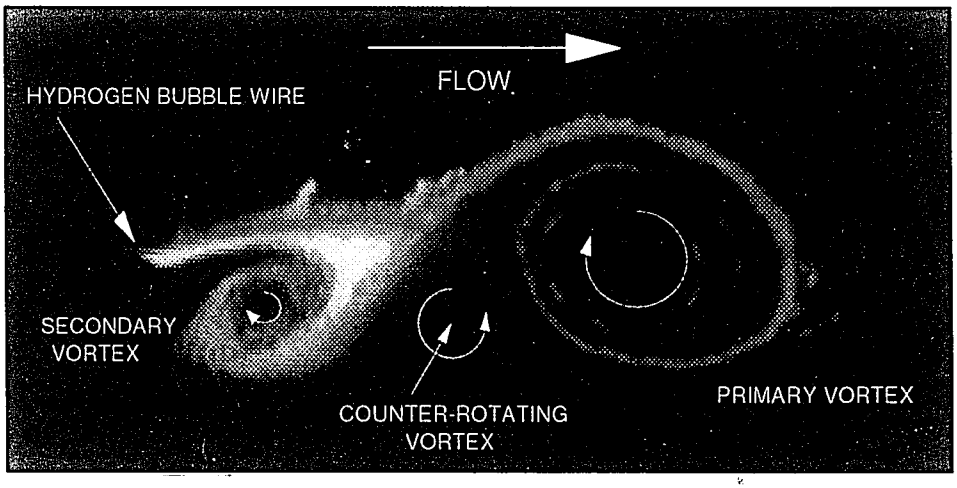

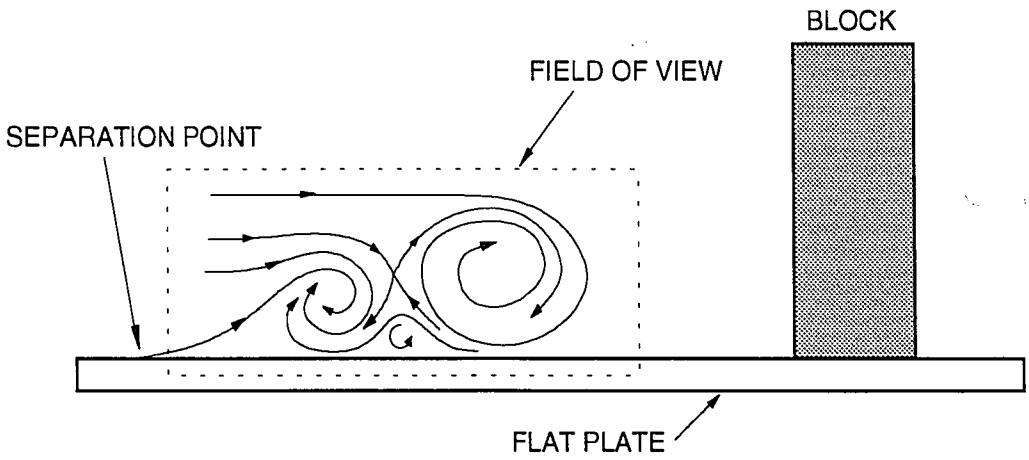

Figure 3.2 Hydrogen bubble visualization and streamline schematic of regime 2 (steady, two-vortex).

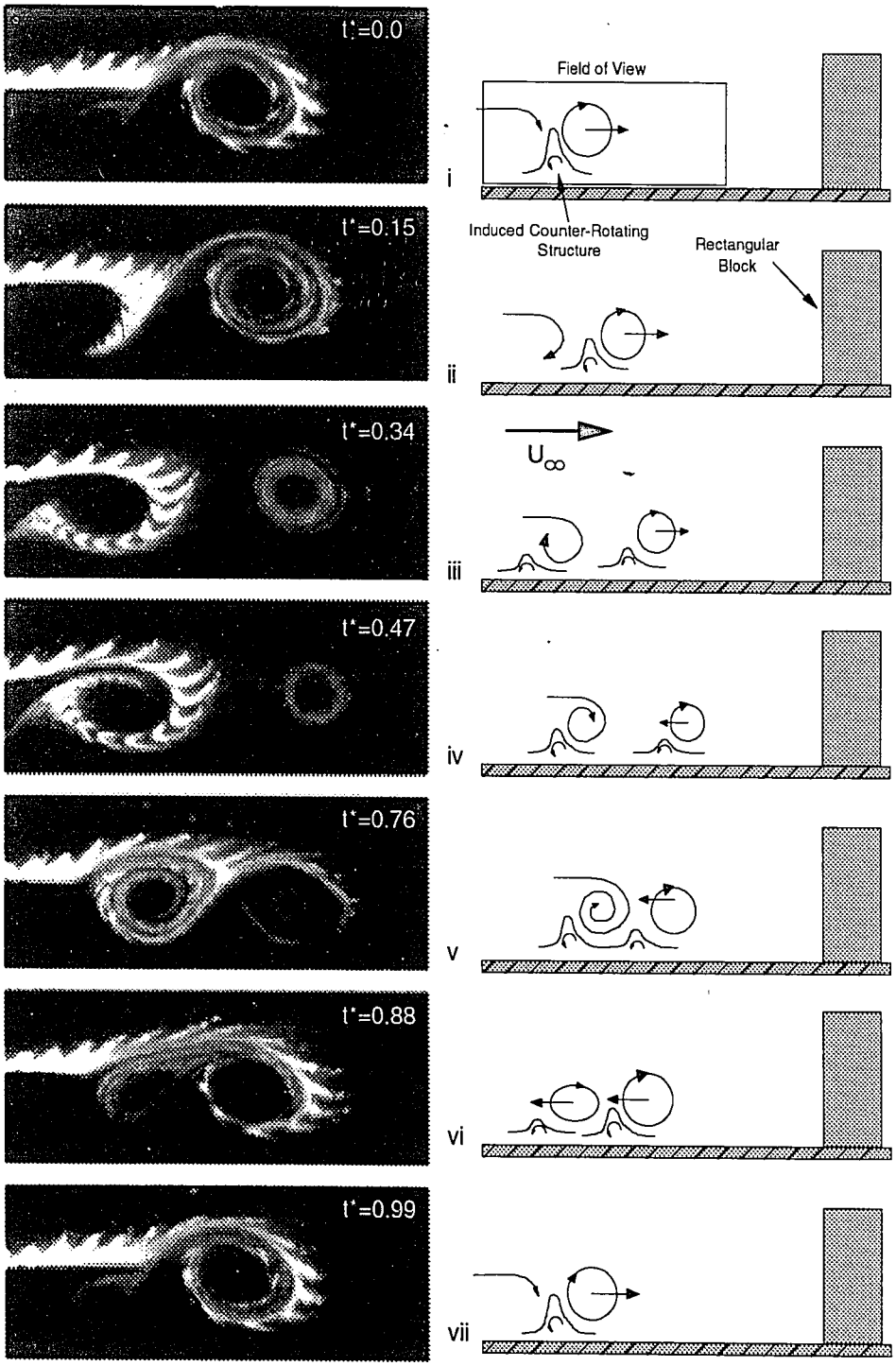

Figure 3.3 Hydrogen bubble visualization and corresponding schematic time sequence of the oscillating regime (regime 3), where $t^*=t/T$ (t=time and T is the period of one cycle). The height of the induced counter-rotating structures is a relative measure of their strength.

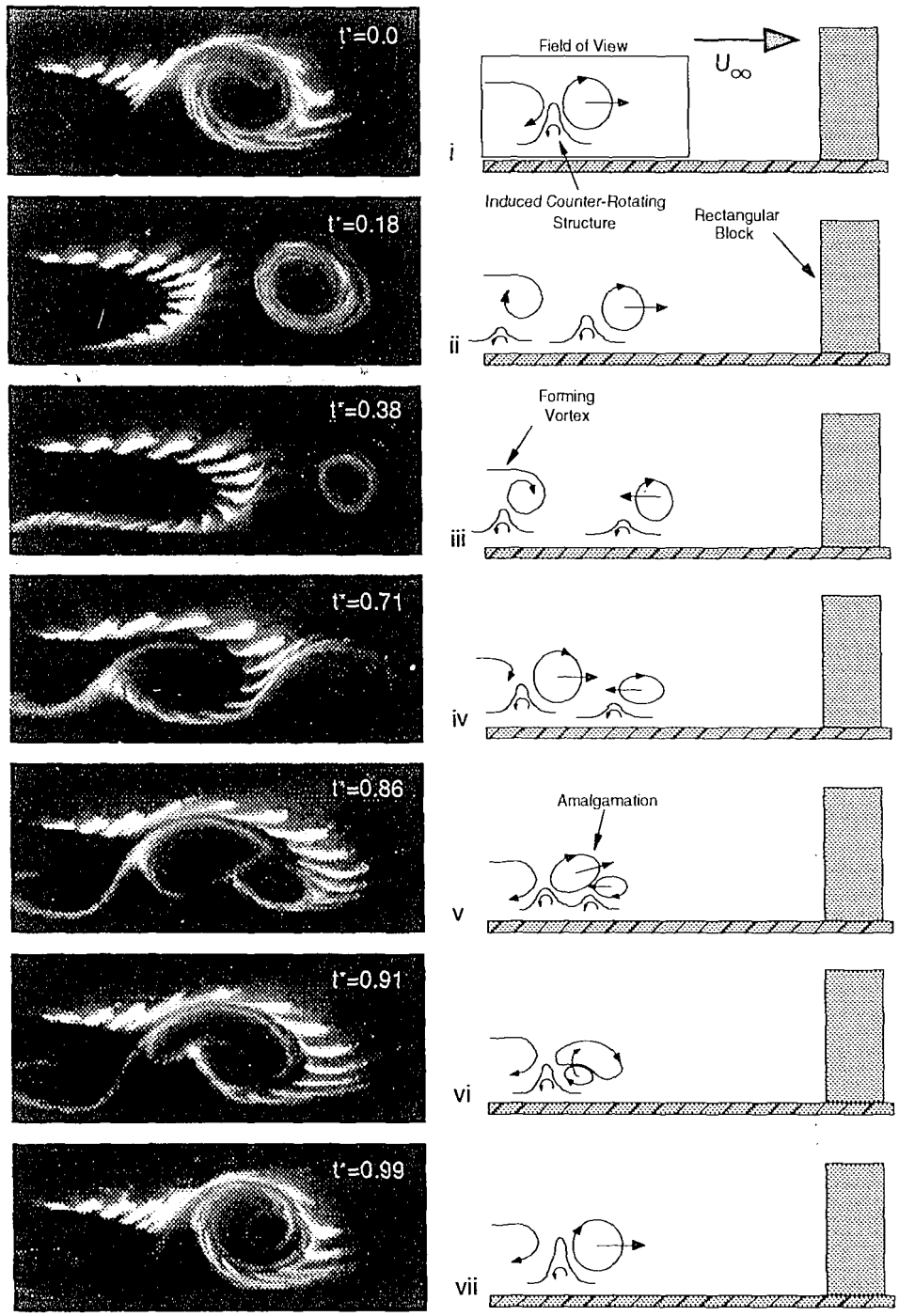

Figure 3.4 Hydrogen bubble visualization and corresponding shematic time sequence of the amalgamating regime (regime 4), where $t^*=t/T$ (t-time, T is the period of one cycle). The height of the induced counter-rotating structures is a relative measure of their strength

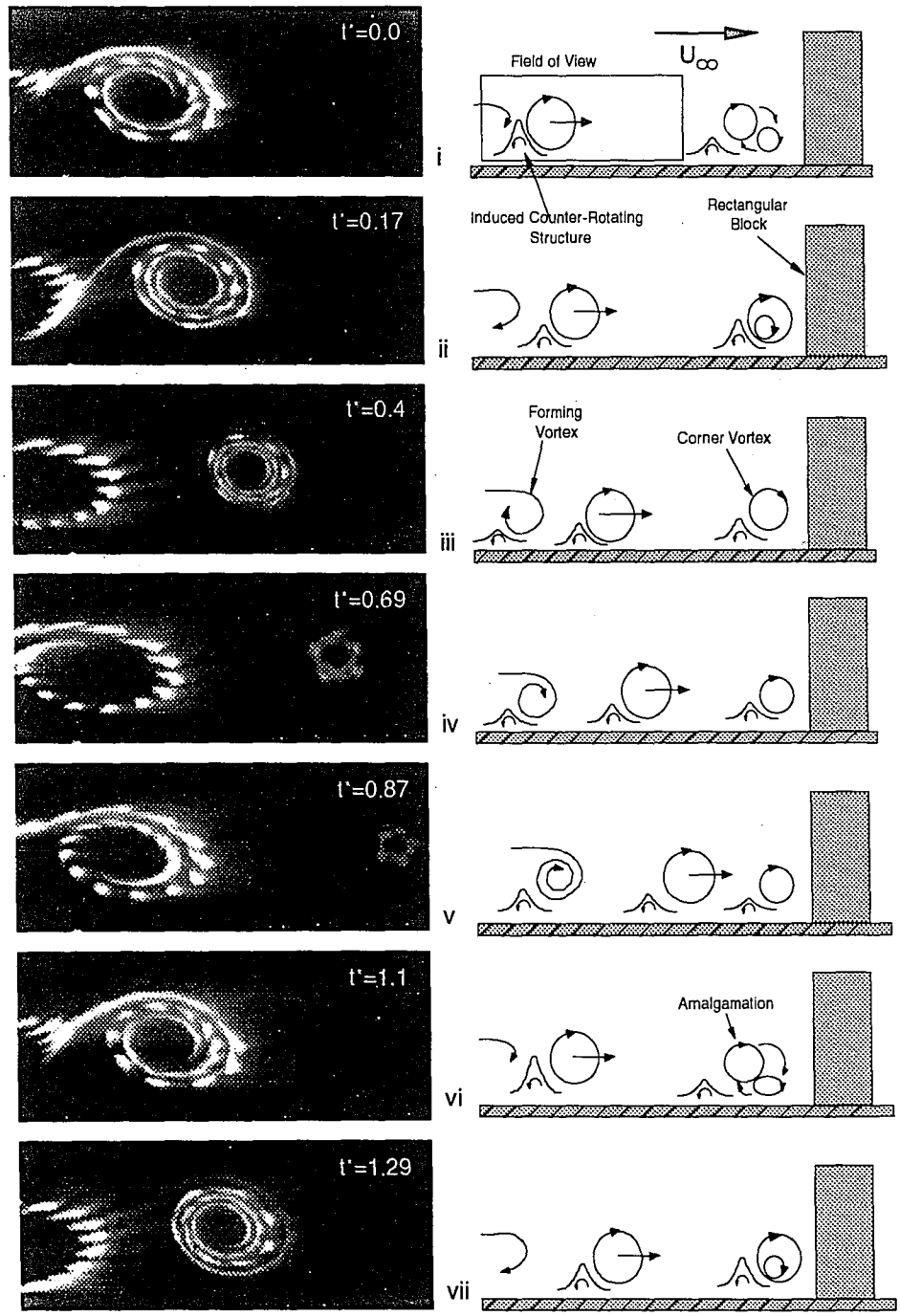

Figure 3.5 Hydrogen bubble visualization and corresponding schematic time sequence of the breakaway regime (regime 5), where $t^*=t/T$ (t=time and T is the period of one cycle. The height of the induced counter-rotating structures is a measure of their relative strength

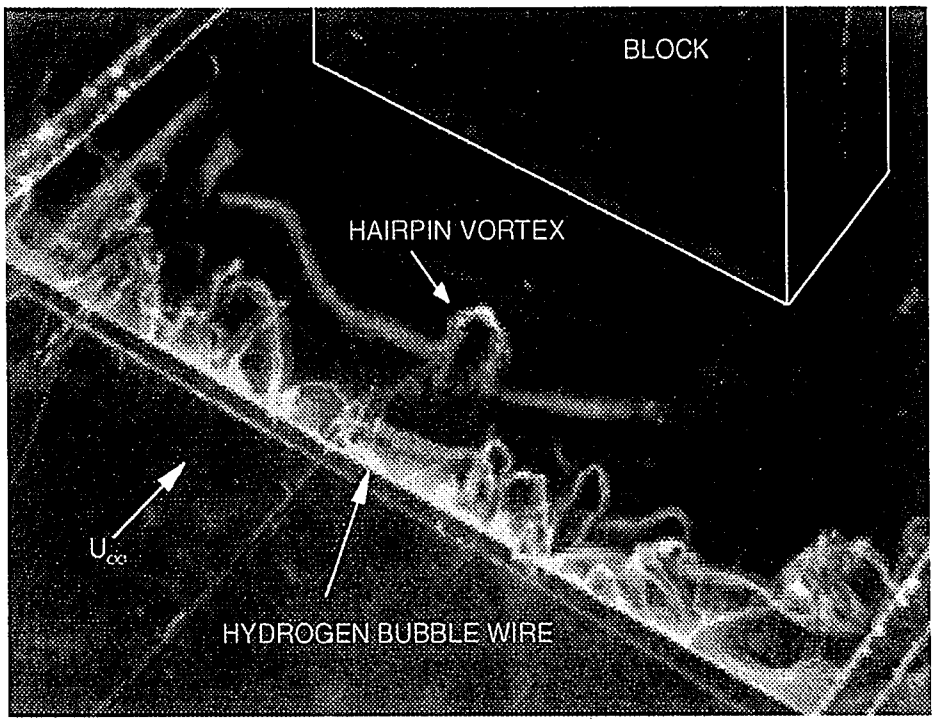

Figure 3.6 Oblique view hydrogen bubble visualization of the transitional regime showing the formation of hairpin vortices.

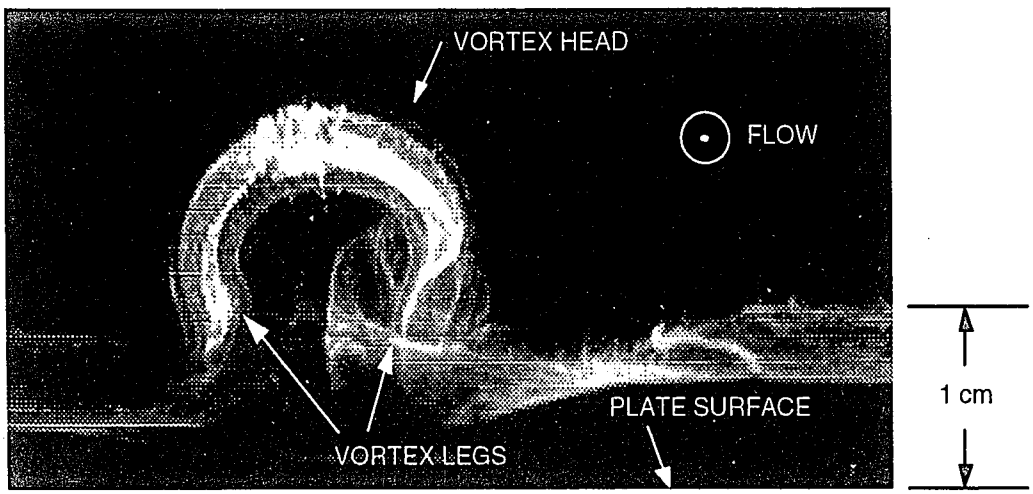

Figure 3.7 End-view hydrogen bubble visualization of a hairpin vortex in the transitional regime.

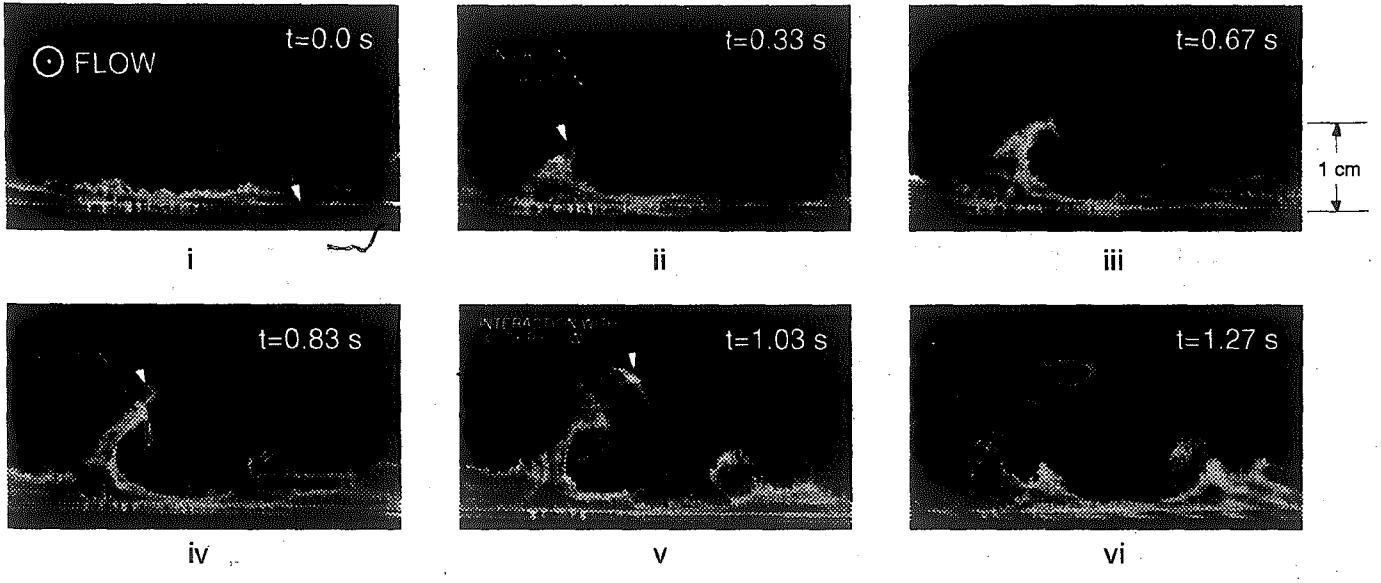

Figure 3.8 End-view hydrogen bubble visualization of the interaction of a hairpin vortex in the transitional regime with the surface. The hydrogen bubble wire is located in the plate surface, just upstream of the transverse light sheet.

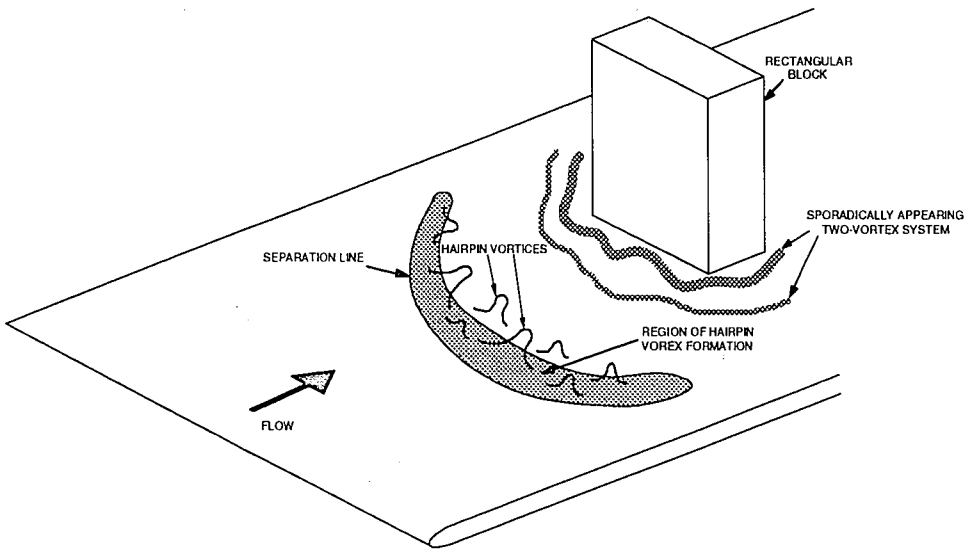

Figure 3.9 Schematic of transitional regime.

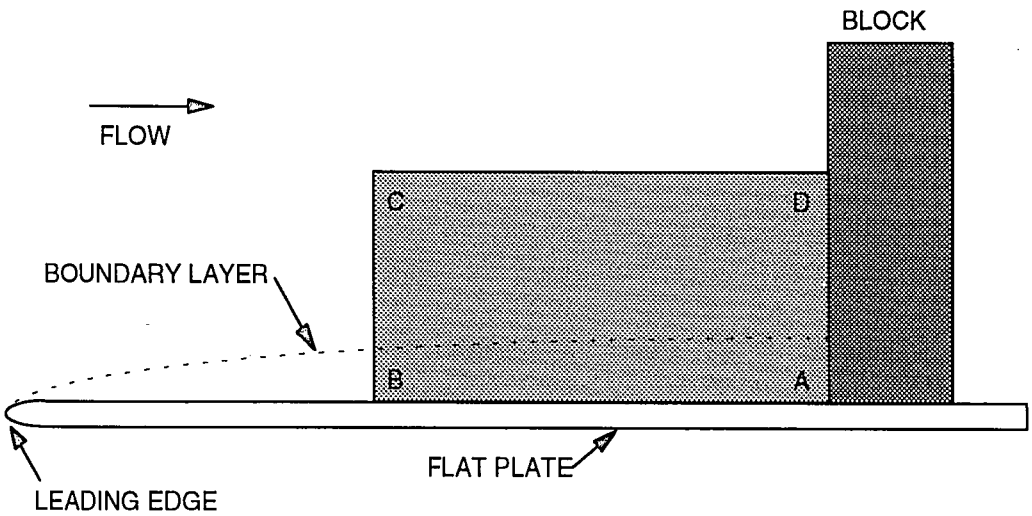

Figure 3.10 Control surface used to aid physical interpretation of the results.

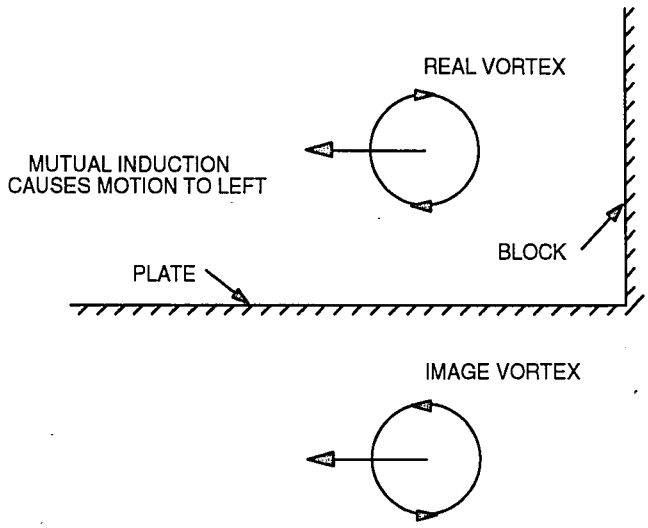

a) Mutual induction due to image vortex in the plate.

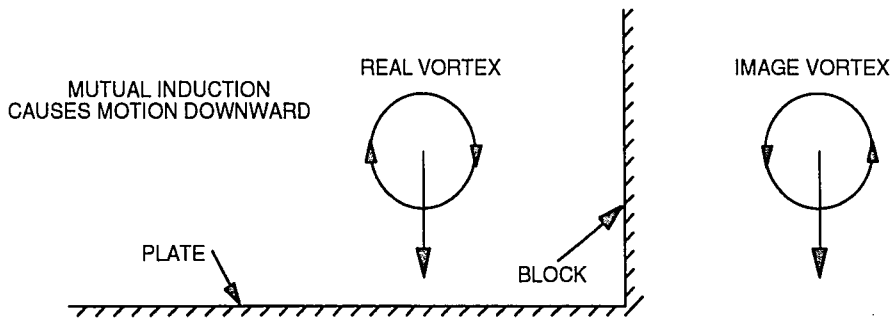

b) Mutual induction due to image vortex in the block.

Figure 3.11 Mutual induction effects by image vorticity for a single necklace vortex.

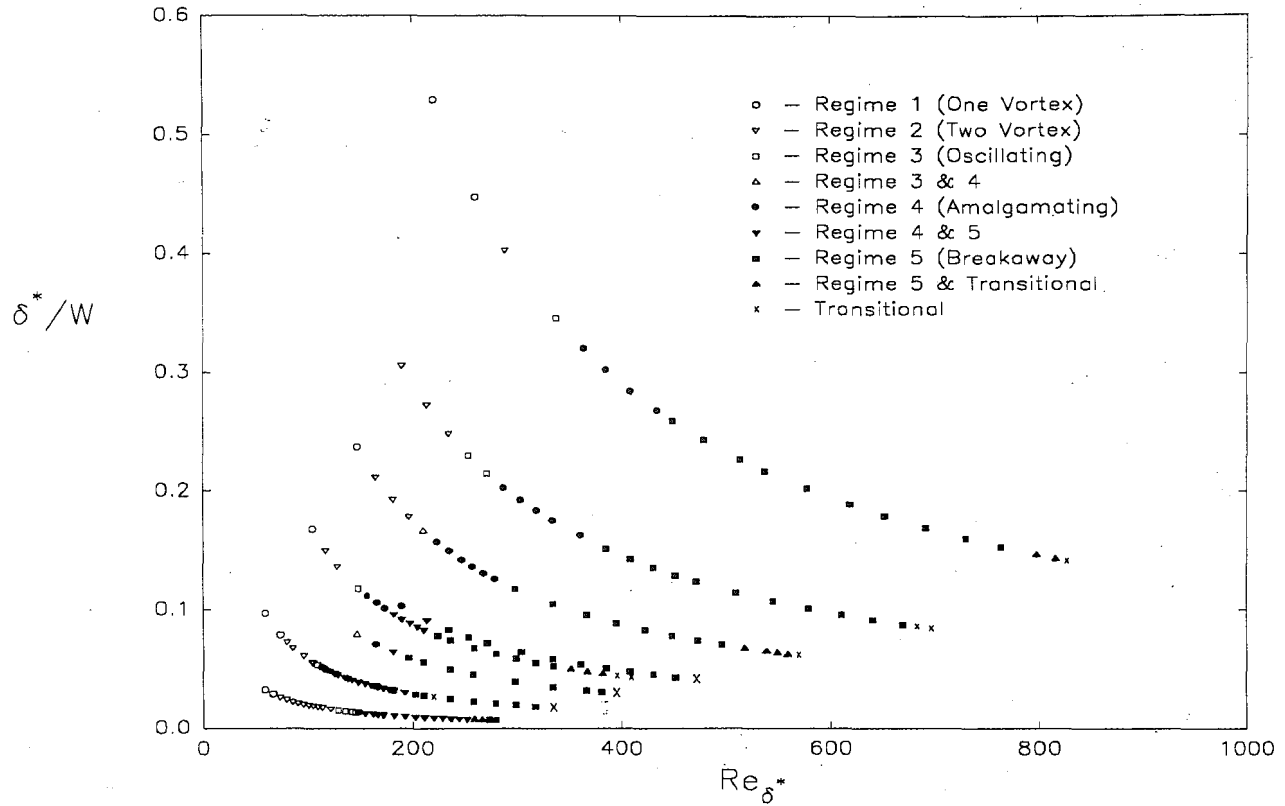

Figure 3.12 Flow regime plotted as a function of δ^*/W and Re_{δ^*} for both the 5.1 cm and 15.24 cm wide block.

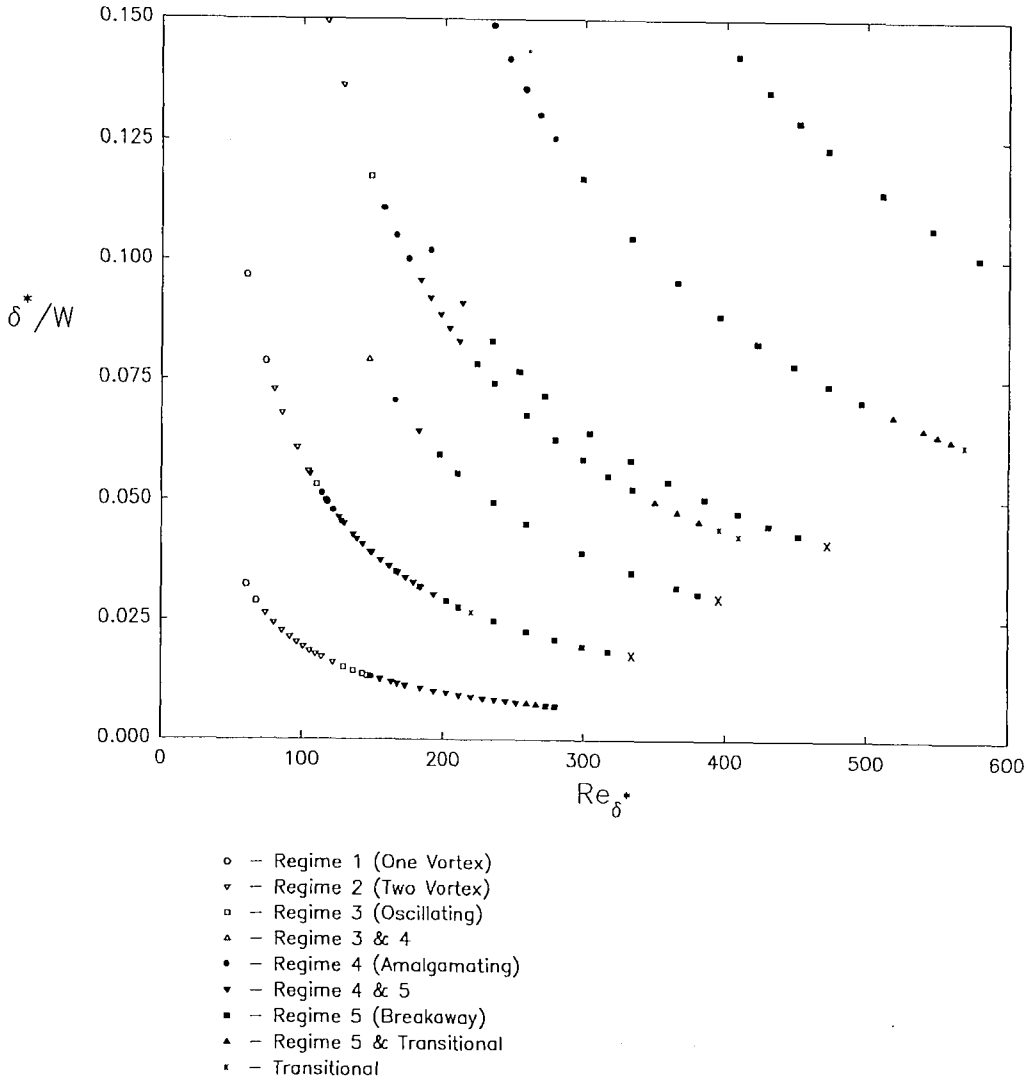

Figure 3.13 Flow regime plotted as a function of δ^*/W and Re_{δ^*} for both the 5.1 cm and 15.24 cm wide block.

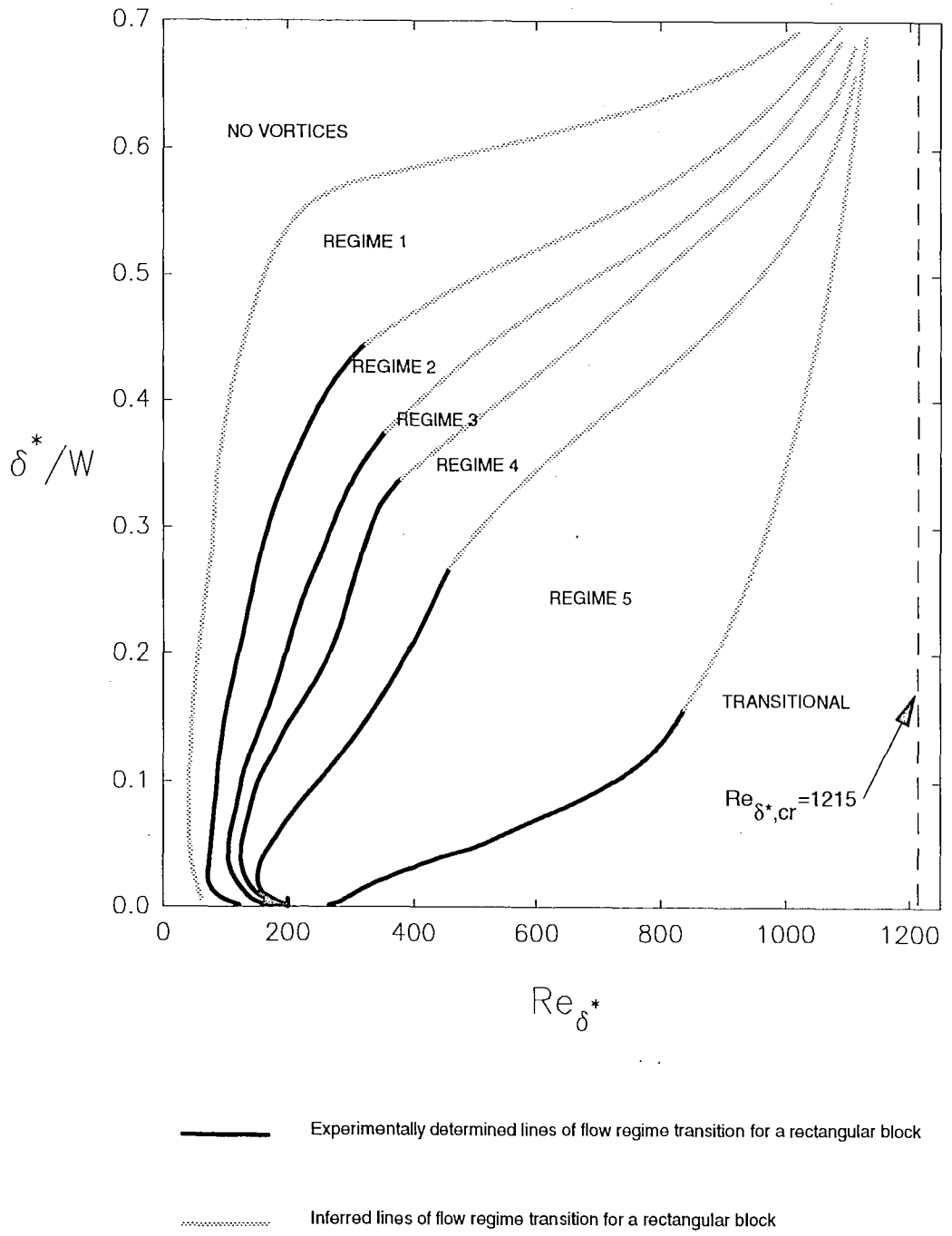

Figure 3.14 Lines of flow regime transition, based on Figures3.12 & 3.13.

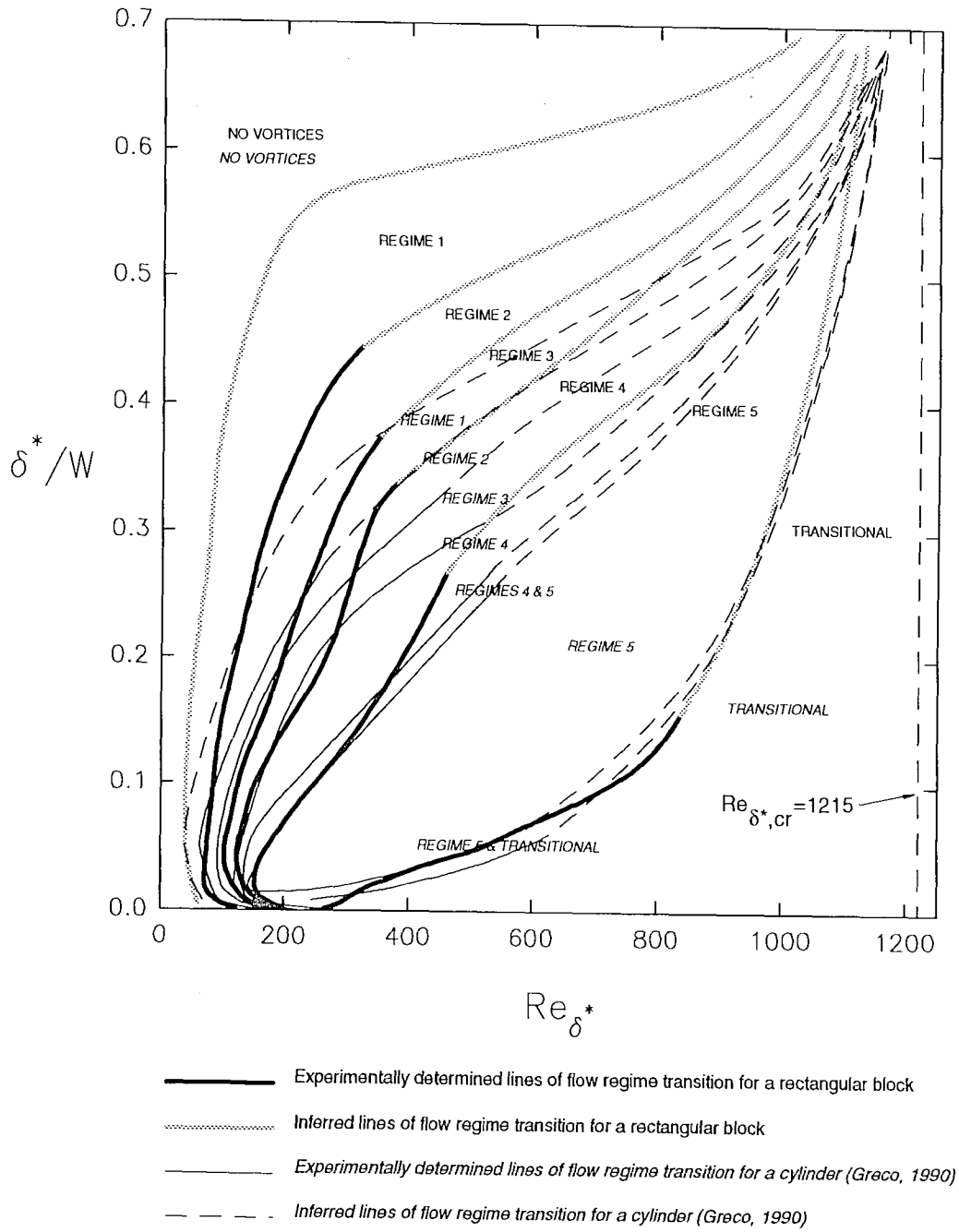

Figure 3.15 Comparison of rectangular block flow regime map to the flow regime map of a cylinder.

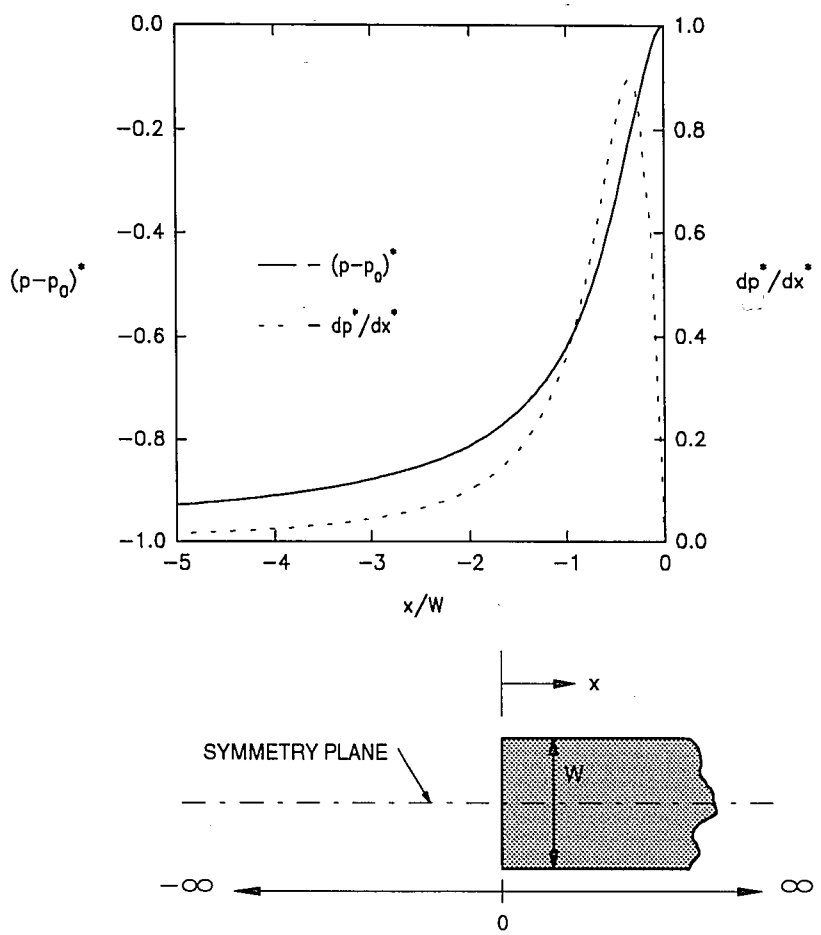

Figure 3.16 Dimmensionless pressure $(p\text{-}p_0)^*=2(p\text{-}p_0)/\rho U^2$ and pressure gradient $dp^*/dx^*=2W(dp/dx)/\rho U^2$ vs. x/W for an inviscid approach flow to a rectangular body, wgere p_0 is the stagnation pressure.

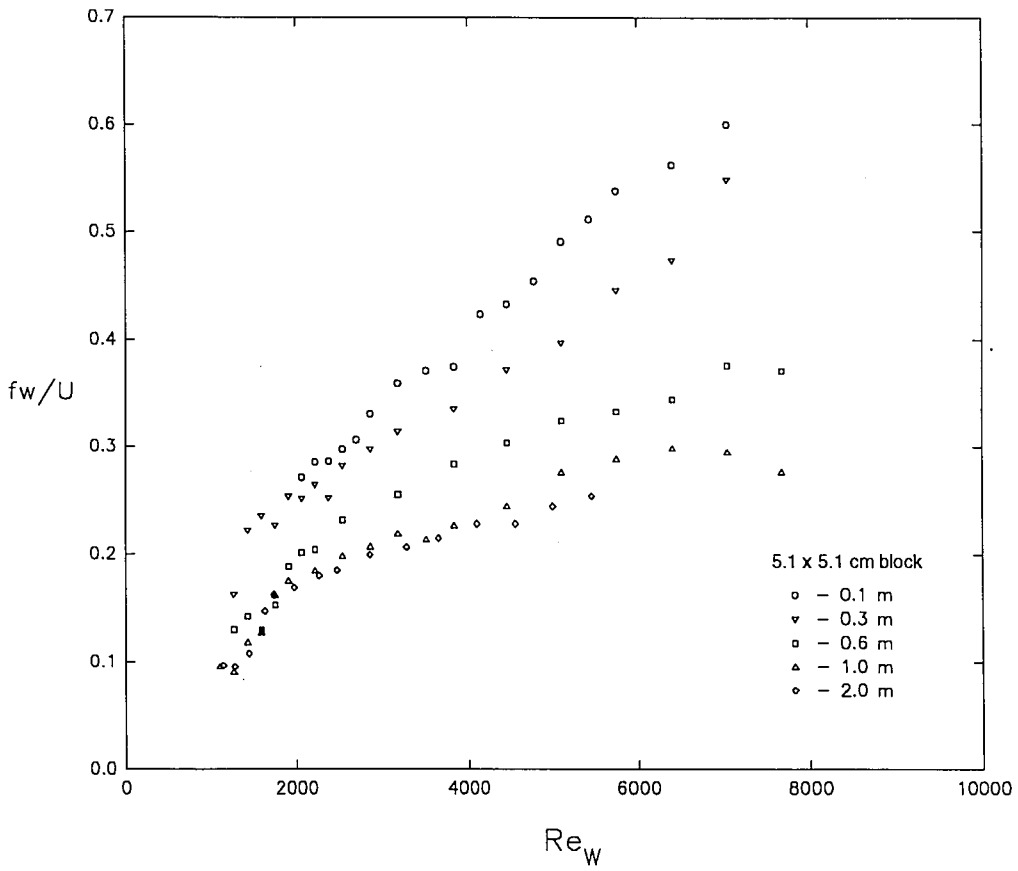

Figure 3.17 Normalized frequency data for the 5.1 cm x 5.1 cm block.

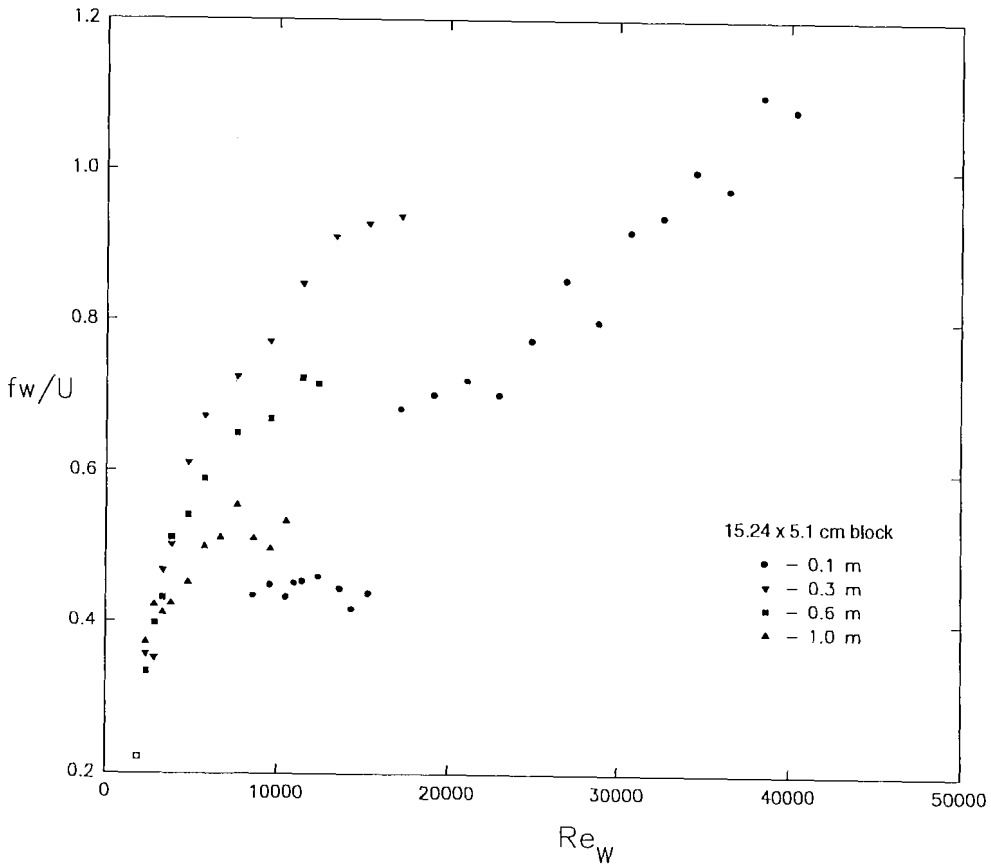

Figure 3.18 Normalized frequency data obtained for the 15.24 cm x 5.08 cm block.

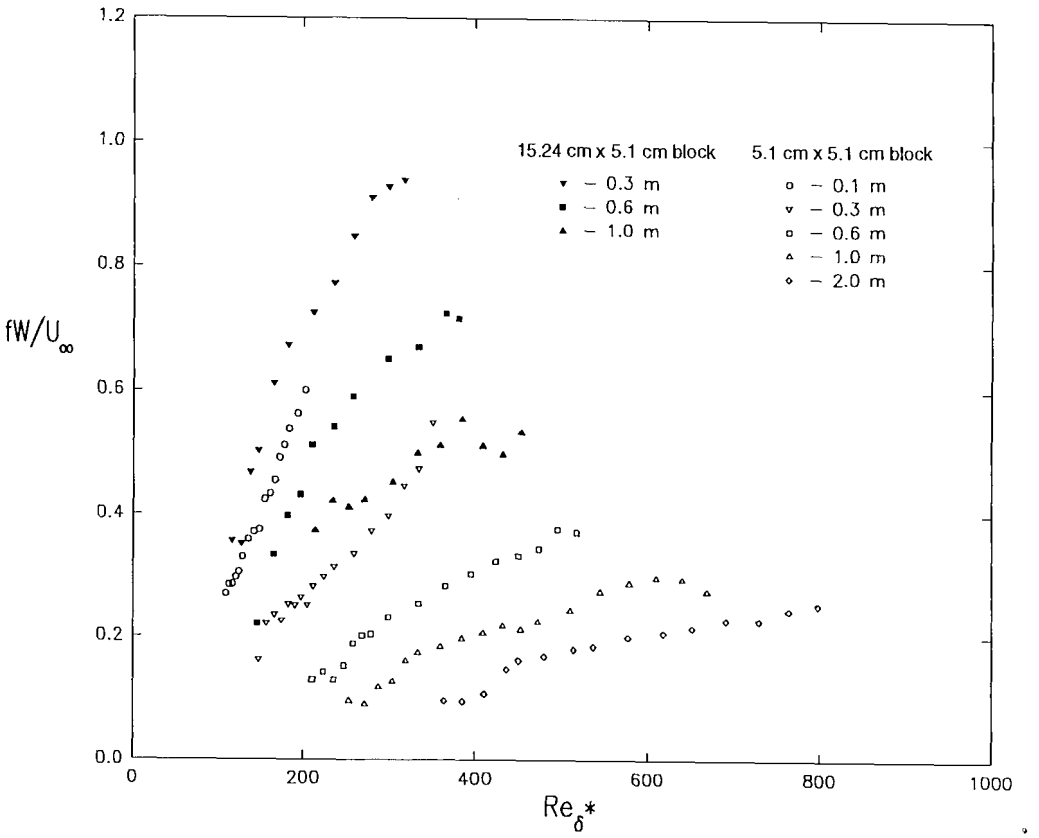

Figure 3.19 Normalized frequency for the 5.1 cm and 15.24 cm wide blocks.

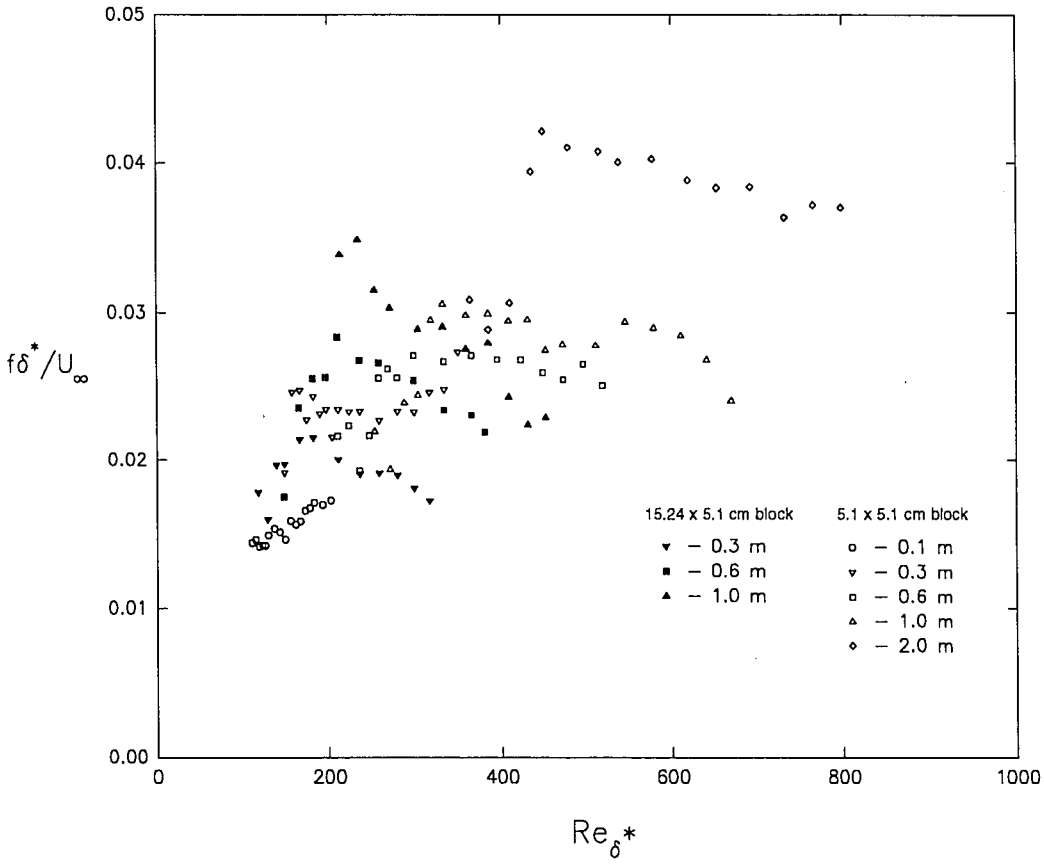

Figure 3.20 Normalized frequency data obtained for the 15.24 cm and 5.1 cm wide blocks.

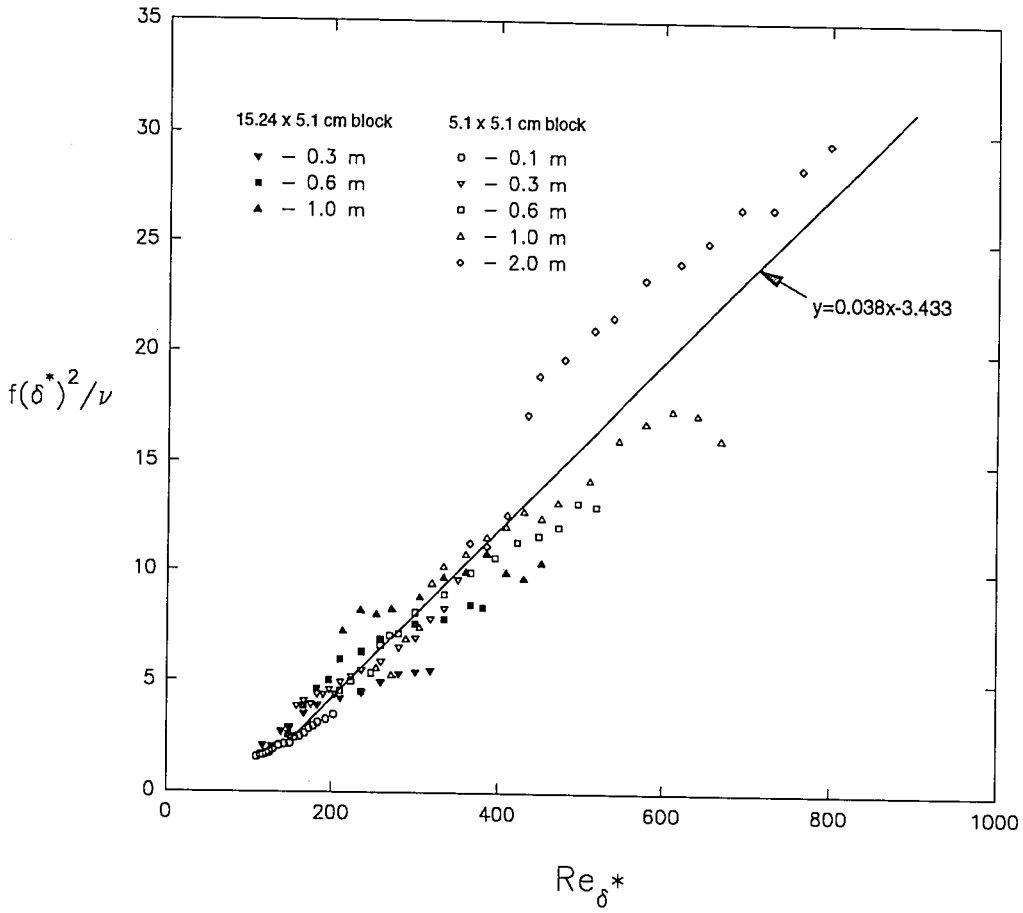

Figure 3.21 Normalized frequency data obtained for the 15.24 cm and 5.1 cm wide blocks and linear curve fit.

4.0 VELOCITY/VORTICITY FIELD BEHAVIOR of BREAKAWAY REGIME

4.1 INTRODUCTION

One particular case in the breakaway regime with the 15.24 cm body was studied using particle image velocimetry (PIV). This was done to obtain quantitative data for examination of both the character of the velocity and vorticity fields, the process of vortex decay and the vorticity balance, and the interaction of the vortices with the surface. For this particular case the block was mounted on the flat plate and the flow parameters set as described in section 2.7 (Figure 2.6). The wider body was used to assure larger scale vortex structures which are necessary for successful implementation of PIV.

4.2 GENERAL CHARACTERISTICS

For the flow conditions examined in this flow field study, the vortex system is unsteady, characterized by the periodic formation of necklace vortices which subsequently breakaway and move towards the block (Figure 4.1 is a schematic illustration of this type of periodic behavior as viewed on the symmetry plane). For this particular flow, a primary vortex forms approximately 132 mm upstream of the block (Figure 4.1 a-c). Following formation, the primary vortex breaks away from the formation region (at approx. 100 mm from the block) and advects downstream (Figure 4.1 c-d). The diameter of the primary vortex at this point is approximately 14-15 mm, which is approximately 81-87% of the equivalent, unobstructed Blasius boundary layer thickness (δ) for the same location (0.6 m) from the leading edge of the plate. As

described for regime 4, an eruptive type of event of the counter-rotating structure near the surface seems to be responsible for both causing the release of the primary vortex from the formation regime and forcing it away from the plate, where it advects downstream. Following release of the primary vortex, the secondary vortex gains strength and develops into a new primary vortex. As the original primary vortex approaches the block, it decelerates and coalesces with a corner vortex in the junction region (Figure 4.1 b-d). In addition, the vortex is stretched as it advects downstream, reducing the diameter of the vortex to approximately 12-13 mm (69-75% of the equivalent Blasius boundary layer) just prior to amalgamation; this corresponds to a 14% reduction in vortex diameter from breakaway to amalgamation, which is less than that observed by Greco (1990). This variance may be indicative of a difference between block and cylinder behavior, or it may reflect a limitation of Greco's use of hydrogen bubble visualization to estimate the diameter of vortices after breakaway, since the hydrogen bubbles will spiral towards the center of the vortex (due to local pressure variations across a vortex) and will most likely bias diameter estimates to the low side. The new corner vortex formed by the amalgamation process remains in the corner region until a new primary vortex arrives and this coalescence process repeats. The corner vortex undergoes a stretching process between amalgamations, which reduces its diameter by approximately 25% over a cycle, and also experiences image vortex induction, which causes it to move towards the plate and upstream as it coalesces with the new primary vortex. The frequency at which these events occur was determined to be 0.2 Hz from an extended visualization sequence, representing a Strouhal number of 0.605 based on block width; thus, the frequency of this breakaway behavior is about 4.65 times higher than the vortex shedding Strouhal frequency of 0.13 for a rectangular block

of this shape. At any given time during the cycle there are two vortices developing in the formation region upstream, as illustrated in Figure 4.1.

4.3 VELOCITY and VORTICITY FIELD

Figure 4.2 is a sample velocity field obtained following post processing of the particle images. The flow field dimensions captured in the PIV experiments were approximately 84x54 mm, with the block defining the right edge of the field and the flat plate the bottom of the field of view (Figure 2.6); note that this excludes the formation region. This field of view was selected to allow a close examination of the vortex interactions, providing adequate spatial resolution of both the discrete necklace vortices, as well as the smaller-scale structures created near the surface. For the purposes of this paper, the top 30 mm of the field of view, which reflects basically a uniformly decelerating free-stream flow, is not shown (Figure 2.6). The particular velocity field shown in Figure 4.2 reflects quantitatively the phase of the periodic cycle wherein a necklace vortex, to the left, is approaching a corner vortex, appearing to the right of the figure.

The z-direction vorticity field was established using Stokes theorem, which can be written as:

$$\iint_A (\nabla \times \vec{u}) \cdot d\vec{A} = \oint_c \vec{u} \cdot d\vec{s} \qquad (1)$$

Assuming the vorticity to be constant over $\bar{A}$, the vorticity is given by

$$\omega_z = \frac{1}{4\delta_x \delta_y} \oint_c \vec{u} \cdot d\vec{s} \qquad (2)$$

where δ_x and δ_y are the step sizes between two adjacent velocity vectors in the x and y directions respectively. The vorticity at a point was calculated from equation 2 by

numerically integrating around a rectangular path defined by the eight points adjacent to a selected point. Since numerical derivative computations are subject to high uncertainties, this Stokes theorems approach was used in lieu of a finite difference representation of the defining equation

$$\omega_z = \frac{1}{2}\left(\frac{\partial v}{\partial x} - \frac{\partial u}{\partial y}\right) \qquad (3)$$

to reduce the uncertainty of the vorticity calculations.

Figure 4.3a is a time sequence of the measured vorticity fields covering 10 seconds of the flow (about 2 cycles). In this figure, clockwise rotation corresponds to negative vorticity and is indicated by dashed lines; conversely, positive vorticity is indicated by solid lines. The iso-vorticity levels range from $\pm 1 \rightarrow \pm 41$ s^{-1} in intervals of 4 s^{-1}. The sequence shown in Figure 4.3a provides a detailed illustration of the behavior of the breakaway necklace vortex system in proximity to the rectangular body. As the sequence begins (Figure 4.3a i), a primary vortex has just begun to amalgamate with the corner vortex. As time progresses, a new primary vortex, formed out of the field of view, is advected downstream, entering at the left of the field of view (Figure 4.3a iii) with an advection velocity of approximately 48% of the local free stream velocity ($u_{adv} / U_{\infty,local}$); note that $U_{\infty,local}$ is defined as the velocity well outside the boundary layer at the same streamwise distance from the block as the advecting vortex. The vortex decelerates as it approaches the block (to an advection velocity of approximately 19% of the local free stream velocity just prior to amalgamation) and begins to amalgamate with the corner vortex (Figure 4.3a ix). Also apparent from Figure 4.3a is the development of concentrated opposite-sign vorticity generated near the trailing portion of the necklace vortices, which is the result of the interaction of the local vortex-generated pressure gradient with the surface fluid. This localized opposite-sign

vorticity concentrates, lifts from the surface, and erupts into the outer field, at times circumventing the original vortex, and apparently cross-canceling with the vorticity of the generating vortex (see section 4.5 below). Visbal (1991), in a computational study of the laminar necklace vortex system formed at a cylinder-flat plate juncture, also noted the aforementioned eruptions of opposite-sign vorticity caused by the interaction of necklace vortices with a surface.

Similar eruptive behavior has been determined by Peridier *et al.* (1991) in a computational study of the unsteady boundary layer separation induced by a two-dimensional vortex in motion above an infinite plate in a quiescent medium. Peridier observed the development of focused eruptions of boundary layer fluid near the trailing edge of the vortex caused by the interaction of the vortex with the surface. While Peridier's study examined the problem in the limit Re $\rightarrow\infty$ (much higher than the present study), the character of the behavior observed in the present necklace vortex system is essentially the same as that described by Peridier, suggesting that the mechanisms for the generation of these eruptions (i.e., local vortex-imposed pressure gradients) are the same.

The similarity of the observed eruptions of opposite-sign vorticity in the necklace vortex system to the bursting process characteristic of near-wall turbulent flows should be noted. It is suggested by Smith *et al.* (1991) that the eruption of surface fluid from the near-wall region into the outer field, caused by the interaction of coherent vortices embedded in a turbulent boundary layer with the surface fluid, is "...the fundamental means for regeneration and production of new turbulence," and as such is basically the "bursting" event described previously by others (e.g., Kim *et al.*, 1971). This implies that any method of control of the turbulent boundary layer must be based on controlling these fluid eruptions (Smith *et al.*, 1991). The present necklace vortex system allows the examination of the interaction of a vortex with a surface in relative isolation from the

competing influences present in a fully-turbulent flow, providing an understanding of the mechanism by which these eruptions occur, which is essential for development of intelligent control schemes for turbulent flow.

4.4 VORTICITY FLUX

Figure 4.3b is a series of vorticity flux plots which correspond to the vorticity plots of fig 4.3a. Vorticity flux (Φ_ω) is computed using the expression

$$\Phi_\omega = \int_0^y \omega u dy, \qquad (4)$$

which reflects the streamwise flux of vorticity across a vertical cross section of the flow field. The vorticity flux provides a measure of the instantaneous vorticity transport at any streamwise location at a particular time. The peaks of vorticity flux which appear in Figure 4.3b generally correspond to the necklace vortex position (negative peaks) or the surface generated vorticity (positive peaks). Note that from Figure 4.3b iii to 4.3b ix the vorticity flux associated with the primary vortex appears to systematically decrease as the vortex advects downstream, which suggests a "loss" of vortex strength as the vortices approach the block, prior to amalgamation with the corner vortex.

4.5 CIRCULATION and TRAJECTORY

The circulation of individual vortices was calculated from the velocity field using the line integral

$$\Gamma_v = \oint \vec{V} \cdot d\vec{s}, \qquad (5)$$

and integrating numerically around a contour of minimal constant vorticity (where ω= -1.0 s^{-1} was taken as the essential boundary of a vortex). Figure 4.4 is a plot of non-dimensional vortex strength (Γ_v/Γ_e, closed symbols) and vortex trajectory (open symbols), corresponding to the sequence Figure 4.4 iv to 4.4 xi.. The vortex strength is non-dimensionalized on an equivalent cyclic circulation term (Γ_e) obtained by integrating the vorticity flux passing through the left side of the field of view over approximately one cycle (Figure 4.3 iii to 4.3 x); this gave a cycle strength of approximately -4500mm^2/s, and represents the equivalent circulation strength of the vorticity advected into the field of view during one cycle. The circles in Figure 4.4 indicate the center of the incoming primary vortex, the triangles show the center of the initial corner vortex, and the squares show the center of the new corner vortex following amalgamation. Note that the primary vortex enters from the left and follows an essentially level path as it is advected downstream, while the corner vortex follows a roughly circular motion. At the point of amalgamation, the corner vortex is pulled beneath the primary vortex. Notice that each vortex continuously loses strength up to the point of amalgamation. The primary vortex circulation strength enters at approximately 33% of the equivalent cyclic circulation strength, decreasing to approximately 15% just before amalgamation. The corner vortex exhibits similar behavior, starting at a strength of about 25%, and decreasing to approximately 13% before amalgamation. During amalgamation, the new corner vortex increases sharply in strength, from about 13% to 25%, due to the additional vorticity contributed by the primary vortex. However, immediately following amalgamation, the new corner vortex experiences a sharp decrease in strength.

Note that the points on Figure 4.4 which correspond to the amalgamating vortices of Figure 4.3a ix are indicated by different positions, but reflect the same strength for each vortex. This is because at this point in the amalgamation process the ω=-1s^{-1}

contour (used to define the vortex strength, as mentioned above) engirdles both vortices, such that the strength of both vortices is merged. It is hypothesized that cross-cancellation of vorticity between the necklace vortices and the opposite-sign vorticity generated due to the viscous interaction of the respective vortices with the surface is the primary mechanism causing the observed decrease in strength of both the primary and corner vortex.

Because the necklace vortices deform three-dimensionally as they approach the block, they undergo a process of stretching by the flow around the sides of the block. To examine the potential for modification of the vortex strength by stretching, a simple model was examined wherein the vortex was modeled as a straight cylindrical solid body of rotation of length L, radius R, and uniform angular velocity Ω_z. Treating the flow as inviscid, the angular momentum is given by.

$$H = I_{zz}\Omega_z, \tag{6}$$

where

$$I_{zz} = \frac{\rho}{2} L\pi R^4. \tag{7}$$

Now, since angular momentum is conserved in an inviscid flow,

$$H_1 = \Omega_1 \frac{\rho}{2} L_1 \pi R_1^4 = H_2 = \Omega_2 \frac{\rho}{2} L_2 \pi R_2^4, \tag{8}$$

but the volume of the vortex remains constant after stretching, so

$$\begin{aligned} L_1 R_1^2 &= L_2 R_2^2 \\ \therefore \Omega_2 &= \Omega_1 \left(\frac{R_1^2}{R_2^2} \right). \end{aligned} \tag{9}$$

Examining the change in circulation,

$$\Gamma_1 = \omega_1 \pi R_1^2 = 2\Omega_1 \pi R_1^2$$
$$\Gamma_2 = \omega_2 \pi R_2^2 = 2\Omega_2 \pi R_2^2. \qquad (10)$$

Substituting equation 9 into 10 indicates that $\Gamma_1=\Gamma_2$ for inviscid stretching of a vortex. This illustrates that stretching of a vortex in an inviscid environment will redistribute the vorticity at a cross-section, but will not change the overall strength of the vortex. Since the present measurements indicate that the necklace vortex strength continually diminishes, this suggests that viscous effects must be responsible. There are basically two ways that viscous effects could manifest themselves. First, would be for vorticity to diffuse across the ω=-1 s^{-1} contour used to establish the vortex strength; the second, would be for cross-cancellation to occur between the necklace vortices and their corresponding surface-generated vorticity.

To examine the possible effects of viscous diffusion, the cross-section of a necklace vortex was modeled as a decaying Oseen vortex in a quiescent medium. Typical velocity profiles measured across a necklace vortex (see Figure 4.6) were compared to a comparable strength and diameter (at ω=-1 s^{-1}) Oseen vortex to establish a comparable state of decay. The change in circulation of the Oseen vortex from this initial condition over a four second period (the period of measured vortex decay from Figure 4.3a iv to 4.3a vii) was determined using ω=-1 s^{-1} as the boundary for determination of circulation strength. Using this approach indicated a "decrease" of circulation strength of the modeled Oseen vortex of about 8.0% due to diffusion across the ω=-1 s^{-1} boundary. However, Figure 4.4 indicates a decrease of approximately 50% for the same four second period from Figure 4.3a iv to 4.3a vii, or from the time the vortex enters the field of view up until just prior to amalgamation. This suggests that diffusion can play only a small part in the loss of vortex strength, and that vorticity cross-cancellation is the probable mechanism for the observed vortex decay. Re-examining

Figure 4.3a clearly shows this process in action, as the tongues of positive vorticity are observed to project away from the surface and engirdle the necklace vortices. Clearly, a continuous process of generation and ejection of opposite-sign vorticity, followed by engirdlement and cross-cancellation with the initiating vortex is the key mechanism in the observed rapid decrease in vortex strength and in establishing a balance of the vorticity field within the junction region.

4.6 VELOCITY PROFILES

The velocity field data was also used to examine selected u-velocity profiles for assessment of how the boundary layer is modified by the presence of the necklace vortex system and to examine the velocity distribution in the core of the necklace vortices. Figures 4.5a and b show selected velocity profiles for two frames of data (Figure 4.3a v and 4.3a ix). These suggest that the velocity distribution within the vortex core is quite similar to that of a combined Rankine vortex, with a central core which appears near solid body rotation. Figure 4.5a also illustrates that the profile shape is rather Blasius-like between vortices, taking on inflectional characteristics within the regions of surface-generated, positive vorticity. Note that the general behavior of these collective profiles in the vicinity of the primary vortex appears coincident with similar profiles determined by Visbal (private communication) from his previously published computational study of unsteady cylinder juncture flows (Visbal, 1991), including the combined Rankine behavior of the vortex core, and the inflectional behavior in the induced vorticity regions.

Note that inflectional profile behavior, similar to that shown in the induced vorticity regions of the present study, has also been shown computationally (Peridier *et al.*, 1991) to be indicative of vortex-induced boundary layer separation in the limit

$Re \rightarrow \infty$. Peridier showed that pronounced inflectional velocity profiles were manifested in the eruptive regions induced by a vortex above an infinite plate. The inflectional profiles observed in the present study are less pronounced because the necklace vortices were much weaker than those studied by Peridier. However, the similar profile behavior suggests that the eruptive mechanisms observed in this study are probably the same as those revealed by Peridier.

Figure 4.6 shows the collective center-line velocity profiles for the advecting primary necklace vortex (shown in Figure 4.3a iv through 4.3a vii). In this figure, the similarity of the core profile to that of a combined Rankine vortex is quite marked, illustrating that the profile behavior remains essentially invariant as the vortex advects toward the block.

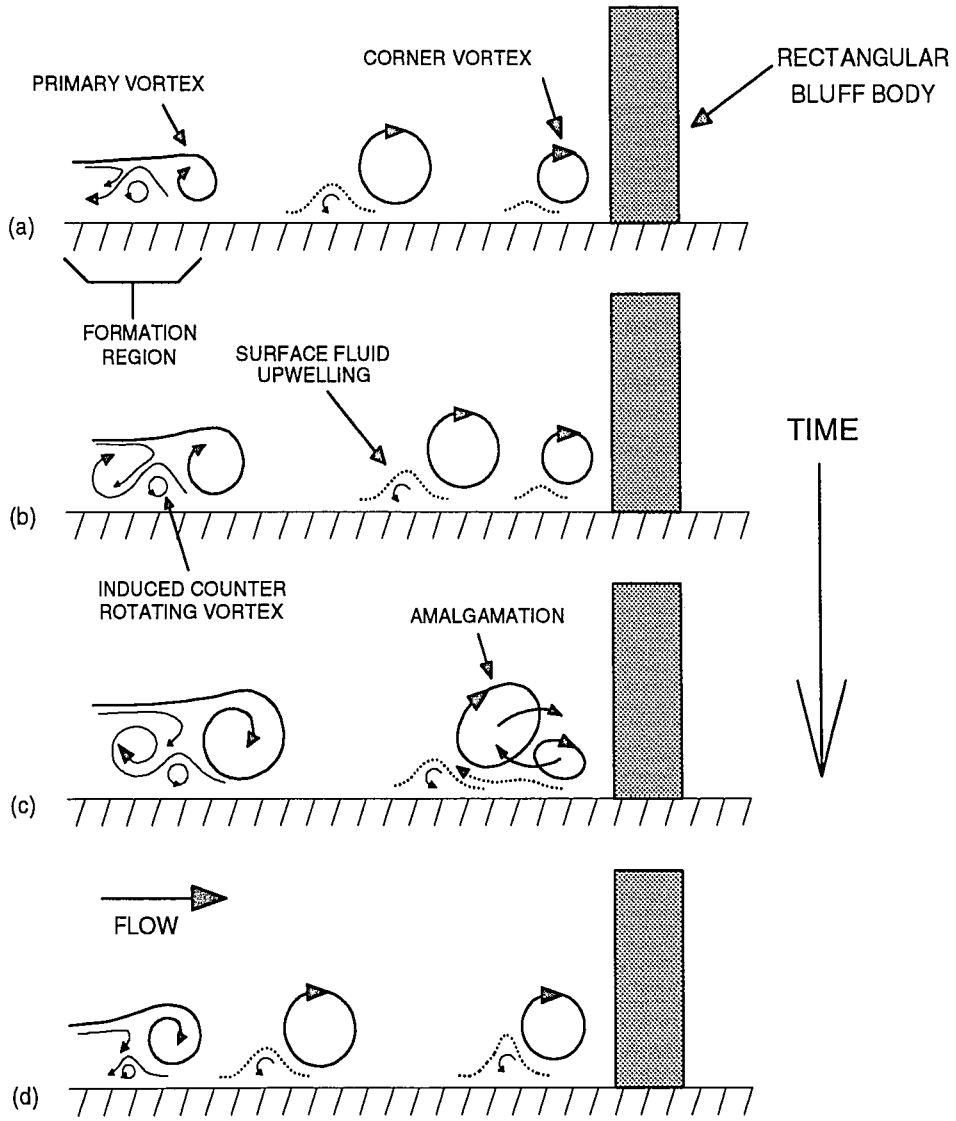

Figure 4.1 Schematic of unsteady necklace vortex system behavior viewed on the symmetry plane.

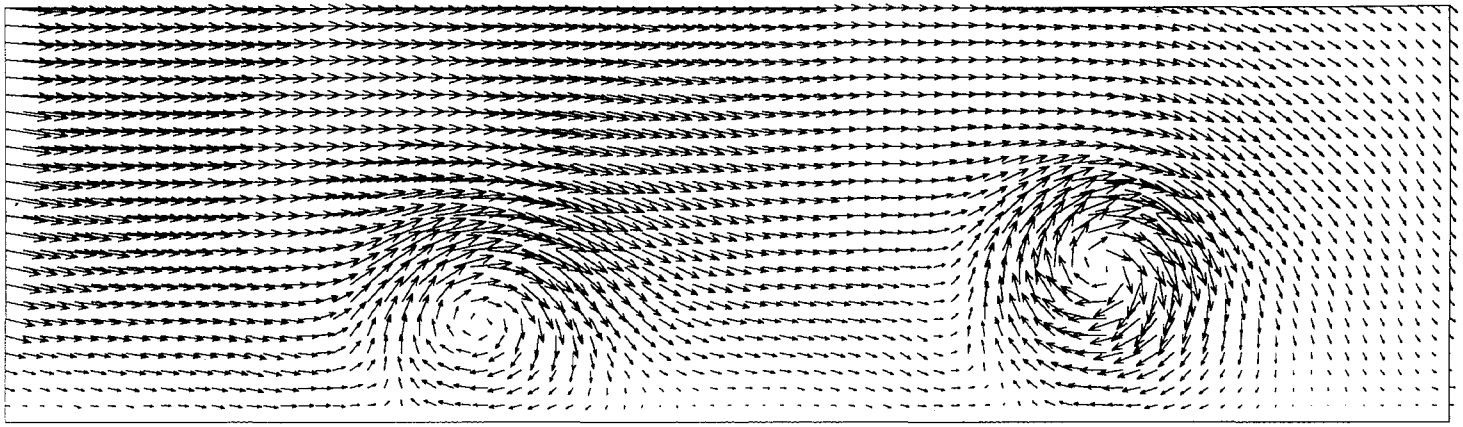

Figure 4.2 Sample velocity field (corresponding to figure 4.3a v) obtained after interrogation and post processing. Vector spacing is approximately 1.02 vectors/mm.

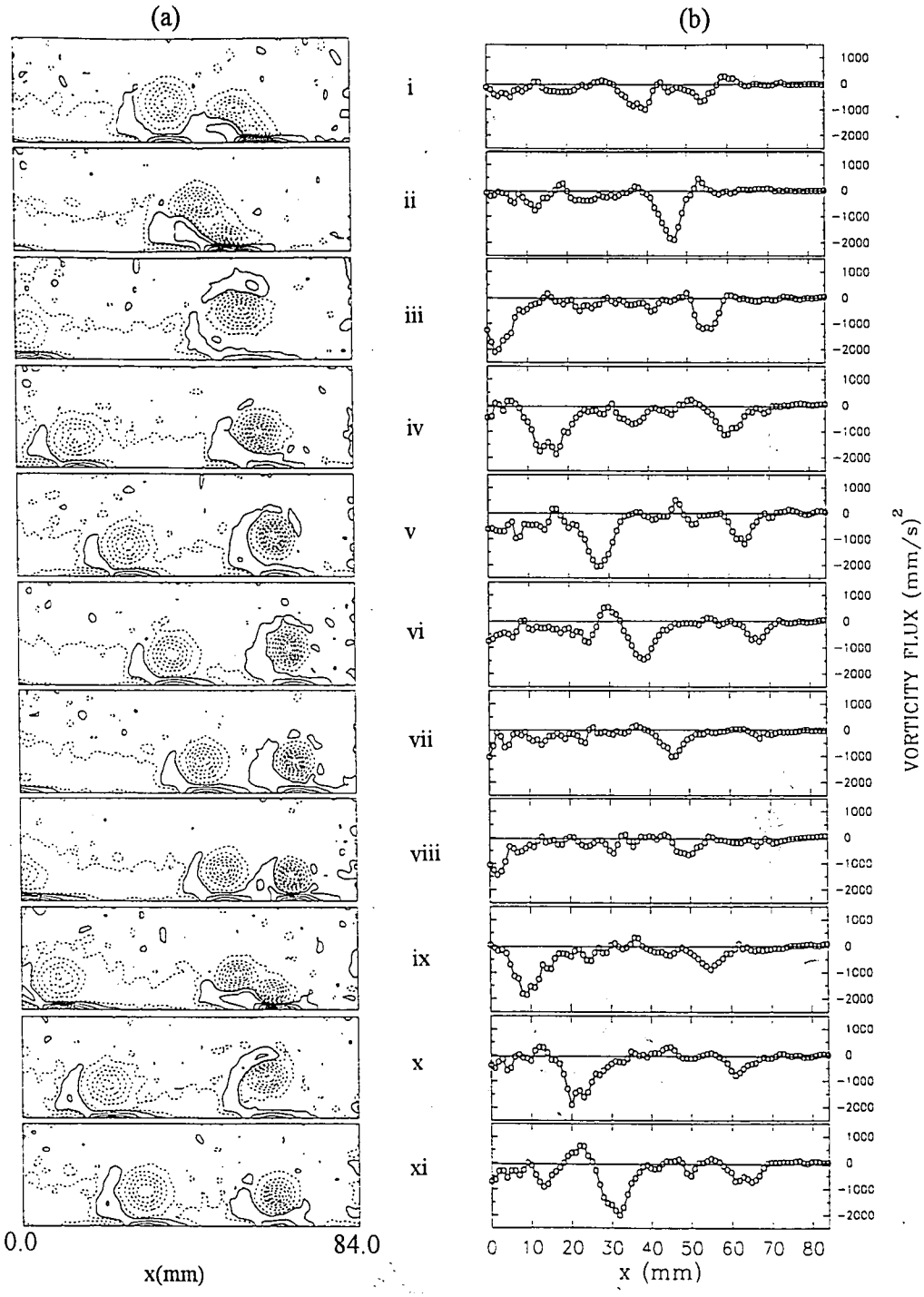

Figure 4.3 (a) Vorticity contours. Dashed lines indicate negative vorticity, solid lines indicate positive vorticity. Time between frames is 1.0s. (b) Vorticity flux.

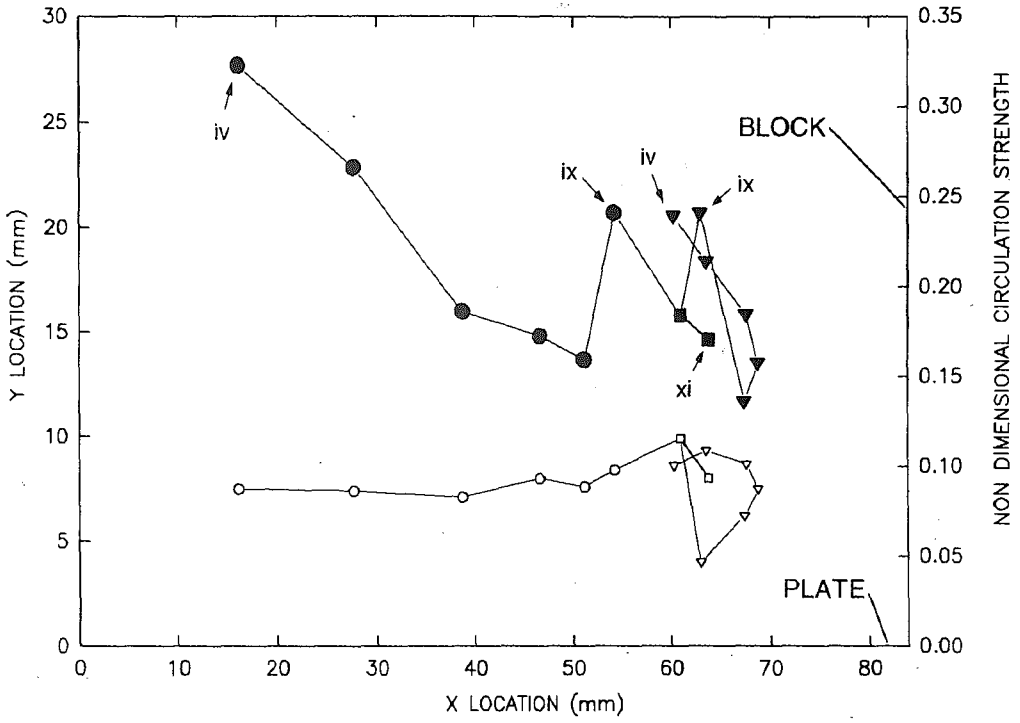

Figure 4.4 Vortex trajectory (open symbols) and non dimensional strength (Γ_v/Γ_e, closed symbols), where Γ_e is the time integral of vorticity flux passing across the left edge of the field of view over one cycle. Plotted data corresponds to Figure 4.3 iv to 4.3 xi. Circles represent the impinging primary vortex, triangles represent the corner vortex, and squares are the new corner vortex after amalgamation.

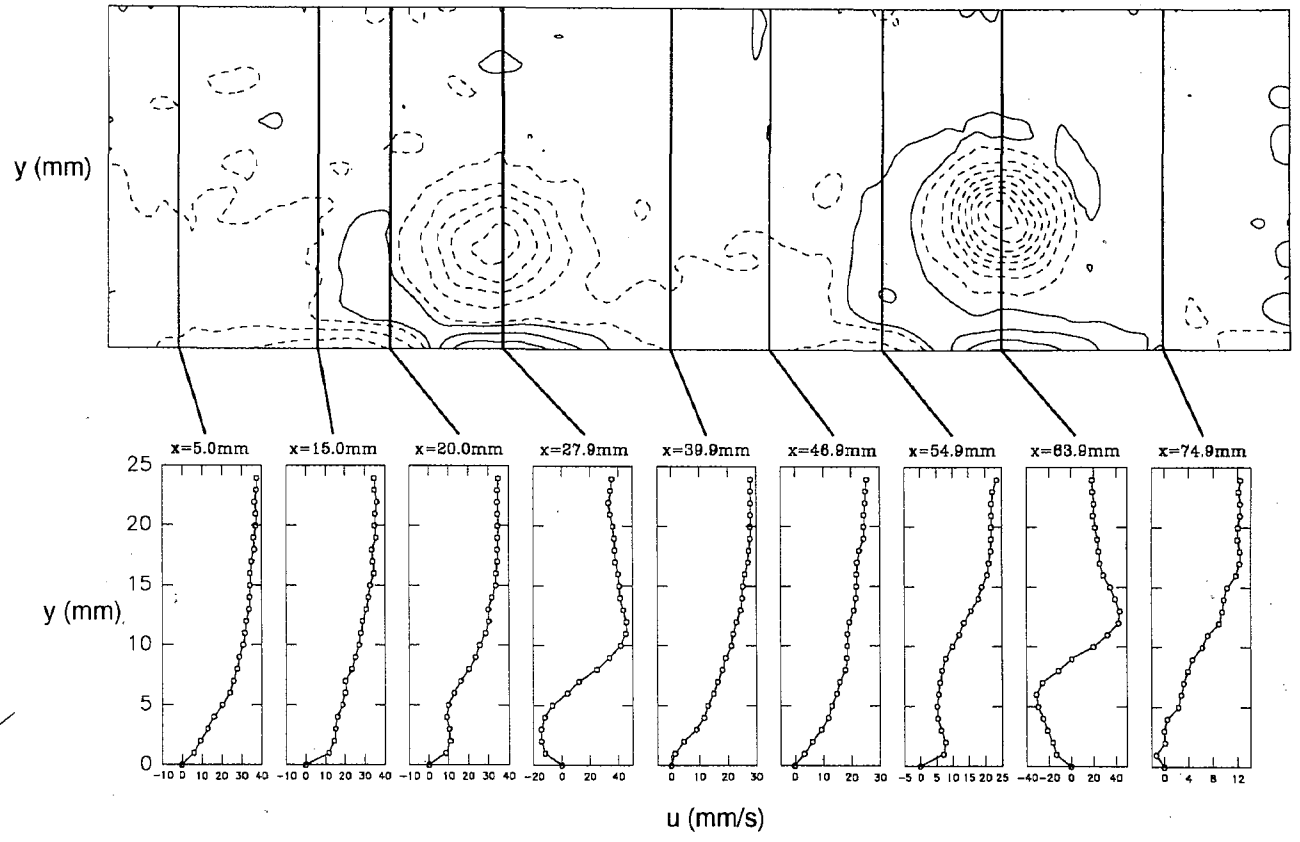

Figure 4.5 (a) Selected u-velocity profiles for Figure 4.3a v.

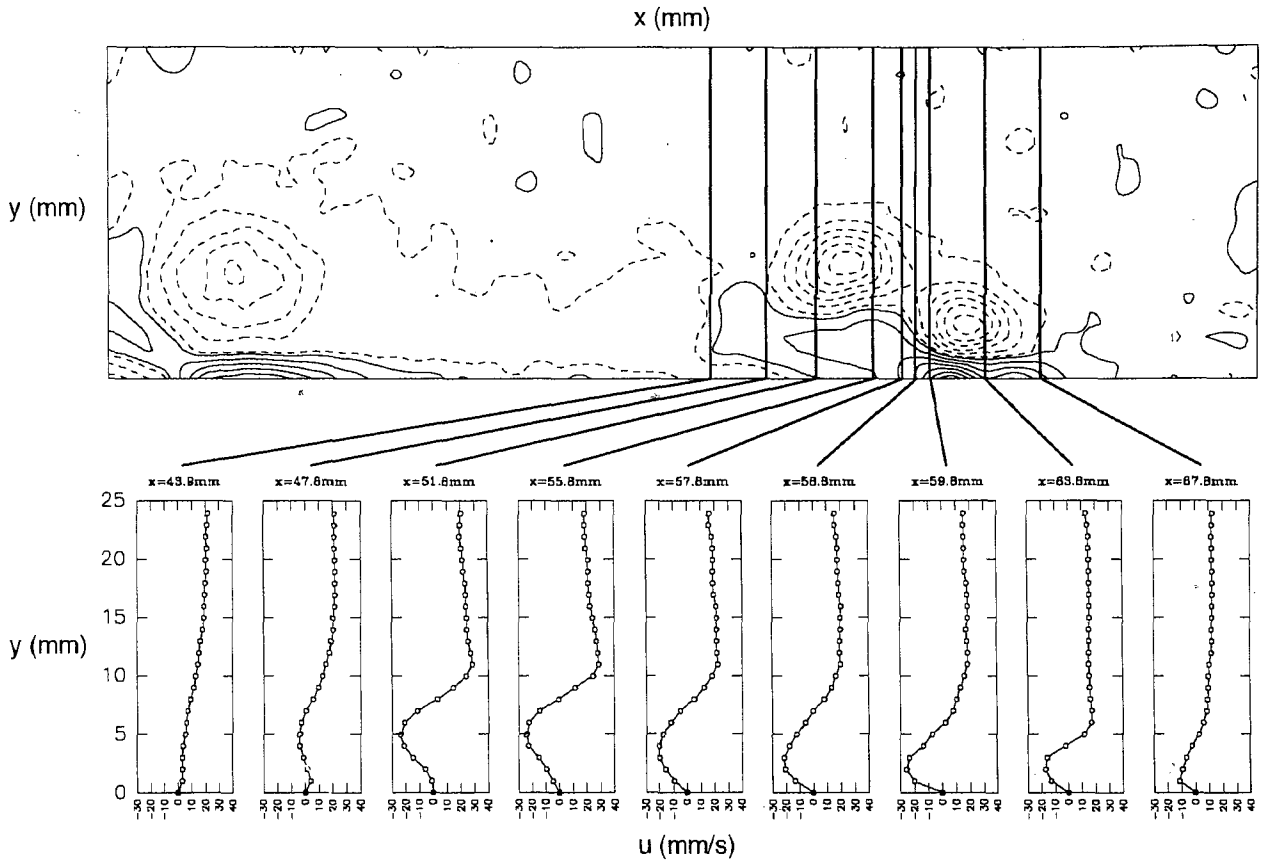

Figure 4.5 (b) Selected u-velocity profiles for Figure 4.3a ix.

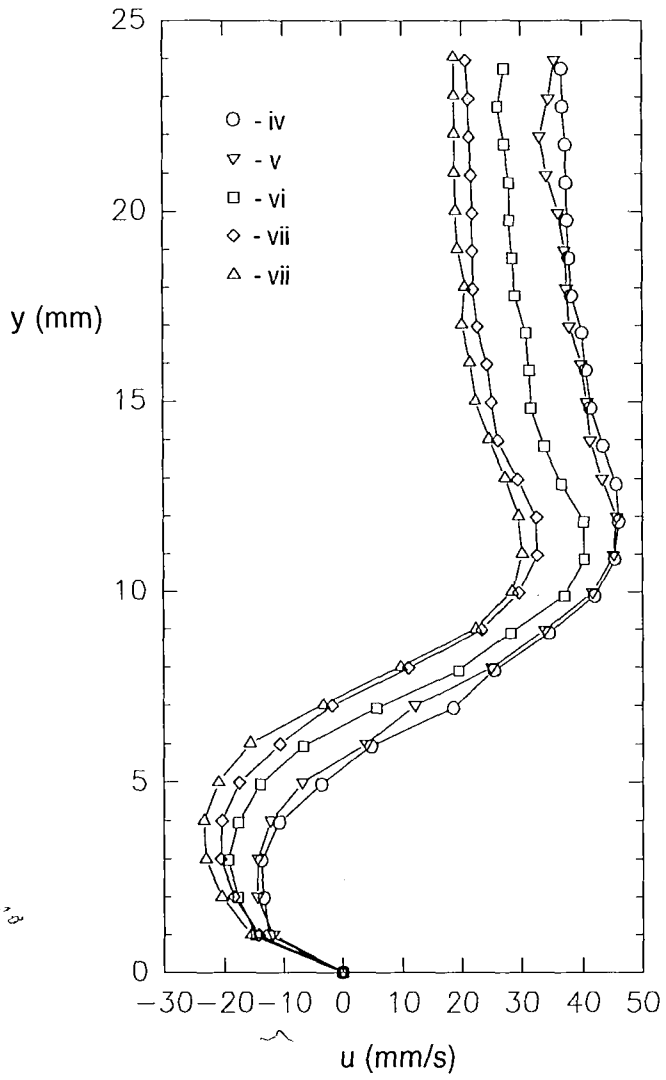

Figure 4.6 Centerline velocity profiles of a necklace vortex advecting downstream. Profiles correspond to the centerline of the primary vortex shown in Figures 4.3a iv to 4.3a vii. Each profile is taken at one second intervals.

5.0 CONCLUSIONS

The laminar necklace vortex system formed at a rectangular body-flat plate junction was examined qualitatively and quantitatively to establish the dynamics of the necklace vortex system, the distribution of system vorticity, and the process of vorticity balance within the system. Analysis of visualization and PIV results indicate that:

1. The laminar necklace vortex system formed at the junction of a rectangular block and flat plate exhibits five distinct flow regimes, depending on the flow speed, block width, fluid viscosity, and distance of the block from the leading edge of the plate.

2. The five flow regimes observed are: 1) a steady single necklace vortex, 2) a steady two necklace vortex system, 3) an oscillatory regime where two vortices oscillate periodically, and slightly out of phase with each other, 4) an amalgamating regime where the necklace vortices periodically form and amalgamate with each other, and 5) a breakaway regime where the necklace vortices periodically form, break away from the formation region, advect downstream towards the block, and amalgamate with a corner vortex near the block-plate junction.

3. The frequency of events in the unsteady regimes was found to be a function of free-stream velocity, block width, fluid viscosity, and distance of the block from the leading edge of the plate. The frequency of events increases essentially linearly with free-stream velocity (although for wider blocks the frequency behavior deviates from linearity), and

decreases with increasing block width and increasing distance of the block from the leading edge of the plate.

4. The advecting, primary necklace vortices within the breakaway regime exhibit velocity profile characteristics similar to that of an advecting combined Rankine vortex.

5. The necklace vortices interact with surface fluid adjacent to the plate, generating concentrated regions of opposite-sign vorticity, which lift away from the surface and interact with the generating vortex.

6. The necklace vortices undergo a systematic decrease in strength due to a cross-cancellation of the vorticity comprising the necklace vortices with the opposite-sign vorticity generated by the interaction of the necklace vortices with surface fluid.

7. Above a critical Reynolds number, small disturbances present in the necklace vortices are amplified and fed back upstream affecting subsequent vortex formation. The disturbances typically develop initially as hairpin-like distortions of the necklace vortices. Eventually the necklace vortex system destabilizes completely, resulting in a fully transitional flow regime dominated by the formation of hairpin vortices and an unsteady two-vortex system near the corner of the block-plate junction.

REFERENCES

ADRIAN, R. J., 1986, "Image shifting technique to resolve directional ambiguity in double-pulsed velocimetry," *Applied Optics,* Vol. 25, pp. 3855-3858.

ADRIAN, R. J., 1991, "Particle-imaging techniques for experimental fluid mechanics," *Annual Review of Fluid Mechanics,* Vol. 23, pp. 261-304.

BAKER, C. J., 1979, "The laminar horseshoe vortex," *Journal of Fluid Mechanics,* Vol. 95, part 2, pp. 347-367.

BLACKWELDER, R. F., & ECKELMANN, H., 1979, "Streamwise vortices associated with bursting phenomenon," *Journal of Fluid Mechanics,* Vol. 94, pp. 577-594.

BLEVINS, R. D., 1990, Flow-Induced Vibrations Second Edition, Van Nostrand Reinhold, New York.

CORCORAN, T. E., 1992, "Control of the wake from a simulated blade by trailing-edge blowing", M.S. Thesis, Dept. of Mechanical Engineering and Mechanics, Lehigh University.

GRECO, J. J., 1990, "The flow structure in the vicinity of a cylinder-flat plate junction: flow regimes, periodicity, and vortex interactions," M.S. Thesis, Dept. of Mechanical Engineering and Mechanics, Lehigh University.

GREGORY, N., & WALKER, 1951, W. C., "The effect of transition of isolated surface excrescences in the boundary layer," Rep. Memor. Aero. Res. Council No. 2779, London.

HAIDARI, A. H., 1990, "Evaluation of three-dimensional flow behavior of hairpin vortices," Ph.D. Dissertation, Lehigh University.

HAIDARI, A. H., & SMITH C. R., 1993, "The generation and regeneration of single hairpin vortices," submitted to the Journal of Fluid Mechanics.

HARVEY, J. K., & PERRY, F. J., 1971, "Flowfield produced by trailing vortices in the vicinity of the ground", *AIAA Journal, 9,* pp. 1659-1660.

KIM, H. T., KLEIN, S. J., & REYNOLDS, W. C., 1971, "The production of turbulence near a smooth wall in a turbulent boundary layer," *Journal of Fluid Mechanics,* Vol. 50, pp. 133-160

KLEIN S. J., & McCLINTOCK, F. A., 1953, "Describing uncertainties in single-sample experiments," *Mechanical Engineering,* January, p. 3.

LANDRETH, C. C. and ADRIAN, R., 1989, "Measurement and refinement of velocity data using high-image-density analysis in particle image velocimetry", *Applications of Laser Anemometry to Fluid Mechanics* (eds. R, J. Adrian, T. Asauuma, D. F. G. Durão, F. Durst, and J. H. Whitelaw), Springer-Verlag.

LUGT, H. J., 1983, Vortex Flow in Nature and Technology, John Wiley & Sons, New York

NORMAN, R. S., 1972, "On obstacle generated secondary flows in laminar boundary layers and transition to turbulence," Ph.D. Dissertation, Dept. of Mechanics/Mechanical and Aerospace Engineering, Illinois Institute of Technology.

OFFEN, G. R., & KLEIN, S. J., 1975, "A proposed model of the bursting process in turbulent boundary layers," *Journal of Fluid Mechanics,* Vol. 70, pp. 209-228.

PERIDIER, VALLORIE J., SMITH, F. T., & WALKER, J. D. A., 1991, "Vortex-induced boundary-layer separation. Part 1. The unsteady limit problem Re $\rightarrow\infty$," *Journal of Fluid Mechanics,* Vol. 232, pp. 99-131.

PERRY, A. E., & CHONG, M. S., 1982, "On the mechanisms of wall turbulence," *Journal of Fluid Mechanics,* Vol. 119, pp. 173-217.

PRASAD, A. K., ADRIAN, R. J., LANDRETH, C. C., & OFFUT, P. W., 1992, "Effect of resolution on the speed and accuracy of particle image velocimetry interrogation," *Experiments in Fluids,* Vol. 13, pp. 105-116.

ROCKWELL, D., MAGNESS, C., TOWFIGHI, J., AKIN, O., & CORCORAN, T., 1993, "High image-density particle image velocimetry using laser scanning techniques," *Experiments in Fluids,* Vol. 14, pp. 181-192.

RUNSTADLER, P. W., KLEIN, S. J., & REYNOLDS, W. J., 1963, Report No. MD-8, Department of Mechanical Engineering, Stanford University.

SCHWIND, R. G., 1962, "The three-dimensional boundary layer near a strut," Gas Turbine Lab. Report Number 67, M.I.T.

SEDNEY, R., & KITCHENS, C. W. Jr., 1975, "The structure of three-dimensional separated flows in obstacle, boundary-layer interactions", AGARD-CP-168 on Flow Separation.

SMITH, C. R., & SCHWARTZ, S. P., 1982, "Observation of streamwise rotation in the near-wall region of a turbulent boundary layer," *Physics of Fluids,* Vol. 26, No. 3, pp. 641-652.

SMITH, C. R., 1984, "A synthesized model of the near wall behavior in turbulent boundary layers," Proceedings of the Eighth Symposium on Turbulence, G. K. Patterson, J. K. Zakin, ed., University of Missouri-Rolla, Dept. of Chem. Engrg., Rolla, Missouri.

SMITH, C. R., 1987, "A study of hairpin vortices in a laminar boundary layer. Part 1. Hairpin vortices generated by a hemisphere protuberance," *Journal of Fluid Mechanics,* Vol. 175, pp. 1-41.

SMITH, C. R., 1987, "A study of hairpin vortices in a laminar boundary layer. Part 2. Hairpin vortices generated by fluid injection," *Journal of Fluid Mechanics,* Vol. 175, pp. 43-83.

SMITH, C. R., WALKER, J. D. A., HAIDARI, A. H., & SOBRUN, U., 1991, "On the dynamics of near-wall turbulence," *Philosophical Transactions of the Royal Society London A,* Vol. 336, pp. 131-175

THEODORSEN, T., 1952, "Mechanism of turbulence," Proc. of the Second Midwestern Conference of Fluid Mechanics, Ohio State University, Columbus, Ohio.

THOMAS, A. S. W., 1987, :The unsteady characteristics of laminar juncture flow," *Physics of Fluids,* Vol. 30, pp. 283-285.

TOWFIGHI, J., 1992, "Instantaneous structure of vortex breakdown on a delta wing," M. S. Thesis, Lehigh University.

VISBAL, M. R., 1991, "The laminar horseshoe vortex system formed at a cylinder/plate juncture," AIAA 22nd Fluid Dynamics, Plasma Dynamics & Lasers Conference, AIAA 91-1826

WALKER, J. D. A., 1978, "The boundary layer due to a rectilinear vortex," Proc. of the R. Soc. Lond. A 359, pp.167-188.

WALKER, J. D. A., SMITH, C. R., DOLIGALSKI, T. L., & CERRA, A. W., 1987, "Impact of a vortex ring on a wall," *Journal of Fluid Mechanics,* Vol. 181, pp. 99-140.

WHITE, F. M., 1974, Viscous Fluid Flow, McGraw-Hill Book Company, New York, New York.

WILLMARTH, W. W., & TU, B. J., 1967, "Structure of turbulence of the boundary layer near the wall," *Physics of Fluids,* Vol. Suppl. 10, p. 3134.

APPENDIX A - UNCERTAINTY ANALYSIS

The uncertainty of the frequency measurements discussed in section 2.7 was established using the mean square method described by Klein and McClintock (1953). If the result R is a given function of the independent variables, (i.e. $R=R(x_1, x_2,...x_n)$) then the uncertainty of the result can be expressed as:

$$w_R = \left[\left(\frac{\partial R}{\partial x_1} w_1\right)^2 + \left(\frac{\partial R}{\partial x_2} w_2\right)^2 + \cdots + \left(\frac{\partial R}{\partial x_n} w_n\right)^2\right]^{\frac{1}{2}} \qquad (1)$$

where w_R is the uncertainty of the result and $w_1, w_2...w_n$ are the uncertainties of the independent variables, $x_1, x_2,...x_n$.

For the frequency measurements the results were obtained using:

$$f = \frac{N}{t} \qquad (2)$$

where f is the frequency of events in the unsteady regimes (i.e. the frequency of oscillations, amalgamations, or breakaways) and N is the number of events observed for a given period of time, t. Substituting (2) into (1) and dividing by f yields:

$$\frac{w_f}{f} = \left[\frac{\left(\frac{\partial f}{\partial N} w_N\right)^2 + \left(\frac{\partial f}{\partial t} w_t\right)^2}{f^2}\right]^{\frac{1}{2}} \qquad (5)$$

where w_f/f is the percent error of the frequency measurements, w_N is the uncertainty of the number of events observed, and w_t is the uncertainty of the time measurement. The uncertainty of N was 0, since the number of observed events is easy to determine to an exact degree, therefore equation (5) simplifies to:

$$\frac{w_f}{f} = \frac{w_t}{t} \qquad (6)$$

Equation (6) shows that the uncertainty of the frequency measurements resides solely in the time measurement. Using equation (6) estimates of the error of the frequency data were made with a relatively conservative estimate of $\omega_t = \pm 0.5$ s. Since most video sequences used for data acquisition were 60 s to 120 s the majority of data points fall within a 0.8% to 0.4% error. A few cases are subject to an error of approximately 1.0%

The error associated with the PIV (Particle Image Velocimetry) measurements must also be addressed. In PIV primary sources of error are: 1) the visualization error -- associated with limited resolution of the optical data and data acquisition system, sampling error due to limited particle concentration; and 2) interrogation error -- errors arising from the numerical algorithm used to determine the position of the particles, as well as random errors due to particle imperfections, the recording process, and electronic noise. Quantification of these errors is difficult since the flow being studied is itself unknown; however previous studies (Prasad et. al., 1992) indicate that with present techniques and special care the errors can be reduced to acceptable levels. For example Prasad et al. (1992) using turbulent channel flow to determine the uncertainty in PIV calculated the magnitude of the error in the velocity field as under 2.0% of the total velocity vector for both the u- and v- velocity.

APPENDIX B - NO-SLIP WALL CONDITION IMPLEMENTED WITH PIV RESULTS

Since the plate was included within the field of view in the PIV experiments, special care had to be taken to ensure a no slip condition on the plate surface using the PIV data. Due to a variety of factors discussed in section 2.8, the original vectors determined during processing will not necessarily be 0 along the plate surface; many vectors will be either non-zero or will be indeterminant leaving a blank data point. Post processing consisted of first deleting the erroneous vectors, including non-zero wall vectors, from the field as described in section 2.8. Then an in-house computer program was used to replace *all* the wall vectors and blank data points on the wall with a zero velocity vector (note that because the flow was biased a zero velocity vector corresponds to u=bias velocity, v=0.0). The data file was then interpolated to fill in any adjacent blank data points and smoothed as described in section 2.8. Since the smoothing routine altered the wall values from zero, the computer program was again used to force the wall velocity to be zero. The resulting data file was used for all subsequent numerical analysis. Figure B.1 illustrates the effect of a forced no-slip condition on a typical PIV flow field.

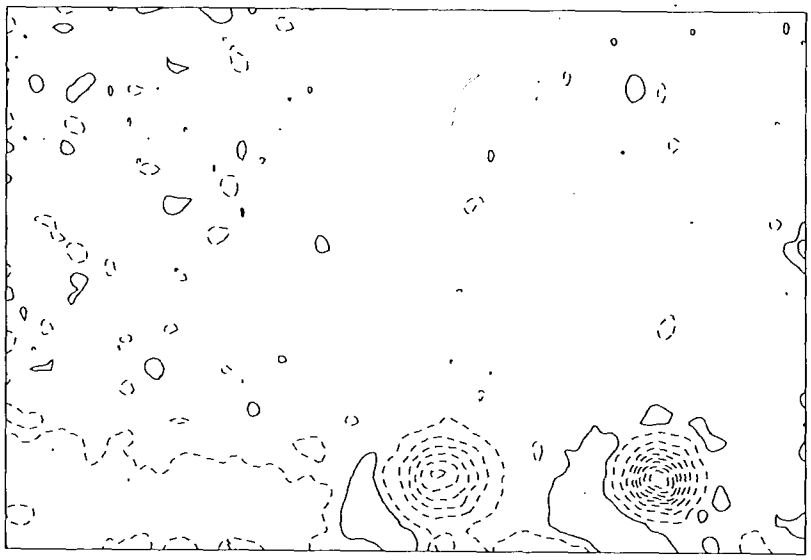

ORIGINAL POST-PROCESSED AND SMOOTHED DATA

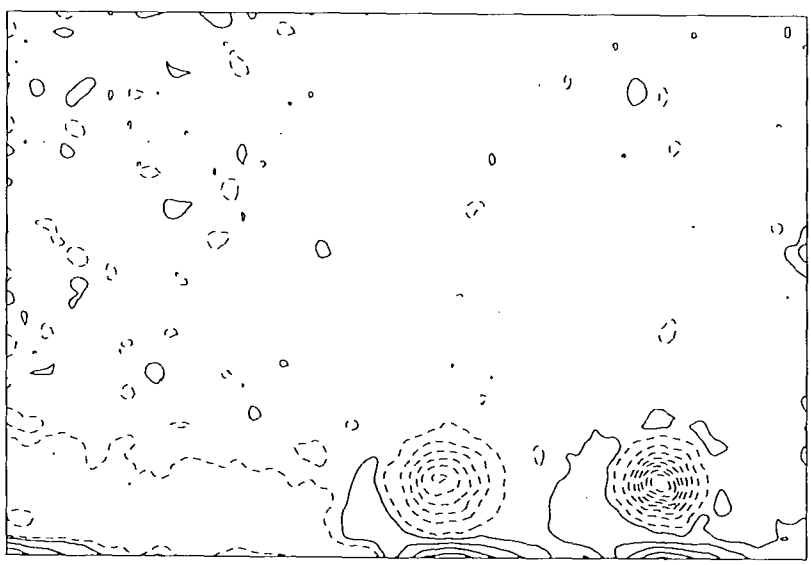

WITH AN IMPOSED NO-SLIP CONDITION

Figure B.1 Comparison of vorticity contours with and without the no-slip condition imposed on the plate surface.

APPENDIX C - FREQUENCY DATA

The frequency data used in this study is presented in Figures C.1 and C.2.

U (cm/s)	x=0.1 m	x=0.3 m	x=0.6 m	x=1.0 m
2.183				0.041
2.501		0.080	0.064	0.044
2.818		0.123	0.079	0.065
3.135		0.145	0.080	0.079
3.453		0.154	0.104	0.110
3.770		0.188	0.140	0.130
4.088	0.218	0.202	0.162	
4.405	0.248	0.229	0.177	0.160
4.722	0.266	0.234		
5.040	0.295	0.280	0.230	0.196
5.357	0.323			
5.675	0.369	0.333		0.231
6.309	0.446	0.390	0.317	0.271
6.944	0.507			0.292
7.579	0.559	0.500	0.423	0.337
8.214	0.685			
8.848	0.754	0.649	0.529	0.424
9.483	0.848			
10.118	0.977	0.791	0.646	0.548
10.753	1.082			
11.387	1.205	1.000	0.746	0.646
12.657	1.400	1.180	0.858	0.743
13.927	1.644	1.503	1.031	0.808
15.196			1.111	0.825

U (cm/s)	x=2.0 m
2.258	0.043
2.527	0.048
2.856	0.061
3.214	0.093
3.424	0.109
3.902	0.130
4.500	0.160
4.919	0.179
5.666	0.223
6.503	0.264
7.221	0.305
8.118	0.364
9.045	0.406
9.912	0.476
10.809	0.539

Figure C.1 Frequency (1/s) data obtained for the 5.1 cm x 5.1 cm block.

U (cm/s)	x=0.1 m	x=0.3 m	x=0.6 m	x=1.0 m
1.231			0.018	
1.549		0.036	0.034	0.038
1.866		0.043	0.049	0.052
2.183		0.067	0.062	0.059
2.501		0.082	0.084	0.070
3.135		0.126	0.111	0.093
3.770		0.166	0.146	0.123
4.405				0.148
5.040		0.240	0.215	0.183
5.675	0.162			0.190
6.309	0.185	0.320	0.277	0.206
6.944	0.197			0.243
7.261	0.215			
7.579	0.225	0.422	0.360	
8.214	0.247		0.386	
8.848		0.528		
9.039	0.263			
9.483	0.259			
10.118	0.290	0.616		
11.387	0.510	0.701		
12.657	0.582			
13.927	0.658			
15.196	0.699			
16.466	0.835			
17.735	0.994			
19.005	0.995			
20.274	1.221			
21.544	1.325			
22.813	1.493			
24.083	1.539			
25.352	1.828			
26.622	1.886			

Figure C.2 Frequency (1/s) data obtained for the 15.24 cm x 5.1 cm block.

VITA

The author was born in Albany, New York on July 11, 1969 to Charles and Virginia Seal. After graduating from Lakeland High School with Honors in 1987, he attended Clarkson University in Potsdam, New York where he received a Bachelor of Science Degree in Mechanical Engineering in the spring of 1991. While at Clarkson University the author was inducted into the engineering Honor society Tau Beta Pi and the Mechanical Engineering Honor society Pi Tau Sigma. Immediately following undergraduate work the author was accepted to Lehigh University as a Fellow, where he earned a Master of Science Degree in Mechanical Engineering in October 1993. The author plans to remain at Lehigh University and obtain a Ph.D., after which he would like to pursue a career in industry, emphasizing applied research and development in the field of Mechanical Engineering.

END

OF

TITLE